PHOTOPHYSICAL INVESTIGATION OF XANTHENES FOR USE IN BACKGROUND SUPPRESSION

A Dissertation
Presented to
The Academic Faculty

by

Aida Abebe Demissie

In Partial Fulfillment
of the Requirements for the Degree
Doctorate of Philosophy in the
School of Chemistry and Biochemistry

Georgia Institute of Technology
December 2019

PHOTOPHYSICAL INVESTIGATION OF XANTHENES FOR USE IN BACKGORUND SUPPRESION]

Approved by:

Dr. Robert Dickson, Advisor
School of Chemistry and Biochemistry
Georgia Institute of Technology

Dr. Stanislav Emelianov
School of Biomedical Engineering
Georgia Institute of Technology

Dr. Christoph Fahrni
School of Chemistry and Biochemistry
Georgia Institute of Technology

Dr. Elsa Reichmanis
School of Chemical and Biomolecular Engineering
Georgia Institute of Technology

Dr. Ronghu Wu
School of Chemistry and Biochemistry
Georgia Institute of Technology

Date Approved: September 19, 2019

To my parents who wanted everything for me and made sure I got it…

ACKNOWLEDGEMENTS

I owe a great deal of thankyous to several people who have been invaluable in the completion of my studies. First and foremost, I would like to thank my advisor, Professor Robert Dickson, for not only taking me in to his lab but also for his constant guidance and direction. I'm also grateful to the many friendly and intelligent lab mates past and present who have trained me in several techniques and constantly fielded my many, admittedly sometimes annoying questions. Of note are Dr. Saugata Sarkar who initiated our labs interest in PA imaging that ultimately became a topic I pursued throughout my PhD work, thank you for helping me get started your coaching and guidance has been invaluable. Dr. Amy Jablonski who taught me most of what I know about laser alignment and showed me the ropes when I first stated. Jung-Cheng Hsiang who spent countless hours helping me troubleshoot many experiments and unraveling the intricate details of my work, as well us for designing and writing code for many of the data acquisition and analysis software I've used throughout. Dr. Daniel Mahoney for constantly listening to me complain about the many things that did not work and for willing to be a sounding board and help me vet my ideas. Md Shariful for expertly taking over the nanoparticle synthesis aspect of the project so I didn't have to. I would also like to thank Baijie Peng, Joe Richardson, Alexandra Filbrun, Yi-Han Lu, Jagnyaseni Tripathy, Blake Richardson and Yen-Cheng Chen.

I also owe my gratitude to my collaborator Dr. Stanislav Emelianov, for his insights and guidance in photoacoustic imaging as well as Donald Vanderlaan for all that he has done in designing the setup that made photoacoustic modulation possible. I would also like to thank Dr. Jeff Petty, Dr. Raquel Lieberman and Dr. Dustin Huard, Ning Wu and Purva

Kodlekere. Other people I would like to thank for discussions and general guidance are Tony Du, Taylor Allen,

Thank you to my entire support system outside of the lab. Meron, Ashu, Kiwi and Bilu you guys have been a constant in my life thank you for being my sanity checks. I would also like to thank the many friends I've made during this journey especially Matt, Kali, Stephen, Rylan, Mauricio, Anthony and Jerry, thank you for the many laughs, and great food we've shared, the many Shakespeare tavern shows we've seen and the countless memories that made this long journey seem shorter and sweeter. I would also like to thank Aaron Mckee for just being great and believing I could do this even when I didn't want to. To Awaze thanks for being awesome. To my brothers Yoftahe and Ezana, and my family Kidi, Hawi, Nolawi, Elyana, Liqu, Julie, Chadwick and the rest of my extended family support network thanks for always being there when I needed an escape, Most of all, I would like to thank my parents without whose love, emotional and financial support and encouragement none of this would have been possible at all.

TABLE OF CONTENTS

ACKNOWLEDGEMENTS iv

LIST OF TABLES viii

LIST OF FIGURES ix

LIST OF SYMBOLS AND ABBREVIATIONS xiv

SUMMARY xvii

CHAPTER 1. Introduction 1
1.1 Motivation 1
1.2 Fluorescence Principles 3
1.3 Fluorescence Microscopy 4
1.3.1 Fluorescence Microscopy Techniques 6
1.3.2 Fluorescent Labels 6
1.4 Optical Modulation 9
1.5 Photoacoustic Imaging 11
1.6 Thesis Organization 13

CHAPTER 2. Experimental methodology 15
2.1 Sample Preparation 15
2.1.1 Solution and Immobilized samples 15
2.1.2 Phantom Preparation 15
2.1.3 Optically Modulatable Silica Nano-particle Synthesis 16
2.2 Bulk Fluorescence Microscopy 18
2.2.1 Optical Modulation 20
2.2.2 Time Correlated Single Photon Counting 25
2.3 Photoacoustic Experimental Setups 27
2.3.1 Photoacoustic Microscopy 27
2.3.2 Array Based Photoacoustic Imaging 32

CHAPTER 3. Xanthene Dye Photophysics 34
3.1 Introduction 34
3.2 Optical Modulation of Xanthenes 36
3.3 Triplet State Photophysics of Xanthene Dyes 41
3.4 Fluorescein Modulation 45
3.5 Conclusion 46

CHAPTER 4. Optically Activated Delayed Fluorescence 48
4.1 Introduction 48
4.2 OADF from Xanthenes 51
4.2.1 Pulsed-CW 53
4.2.2 Pulsed-Pulsed 63
4.3 Improved OADF Signals 65
4.4 Simulations of Xanthene OADF 67

4.5 Conclusion **71**

CHAPTER 5. Photoisomer Vs. Triplet Modulaiton in Merocyanine 540 **74**
5.1 Introduction **74**
5.2 Dark-state Photophysics of Merocyanine 540 **79**
5.2.1 CW excitation 79
5.2.2 Pulsed excitation 80
5.3 OADF Properties **85**
5.3.1 Photophysical Simulations of merocyanine 540 86
5.4 Conclusion **90**

CHAPTER 6. Synchronously Amplified Photoacoustic Image Recovery (SAPhIRe) **92**
6.1 Introduction **92**
6.2 Photoacoustic Modulation **93**
6.3 Single Element Photoacoustic Modulation **94**
6.3.1 Pulsed Primary - CW Secondary Illumination 94
6.3.2 Pulsed Primary - Pulsed Secondary Illumination 99
6.3.3 Dual Laser Modulation 102
6.4 Array Based Modulated Photoacoustic Image Recovery **106**
6.4.1 Phantom Modulation 106
6.4.2 Ex-Vivo Imaging 110
6.5 Conclusion **114**

CHAPTER 7. Conclusion and Future Outlook **115**

REFERENCES **119**

LIST OF TABLES

Label No.	Caption	Pages
Table 2-1	Excitation sources used for xanthene fluorescence experiments.	20
Table 3-1	Summary of experimentally determined time scales for one-laser modulation of xanthenes	44
Table 4-1	Triplet lifetimes of rose bengal, erythrosin B (EB) and eosin Y (EY) using 532nm pulsed primary excitation with coillumination at 830nm CW secondary.	57
Table 4-2	Xanthene photophysical parameters used in simulations	69
Table 4-3	Ratio of OADF photons to prompt fluorescence in simulated scenarios as well as experimental	70
Table 5-1	Measured photophysical timescales of merocyanine 540	85
Table 5-2	Photophysical parameters used for simulation	87

LIST OF FIGURES

Label No.	Caption	Pages
Figure 1-1	Figure 1-1 Jablonski diagram showing the different transitions and energy levels associated with fluorescence.	4
Figure 1-2	A fluorescence microscope diagram. In this case a light source is filtered for green light, which is used to excite the sample and subsequent red fluorescence transmitted for detection.	5
Figure 1-3	Illustration of optical modulation A) Jablonski diagram showing states involved in modulation of a three-state model.	10
Figure 1-4	Figure 1-4 Principle of photoacoustic imaging	12
Figure 2-1	Alginate phantoms without rose bengal (A) with rose bengal (B)	16
Figure 2-2	Procedure for making dye doped silica nano-particles	17
Figure 2-3	Microscope setup used for typical fluorescence experiments.	19
Figure 2-4	Experimental setup for typical fluorescence modulation experiments.	21
Figure 2-5	Picture of A) EOM and driver B) AOM and driver C) delay generator D) Function generators used in modulation experiments	23
Figure 2-6	Schematic showing pulsed primary cw secondary experimental setup when A) there is a sync out signal from laser (picoquant) and B) no sync connection available (uniphase).	24
Figure 2-7	schematic for simultaneous fluorescence/phosphorescence lifetime measurement.	25
Figure 2-8	Diagram of the principle behind time correlated single photon counting (TCSPC) acquisition	26
Figure 2-9	TCSPC inputs and electronics	27
Figure 2-10	Experimental setup for pulsed primary CW secondary photoacoustic modulation	28
Figure 2-11	Schematic of photoacoustic signal response upon secondary laser modulation.	28
Figure 2-12	Photoacoustic imaging setup showing the sample stage (top) and typical beam path	30
Error! Reference	Photoacoustic modulation sequence for single laser modulation. Green line indicates pulsed primary (532nm) with red line representing secondary or probe	30

source not found.	(1064nm) pulse. The delay between primary and secondary was adjusted to limit overlap of signals	
Figure 2-14	Dual modulation schematic of external waveforms applied to pulsed pump (blue) and probe (red) lasers operating at 5kHz (~10μs delay between pulsed) modulated at 23Hz for pump and 129Hz for probe and expected Fourier transform result of modulatable dyes	31
Figure 2-15	Picture of Vevo ultrasound imaging platform	33
Figure 3-1	Chemical structures of investigated xanthenes. A) Fluorescein B) Rose bengal C) Erythrosin B and D) Eosin Y	35
Figure 3-2	Absorbance spectra of 1μM water solutions of rose bengal (red), erythrosin B (orange) and Eosin Y (green)	36
Figure 3-3	Enhancement dependence of rose bengal on A) primary intensity with secondary held constant and B) secondary intensity with primary held constant	38
Figure 3-4	1Hz modulation of rose bengal fluorescence under 543nm primary and 830nm secondary coillumination and FFT of time domain signal showing a peak at the modulation frequency (1Hz).	40
Figure 3-5	Polarization dependence of rose bengal enhancement in PVA films.	41
Figure 3-6	Fluorescence decay histograms showing ground state recovery for rose bengal using different primary laser off periods, Toff. Primary laser is turned on for 10 ms and off for A) 3 ms, B) 12 ms. For each panel, data were collected and ratios of initial to final intensities within the average primary illumination period, Ton, as a function of Toff are fit to Equation 4.	43
Figure 3-7	Plot of Toff versus fluorescence recovery ratio at different off times.	43
Figure 3-8	Fluorescence signal from fluorescein using 488nm primary and 1Hz modulated 637nm secondary. Data was binned at 1Hz	46
Figure 4-1	Jablonski diagram showing photophysical transitions present in OADF capable fluorophores.	51
Figure 4-2	Normalized pulsed-cw fluorescence histograms of all studied xanthene dyes in PVA. OADF appears after the prompt fluorescence, with integrated OADF increasing with increasing triplet quantum yield along this series. Red dotted line shows prompt fluorescence with no OADF.	53
Figure 4-3	Fluorescence histogram of eosin Y in PVA films under constant pulsed primary (1kHz) excitation intensity and varying CW secondary coillumination showing that the decay constant decreases with higher secondary intensity.	54

Figure 4-4	Plot of secondary excitation intensity versus inverse of decay constant for eosin Y to show their linear relationship. Extrapolating to the y intercept gives $\boldsymbol{k_{off}^{0}}$ which is the inverse of the natural triplet lifetime.	55
Figure 4-5	Histograms of simultaneous fluorescence lifetime and phosphorescence lifetime measurements of rose bengal in PVA. Top panel shows the fluorescence decay on a ns timescale and bottom panel shows the phosphorescence on a ms timescale.	58
Figure 4-6	Fluorescence decay histogram of fluorescein under modulated 488nm excitation at varying intensities.	60
Figure 4-7	Plot of primary excitation power versus measured decay rate from the biexponential fit of fluorescein decay showing a linear relationship for both rates and an apparent convergence towards a single rate at lower excitation powers. The y-intercept gives the triplet lifetime (red) and photobleaching rate (green)	61
Figure 4-8	Fluorescence histogram showing OADF from fluorescein under pulsed primary (472nm) and CW secondary (637nm) excitation	62
Figure 4-9	Fluorescence histogram of rose bengal solution under pulsed primary (10kHz) and CW secondary coillumination under varying levels of oxygen.	63
Figure 4-10	Fluorescence histogram of rose bengal in PVA with 532nm pulsed primary followed by 830nm pulsed secondary illumination. Inset shows the clear dependence of OADF on laser repetition rate.	64
Figure 4-11	Fluorescence histogram of eosin y in PVA with pulsed 100ps excitation (red) CW 50μs pulsed width (black) primary excitation with simultaneous 830nm secondary illumination. Inset shows the clear increase of OADF in CW excitation over pulsed.	66
Figure 4-12	Fluorescence histogram of fluorescein in PVA under 50μs 488nm primary and 633nm CW secondary illumination exhibiting behavior characteristic of OADF.	67
Figure 4-13	Fluorescence lifetime of xanthenes a reconvolution fit	69
Figure 4-14	Fluorescence histogram of simulated eosin Y fluorescence under pulsed excitation (orange) and burst excitation (50μs) showing an increase in OADF with longer excitation cycles.	71
Figure 5-1	A) Photoisomerization in merocyanine 540 B) UV-vis absorption of merocyanine 540 in different media	75
Figure 5-2	Jablonski diagram illustrating fluorescence recovery pathways via dark state recovery. Secondary excitation of the dark (cis) photoisomer regenerates the all-trans ground state of the fluorescent manifold. In contrast, secondary excitation of the all-trans triplet can regenerate the excited state of the fluorescent manifold through reverse intersystem crossing, resulting in Optically Activated Delayed Fluorescence (OADF).	77

Figure 5-3	Schematic representation of a fluorescence histogram of the differences observed between modulation of a photoisomer (red) and a triplet that with OADF properties.	78
Figure 5-4	Fluorescence histogram of merocyanine 540 in water. A) Modulated CW primary excitation (543nm, 600 W/cm2), B) modulated primary plus constant (CW) secondary co-illumination (637nm, 10 kW/cm2), showing elimination of fluorescence decay due to lack of dark state build up.	79
Figure 5-5	Fluorescence histogram of merocyanine 540 in aqueous solution using 532nm pulsed excitation (rep rate 10 kHz) with 637nm CW co-illumination showing an OADF tail persisting past 2μs.	81
Figure 5-6	Fluorescence histogram of MC540 in water under pulsed 532nm primary (500kHz) and pulsed 637nm secondary excitation (10Mhz)	82
Figure 5-7	Fluorescence histogram of merocyanine 540 in PVA films under Pulsed primary and CW secondary excitation.	83
Figure 5-8	Fluorescence lifetime of Merocyanine 540 in PVA film using 532nm pulsed primary and 637nm pulsed secondary excitation. Inset showing the similar nano second decay nature of the OADF signal. A single exponential fit gives a lifetime of approximately 1.7ns for both prompt fluorescence and OADF	84
Figure 5-9	Fluorescence decay histograms showing A) experimental and B) simulated results of merocyanine 540 in PVA under consecutive 532nm and 647nm pulsed illumination.	89
Figure 6-1	Photoacoustic signal comparison between one and two laser illumination	95
Figure 6-2	Photoacoustic signal from rose bengal PVA phantoms under primary only (532nm 10kHz) excitation	96
Figure 6-3	A) Photoacoustic signal from eosin Y PVA phantoms with 532nm 10kHz primary excitation with co-illumination at 830nm (CW) secondary laser modulated at 1kHz. B) FFT of modulated signal showing peaks at both primary laser repetition rate and secondary modulation and their sum and difference.	98
Figure 6-4	Photoacoustic signal from graphite PVA phantoms with 532nm 10kHz primary excitation with co-illumination at 830nm (CW) secondary laser modulated at 1kHz showing similar modulation of primary induced photoacoustic signal upon CW secondary modulation	98
Figure 6-5	Photoacoustic signal generated by illumination at 532nm and consecutive 1064nm of rose bengal in PVA phantoms. Red circled region shows location of signal due to 1064nm and only that is monitored.	101
Figure 6-6	Photoacoustic signals generated by multiple 1064nm excitation pulses of rose bengal in PVA phantom with and without 532nm pre-illumination showing no signal generation with 1064nm only. First 50 pulses have a 532nm pump pulse 10μs	101

	prior to the probe 1064nm pulse while the last 50 only have 1064nm probe pulses clearly showing that there is no 1064nm response when primary (532nm) laser is turned off.	
Figure 6-7	TEM of rose bengal doped silica nanoparticles (Diameter = 95±14nm)	103
Figure 6-8	OADF decay of RB-SiO2 nanoparticles upon probe illumination with green arrow indicating time of pump and red showing probe delay. Exponential fit of this decay indicates an intermediate state lifetime of 20 μs	104
Figure 6-9	Comparison of OADF decay of rose bengal in silica nanoparticles, immobilized in PVA and in water solution showing PVA having longest triplet lifetime followed by silica nanoparticles.	105
Figure 6-10	Photoacoustic signal from RB-SiO2NP (black) and blood (red) under primary 23Hz and secondary 129Hz dual modulation showing the prescence of peaks at the sum and difference frequencies of the modulation in the RB-SiO2NP but not in blood.	106
Figure 6-11	Picture of phantom used for array based imaging. The two separate inclusions with a mixture of rose bengal doped silica nanoparticles and blood and only blood are made from alginate where the clear part is made of bulk rubber with silica powder added for scattering.	107
Figure 6-12	A) Ultrasound image of phantom showing both inclusions. B) photoacoustic signals from 532nm pump overlaid on ultrasound showing signal from both inclusions. C) SAPhIRe image generated by subtracting PA signal obtained with probe laser (1064nm) only from signal obtained with both pump and probe (532nm + 1064nm) showing suppression of background (i.e., blood) signal.	109
Figure 6-13	SAPhIRe imaging paradigm illustrating the different photophysical states affected by excitation at 532nm (green arrow) and 1064nm (red arrow) in optically modulatable (OM) contrast agents versus blood.	110
Figure 6-14	Photo of the rat carcass used and experimental setup for photoacoustic modulation. Photo was taken when 532nm was firing through filters that block both 532nm and 1064nm, which facilitates the visibility of fluorescence from the bolous injection of RB-SiO2 nanoparticles.	112
Figure 6-15	Ex-vivo photoacoustic results. A) Post-injection ultrasound image. The bolus is visible as an oblong echoic region. B) PA overlay using both pump and probe excitations. C) PA overlay using pump excitation. D) PA overlay using probe excitation. E) SAPhIRe overlay. The bolus (echoic US region) and SAPhIRe signal overlap very well. Signal also present along the injection trajectory. All images have 40dB and 32dB dynamic range for US and PA / SAPhIRe, respectively.	114
Figure 7-1	OADF from Rb-SiO_2-NPs showing change in triplet lifetime under varying oxygen concentrations. Experiement was done in an open system with constant nitrogen flowing above the sample.	117

LIST OF SYMBOLS AND ABBREVIATIONS

AOM	Acousto-optic modulator
APD	Avalanche photodiode
APS	(3-aminopropyl)triethoxysilane
CCD	Charge coupled device
CW	Continuous wave
Cy5	Cyanine 5
D	Dark state
EB	Erythrosin B
ECP	Effective core potential
EDC	1-Ethyl-3-(3-dimethylaminopropyl)carbodiimide
EOM	Electro-optic modulator
EY	Eosin Y
FCS	Fluorescence correlation spectroscopy
FFT	Fast Fourier Transform
FRET	Fluorescence (or Förster) resonance energy transfer
I_F	Fluorescence intensity
I_{pri}	Primary laser intensity
IR	Infrared
IRF	Instrument response function
ISC	Intersystem crossing
I_{sec}	Secondary laser intensity
k_{exc}	Excitation rate
k_f	Fluorescence rate

k_{isc}	Intersystem crossing rate
k_{iso}	Isomerization rate
k_{off}^{0}	Natural off rate
k_{off}	Off rate
k_{on}	On rate
MES	2-morpholin-4-ylethanesulfonic acid buffer
OADF	Optically activated delayed fluorescence
OLID	Optical lock-in detection
PBS	Phosphate buffered saline
PCM	Polarizable continuum model
PDT	Photodynamic therapy
PMMA	poly(methyl methacrylate)
PMT	Photomultiplier tube
PVA	Polyvinyl alcohol
QD	Quantum dot
RB	Rose bengal
RISC	Reverse intersystem crossing
RISO	Reverse isomerization
S_0	Ground state
S_1	Excited State
SAFIRe	Synchronously amplified fluorescence image recovery
SNR	Signal to noise ratio
TADF	Thermally activated delayed fluorescence
T_1	Lowest triplet state
TCSPC	Time-correlated single photon counting

UV-vis	Ultraviolet-visible spectroscopy
λ	wavelength
ν_{mod}	Modulation frequency
Φ	Quantum yield
ε	Extinction coefficient
ν_c	Characteristic frequency
σ	Absorption cross section
τ_c	Characteristic time
τ_{off}	Off time
τ_{on}	On time
Γ	Grüneisen parameter
μ_a	Absorption coefficient
α_{th}	Thermal diffiusivity
d_c	Heating region
τ_{th}	Thermal confinement time
ν_s	Speed of sound
δ	Energy fluence

SUMMARY

Fluorescence imaging is an important tool in biological imaging applications. Even with the many advances in this field endogenous background remains a challenge. Herein we present a way of circumventing background fluorescence by using dark-state photophysics of dyes. Amplitude modulation, as presented in Synchronously amplified fluorescence image recovery (SAFIRe), is a technique often employed to generate background free fluorescence signals. This work focuses on understanding the properties of optically the modulatable dyes in the xanthene family, rose bengal, erythrosin B and Eosin Y, with the goal of designing better fluorophores.

This work also outlines previously undescribed methods for optical modulation of xanthenes that give long lived fluorescence as a result of direct repopulation of the singlet excited state from the triplet state. This technique described as optically activated delayed fluorescence (OADF) allows for fluorescence signals to persist much after (~μs) the decay of prompt fluorescence (~ns) allowing for background free detection of signal.. The investigating the mechanism of modulation was investigated using both experimental and theoretical methods and modulation depth and in turn OADF generation was shown to increase with higher triplet quantum yields and at higher excitation rates. Dual laser modulation schemes have been used for photophysical characterization of dyes giving triplet lifetimes of 240μs, 420μs and 2.3ms for rose bengal, erythrosin B and eosin Y respectively.

Finally, optical modulation in photoacoustic imaging was investigated. Photoacoustic imaging is a non-invasive imaging modality that can offer much needed

improvements fluorescence imaging because of the significant reduction in acoustic scattering as compared to optical scattering. Photoacoustic techniques make use of the sound/pressure wave generation upon absorption of laser pulses. Because both fluorescence and photoacoustic signal generations depend on the population of ground state molecules that can absorb the excitation, similar approaches to dynamically shift population from the long-lived dark-states back to ground state will allow for background free photoacoustic imaging, synchronously amplified photoacoustic image recovery (SAPhIRe). SAPhIRe was used to distinguish rose bengal loaded silica nanoparticles from blood background as well as buried ~10mm in rat muscle.

CHAPTER 1. INTRODUCTION

1.1 Motivation

The invention of the modern microscope has revolutionized how we see and perceive the world around us. By being able to clearly visualize objects smaller than what can be observed by the naked eye we have developed a nuanced understanding of the human body, especially regarding the nature and complexity of its internal structures. Significant technological developments in fluorescence microscopy have allowed for this technique to serve an instrumental role in recent advancements in biological imaging.[1-4]. Fluorescence imaging techniques have incredible competency on the microscopic scale; advances in these techniques have enabled researchers to investigate biologically relevant topics such as protein dynamics[5-6] and cellular pathways[7-8].

Considering fluorescence imaging in medical and related contexts as the intended end-use application, in-vivo studies, those that are performed on living cells or organisms, are therefore paramount and represent the closest analogue to commercial use-cases within laboratory conditions. However, poor signal to noise ratios (SNR) due to large background signals from ubiquitous biomolecules such as hemoglobin and other endogenous chromophores have limited the use of fluorescence for many in-vivo applications.[9] Considerable research effort has focused on improving the visibility of signals over this large background by designing new fluorophores that are brighter, exhibit minimal spectral overlap with endogenous absorbers, and have higher labeling efficiencies compared to previous generation agents. With a similar goal in mind, techniques such as confocal microscopy, multiphoton excitation, and total internal reflection have been employed to

improve sensitivity of fluorescence imaging. Our group has pioneered the concept of using optical modulation as tool to suppress the background in fluorescence imaging applications while maintaining strong signals.[10-14]

Optical modulation is a technique which leverages the photophysical properties of fluorophores to selectively amplify target signal over background. Upon laser excitation, optically modulatable fluorophores not only emit via fluorescence but are able to undergo a transition to generate a long-lived dark-state with an absorption spectrum that is red shifted compared to its fluorescence. Co-illumination by a secondary laser coincident with this transient absorption can cause a transition back into the emissive fluorescence manifold, subsequently increasing detected signal. Modulation of the secondary excitation intensity will yield simultaneous modulation of the recorded fluorescence intensity which, upon demodulation, will yield background-free signal.

Despite all the aforementioned advances, use of fluorescence imaging in biomedical applications is limited in scope and remains an unattractive option for deep tissue imaging applications due to the competing background generated as a result of autofluorescence as well as the limitations that arise due to the scattering and the low penetration depth of light. The work outlined in this thesis focuses on improving sensitivity of fluorescence imaging by understanding the modulation properties of organic dyes in order to take advantage of fundamental photophysical processes. Moreover, this work also deals with the translation of these concepts and properties to a technique much more applicable to biomedical imaging. One such technique is photoacoustics, which is a hybrid of fluorescence and ultrasound imaging techniques. A photoacoustic approach is ideal for deep tissue imaging, as it suffers from significantly less scattering and signal attenuation

compared to fluorescence, while simultaneously allowing for improved sensitivity via similar photophysical properties exploited by modern fluorescence imaging techniques.

1.2 Fluorescence Principles

Fluorescence is a type of luminescence that arises from the subsequent emission of a photon after absorption of electromagnetic radiation, which within the context of proceeding discussion will typically fall within the ultraviolet (UV)-visible spectral range. The Jablonski diagram below Figure 1-1 is a general scheme often used to represent fluorescence and associated photonic transitions. The energy landscape for each transition, however, is unique to each fluorophore. Absorption of light by a fluorophore causes a transition from the ground singlet electronic energy level of the molecule (S_0) to the excited singlet electronic energy (S_1). The process of emitting a photon via relaxation from this higher-energy excited state back to the ground state is known as fluorescence. Since some of the absorbed energy is lost through vibrational relaxations with in the excited state, referred to as internal conversion (IC), the energy of the emitted photon is lower energy, i.e. higher wavelength, than the absorbed photons. In addition to fluorescence, electrons in the excited singlet state may also lose their energy through non-radiative processes or might transition in to a triplet state (T_1) with a different spin multiplicity, through inter-system crossing (ISC). Triplet states are often termed “dark states”, because they are not directly accessed through absorption/emission process; they are longer lived than the fluorescence generating state and act as a temporary sink, reducing observed fluorescence. Once a molecule is transitions into a dark state it must undergo a spin flip to either radiatively decay (phosphorescence) or non-radiatively decay back to the singlet ground state. The absorption cross section (σ) or molar extinction coefficient (ε) can be used to represent the

absorption of fluorophores. The fluorescence quantum yield (Φ_{fl}) and intersystem crossing quantum yield (Φ_{isc}) give the likelihood that the relaxation pathway will proceed via either fluorescence or a transition into a transient dark state, respectively. The propensity for the transient state represented as a triplet in Figure 1-1, which can relax back to the ground state via radiative process, is described by the phosphorescence quantum yield (Φ_p) but can also non-radiatively transition back to the ground state.

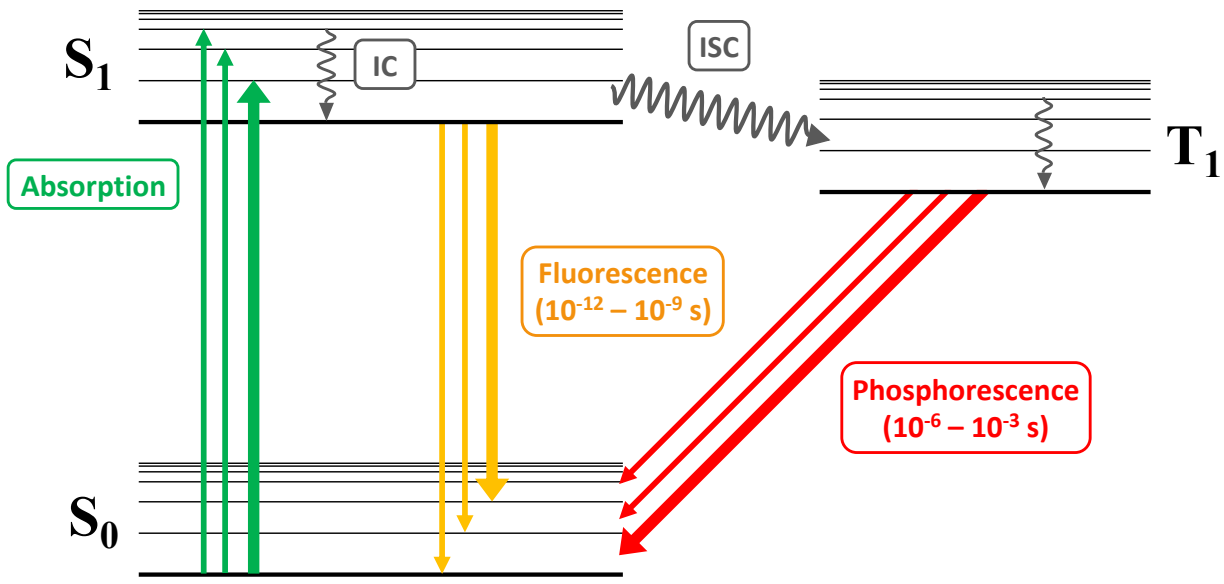

Figure 1-1 Jablonski diagram showing the different transitions and energy levels associated with fluorescence.

1.3 Fluorescence Microscopy

Fluorescence microscopy has become invaluable to modern advances in biological research. The principal competency of a fluorescence microscope lies in its ability to separate the much weaker fluorescence signal from the abundant excitation light by

because excitation light can be filtered out making fluorescence nearly zero background and therefore higher sensitivity. Briefly described in Figure 1-2, a lamp or laser is used as an externally administered excitation source; this light is directed via a series of mirrors on to an appropriate dichroic mirror and continues through an objective on to specimen of interest. The fluorescence generated is then optically guided back through an objective and dichroic mirror on to a detector. Since emission and excitation are usually at different wavelengths, a dichroic mirror is used to reflect the excitation light to the sample while it simultaneously transmits the emission light to the detector. This scheme is employed, in combination with appropriate fluorescence and excitation filters, to ensure only emission wavelengths are recorded on the detector and thus provide the foundational operating principles for fluorescence imaging.

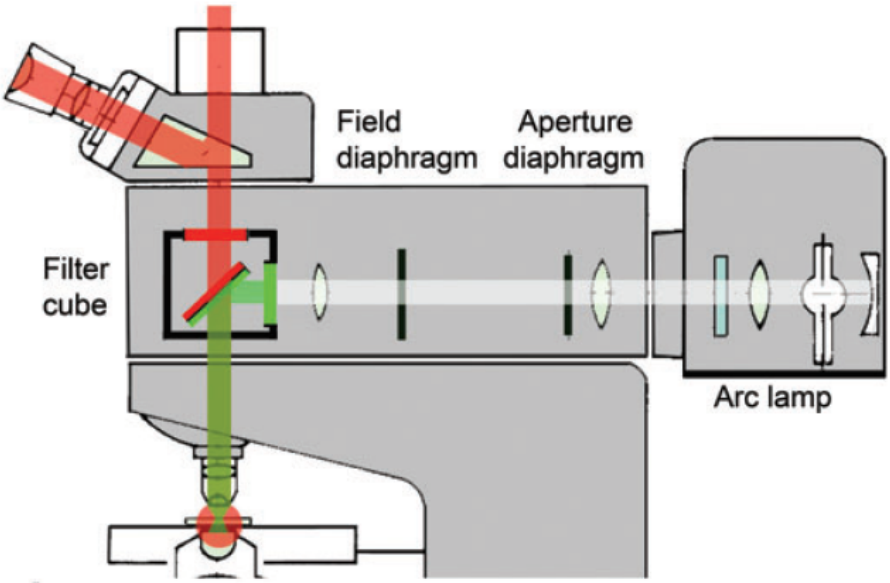

Figure 1-2 A fluorescence microscope diagram. In this case a light source is filtered for green light, which is used to excite the sample and subsequent red fluorescence transmitted for detection.

1.3.1 Fluorescence Microscopy Techniques

Over the years several techniques have been developed that take advantage of fluorescence microscopy. Some of the most noteworthy are fluorescence correlation spectroscopy (FCS)[15-16], which employs stochastic fluctuations in a system to understand photophysical dynamics. Forster resonance energy transfer (FRET)[17], which exploits the overlap of excitation and emission spectra of two systems to determine distance between donor and acceptor groups. Fluorescence recovery after photobleaching (FRAP)[17], is a method used to investigate the kinetic of diffusing fluorescently labeled molecules, by monitoring the fluorescence recovery of a sharply defined region of interest upon photobleaching. Fluorescence lifetime imaging/ Phosphorescence lifetime imaging (FLIM/PLIM)[18] is an imaging technique where the fluorescence/phosphorescence lifetime is a source of contrast.

1.3.2 Fluorescent Labels

An important characteristic of modern fluorescence microscopy techniques is the ability to distinguish a specific biological target solely based on emission. Usually this is accomplished by employing a fluorescent tag that has optical properties which are distinct from surrounding auto-fluorescent background that would otherwise limit visibility of target. Ideal fluorophore selection is by no means a trivial matter and requires bearing in mind multiple elements. Some main parameters often considered as key factors for a successfully selecting appropriate fluorescence tags are labeling chemistry, biocompatibility, absorption and emission color, photostability, brightness, and size of fluorophore.

There are several types of fluorophores that span the visible to near-infrared (NIR) spectral range, each with a particular set of advantages and disadvantages. The most common varieties of fluorophores include organic dyes, quantum dots, fluorescent proteins and small atom metal clusters.

1.3.2.1 Organic Dyes

Organic dyes are one of the most commonly used fluorescent labels. Their high extinction coefficient (50,000 – 300,000 $M^{-1}cm^{-1}$) coupled with their high quantum yield (up to 90%) makes them ideal fluorophores[19-20]. This particular class of dyes is available in a range of emission and excitation wavelengths and is highly desired for its relatively small size, ease of synthesis and tunability. Generally, the emission of these dyes arises from an optical transition delocalized over the whole chromophore as is the case with xanthenes, BODIPY dyes, rhodamines and most cyanines. Though less common and often with lower emission quantum yields charge transfer transitions can also lead to emission as in coumarins[21]. Some of the brightest organic fluorophores belong to the xanthene or cyanine dye families. Even in idealized scenarios however, sensitivity is still a challenge for these dyes, which has motivated the development of signal enhancing methods that have potential biocompatibility issues.

1.3.2.2 Fluorescent Proteins

Fluorescent proteins are proteins which contain a chromophore embedded with in a β-barrel, affording them improved stability. [22-23] This class of fluorophores does not achieve the high levels of extinction coefficients of organic dyes (~100,000 $M^{-1}cm^{-1}$) but has a fluorescence quantum yield of ~50%. The advantage of fluorescent proteins lies in their high biocompatibility and ability to be genetically encoded and expressed in cells.

Fluorescent proteins have been created with excitation and emission profiles that span the visible spectrum and have been optimized for optical properties such as brightness and photoswitching.[24-31] These properties make them ideal candidates for advanced fluorescence studies and technique development.

1.3.2.3 Metal Nanoclusters

Metal clusters are characterized as small collections of metal atoms, usually gold or silver, imbedded in a scaffold to prevent aggregation which can lead to the formation of larger or amorphous non-fluorescent particles. Due to their nanoscopic scale, these metal clusters exhibit discrete molecular transitions which can be tuned by changing cluster size and scaffold architecture. Our lab has previously developed silver clusters in single-stranded DNA (ssDNA)[11, 32] or peptide[33] scaffolds with emission wavelengths spanning the visible-NIR spectrum. Metal nanoclusters generally have high luminescence and photostability with extinction coefficients reaching ~10^5 $M^{-1}cm^{-1}$ and a quantum yield of ~40%.

1.3.2.4 Quantum Dots

Quantum dots are inorganic semiconductor nanoparticles that also exhibit size dependent physical and chemical properties. Their size often ranges between 1-20nm in diameter. They are extremely bright and photostable fluorophores with extinction coefficients of ~10^6 $M^{-1}cm^{-1}$, and a wide range of emission colors[34-35]. Though quantum dots offer large gains in signal visibility, their potential toxicity concerns and functionalization vastly limits their using in biological applications[36-38]. Because quantum dots are made of semiconductor materials, often CdSe or CdTe, which are biologically

incompatible they require the use of ligands which add extra bulk further limiting the scope of their application[39-40].

1.4 Optical Modulation

Optical control of long-lived dark states has been used in several fluorescence techniques, often aimed at improving resolution using photoisomerizing fluorophores that can selectively transition from a bright state to a dark state and vice versa. Stochastic optical reconstruction microscopy (STORM)[41] and photo-activated localization microscopy (PALM)[42-43] have exploited the nature of these photoswitches to generate a high resolution image by successively marking locations of single molecules as they emit. Optical lock-in detection (OLID)[44] has been employed to extend the use of these photoswitches to improve imaging sensitivity by optical modulation of the emission by controlling population in the bright and dark state. OLID makes use of a reference signal for image reconstruction and thus requires the additional measurement of an internal standard. Unfortunately, reconstructed OLID images, however, are not linear in fluorophore concentration due to their nonlinear cross-correlation-based signal processing.

Synchronously amplified fluorescence image recovery (SAFIRe)[14], pioneered by the Dickson group, is a method of reducing noise by shifting signal to a unique detection window with minimal background. This is accomplished by taking advantage of the long lived transient "dark" states of fluorophores. Outlined in Figure 1-3,Upon absorption of light by a fluorophore, electrons are excited to a higher lying energy state which can return back to the ground state through fluorescence. Alternatively, these excited electrons can transition to a non-fluorescent "dark" state. The lifetime of this state is typically longer than the approximately nanosecond fluorescent timescale, therefore a decrease in the

fluorescence intensity is observed as population builds in the dark state over time. Once in the dark state, molecules are trapped until they naturally decay back into the singlet ground state, either radiatively or non-radiatively. Excitation of the dark state can be achieved by, often, a longer wavelength laser which serves to depopulate this state faster than it would naturally decay and results in an enhanced fluorescence signal. Intensity modulation of the secondary excitation will directly encode this frequency on the fluorescence signal such that the signal of interest can be obtained upon demodulation. By choosing a secondary excitation that selectively affects only the transient state of the fluorophore and detecting only at the modulation frequency of the secondary excitation laser, we can effectively remove background. Several fluorophores suitable for SAFIRe, ranging from organic dyes, silver clusters and fluorescent proteins capable of being optically modulated have been identified.

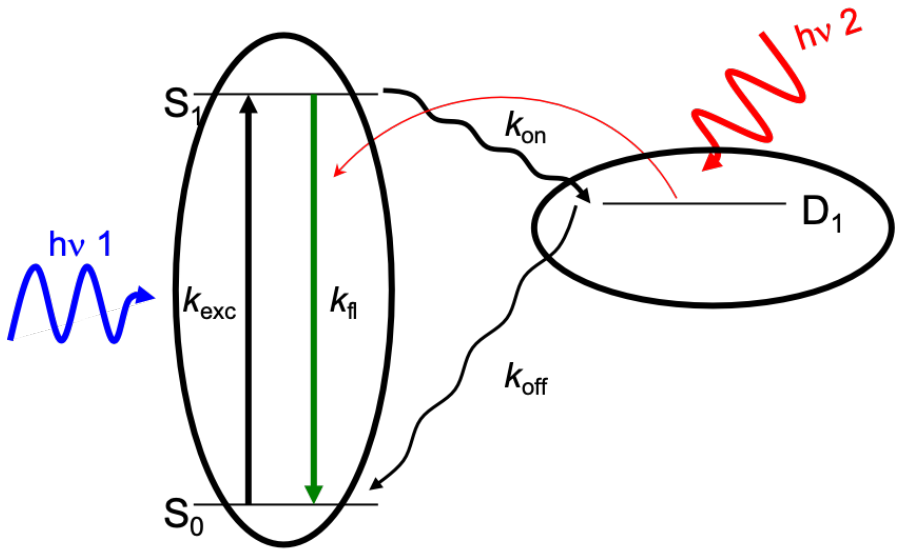

Figure 1-3 Illustration of optical modulation A) Jablonski diagram showing states involved in modulation of a three-state model.

Organic dyes, metal clusters and fluorescent proteins have been shown to be optically modulatable through different photophysical processes. The xanthene dyes rose bengal, eosin Y and erythrosin B have been shown to be optically modulatable via long wavelength depopulation of their triplet state[14] whereas in a 630nm-emitting few-atom silver clusters the modulation was shown to arise due to the presence of charge separated dark state. The path to optical modulation for some fluorescent proteins[13, 26, 28] and cyanines,[45] on the other hand, takes advantage of the presence of a cis-trans isomerization process.

1.5 Photoacoustic Imaging

There is a great need for the development of imaging and detection technologies that can diagnose small, early stage pathologies deep within tissue. Suffering from high scattering and strong auto-fluorescence, in-vivo fluorescent imaging is plagued by high non-specific background signal. Even within the lower background and reduced absorption optical window, 700nm to about 1000nm, the penetration depth of light in human skin is less than 2 mm. This causes background to dominate desired fluorescent signals and makes identifying signal very difficult. Conversely, photoacoustic (PA) imaging has tremendous potential for deep tissue imaging because acoustic waves experience less scattering compared to optical waves in tissue. The attenuation of acoustic waves is two to three orders of magnitude less than optical waves, allowing for recovery of photoacoustic signals from deep within tissue

Photoacoustic imaging is a non-invasive imaging modality that can offer much needed improvements over current techniques. The photoacoustic effect, long ago reported by Alexander Graham Bell, is the basis for photoacoustic imaging.[46] Summarized in Figure 1-4, generation of a photoacoustic signal is achieved via sample irradiation by short laser

pulses which cause a thermo-elastic expansion in the sample. This expansion leads to the generation of sound/pressure waves that are detected by ultrasonic transducers placed around the sample. Photoacoustic imaging exploits properties of both ultrasound imaging and fluorescence imaging by combining the better contrast of optical imaging with the superior depth penetration of ultrasound.

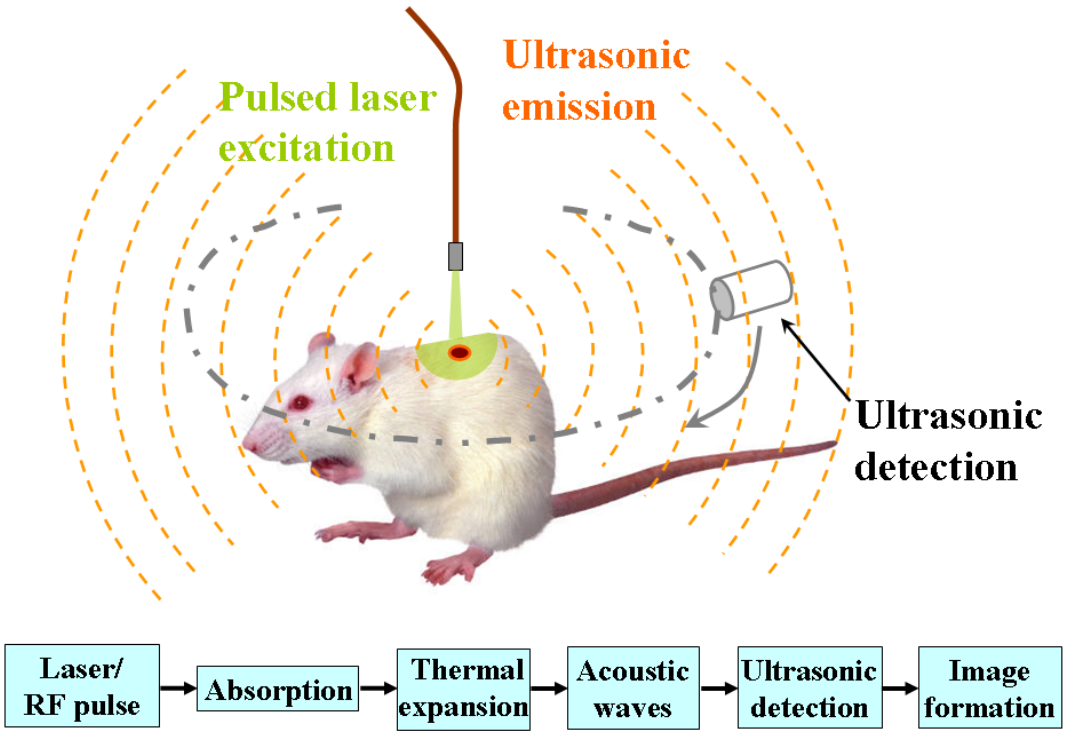

Figure 1-4 Principle of photoacoustic imaging

The PA signal strength depends on the absorption of laser radiation by the sample; as a result, photoacoustic imaging combines the better contrast and resolution of optical imaging with the superior depth penetration afforded by ultrasound imaging[47-49]. In order for thermoelastic expansion to occur, energy deposition needs to be faster than the characteristic time for thermal diffusion, τ_{th}:

$$\tau_{th} = \frac{d_c^2}{\alpha_{th}}$$ **Equation 1**

in which, α_{th} is the thermal diffusivity (m^2/s) and d_c is the characteristic dimension of the heating region. Similarly, under stress confinement conditions, the laser pulse width must be shorter than the stress relaxation time, τ_s:

$$\tau_s = \frac{d_c}{v_s}$$ **Equation 2**

in which, ν_s is the speed of sound in the medium. Under both thermal and stress confinement, the amplitude of the signal observed is dependent only on the total amount of energy absorbed. The pressure wave generation is given by:

$$p = \Gamma * \mu_a * \delta$$ **Equation 3**

in which, Γ is the dimensionless tissue Grüneisen parameter, μ_a is the absorption coefficient, and δ is the energy fluence.

1.6 Thesis Organization

This work builds on previous work in our lab of understanding and characterizing the photophysical processes leading to optical modulation of select organic dyes. It focuses on improving sensitivity of fluorescence imaging techniques as well as photoacoustic imaging techniques by exploiting unique photophysical properties. Chapter two describes the experimental methodologies used, including descriptions of data acquisitions and simulations. Chapter three introduces the xanthene dye family and describes the

photophysical properties investigated that make these dyes ideal for optical modulation. Chapter four builds on the dark state photophysics of xanthene dyes and uses both experimental and theoretical techniques to understand the optically activated delayed fluorescence (OADF) observed and investigates possible signal improvement schemes. This chapter also investigates the possible modulation routes present in merocyanine 540. Lastly, Chapter 5 introduces optical modulation as it relates to photoacoustic imaging and shows its application using both single element detectors and commercially available array ultrasound detectors. Ex-vivo animal studies are also presented here.

CHAPTER 2. EXPERIMENTAL METHODOLOGY

2.1 Sample Preparation

2.1.1 Solution and Immobilized samples

Xanthene dye experiments were conducted in both solution and polyvinyl alcohol (PVA) immobilized environments. Xanthene dyes were purchased from Sigma Aldrich and used without further purification. Deionized (DI) water was obtained after passing through a Nanopure millipore filter (17.8Mohm). All solutions were prepared by dissolving dyes in deionized water to make a 10mM stock solution and diluted to desired experimental concentration. Because of its pH sensitivity, fluorescein samples were prepared at pH 7.4 in phosphate buffered saline. PVA solutions were prepared by dissolving 15%wt PVA (MW98000) in deionized water at 60^0C under constant stirring. Immobilized samples were prepared by mixing dye with PVA solution to achieve desired concentration, then drop casting onto a glass slide and allowing to air dry in a dark environment (approx. 2hrs). Slides were then used, as is, to conduct experiments. For photoacoustic experiments, the sample prepared was approximately 3-5 layers thick with a final poly(methyl methacrylate) (PMMA) layer, 30%wt/v in toluene, was drop casted on to slide ensuring that all the sample was completely covered. This was done to prevent the drop casted PVA layer from dissolving during experiments, as it was fully submerged in water for photoacoustic measurements.

2.1.2 Phantom Preparation

Phantoms were produced from sodium alginate Protanal LF 10/60 (FMC Biopolymer, Drammen, Norway), a transparent, low viscosity alginate with a mean

guluronate/mannuronate (G/M) ratio of 70% and mean molecular weight of 180 kDa. Sodium alginate powder was dissolved in deionized water under and dye was added until desired concentration was achieved. The mixture was poured in a template and submerged into a crosslinking solution of 30% wt/v calcium chloride solution for approximately 15 minutes resulting in solid calcium alginate phantoms.

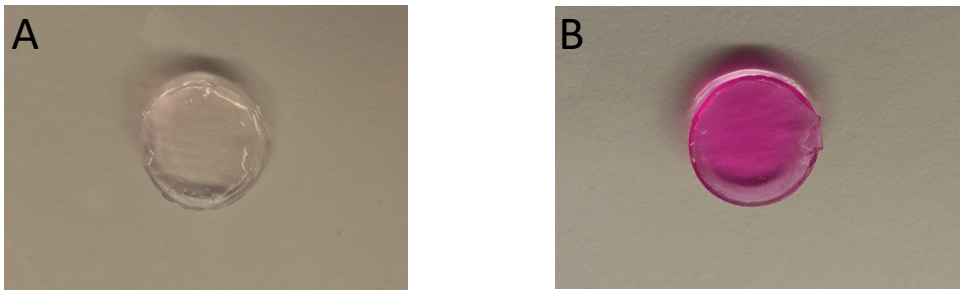

Figure 2-1 Alginate phantoms without rose bengal (A) with rose bengal (B)

2.1.3 Optically Modulatable Silica Nano-particle Synthesis

In order to achieve targeted high concentrations of modulatable dye it was necessary to encapsulate dyes in a polymer matrix. Rose bengal was selected as a representative dye to be studied for encapsulation. Rose bengal-doped silica nanoparticles (RB-SiO_2NP) were made using a capped mesoporous silica synthesis process. In brief, 200mg of cetyltrimethylammonium bromide (CTAB) was dissolved in 95mL of DI water. 0.8mL of rose bengal (5mg/mL) and 0.7mL of sodium hydroxide were added to the solution. The reaction was heated to 80^0C and allowed to stabilize for ~1 hour after which 1mL of tetraethyl orthosilicate (TEOS) was added under constant stirring. After 2 hours another 1mL aliquot of TEOS was added dropwise to limit formation of additional silica seeds. The reaction was allowed to proceed for another hour. Particles were centrifuged and washed three times to remove unreacted dye, and finally suspended in water.

Rose bengal-doped silica nanoparticles were also made using a modified stober process where rose bengal was covalently linked via the carboxylic acid moiety on the dye to (3-aminopropyl)triethoxysilane (APS) forming a thiourea linkage. The rose bengal to APS conjugation was done by mixing rose bengal (~10µmoles) with and excess APS (0.5mmoles) in a 0.1M solution of 2-morpholin-4-ylethanesulfonic acid (MES) buffer. 1-Ethyl-3-(3-dimethylaminopropyl)carbodiimide (EDC) was used as a carboxyl activating agent in order to facilitate coupling to the primary amine on the APS. This reaction was allowed to proceed in the dark for 12 hours under constant stirring. Because the silica particle formation proceeds in ethanol solution the water from the dye-APS adduct was removed by freeze drying and was redissolved in ethanol. Figure 2-2 shows the experimental procedure for making the silica nanoparticles after the initial dye-APS conjugation.

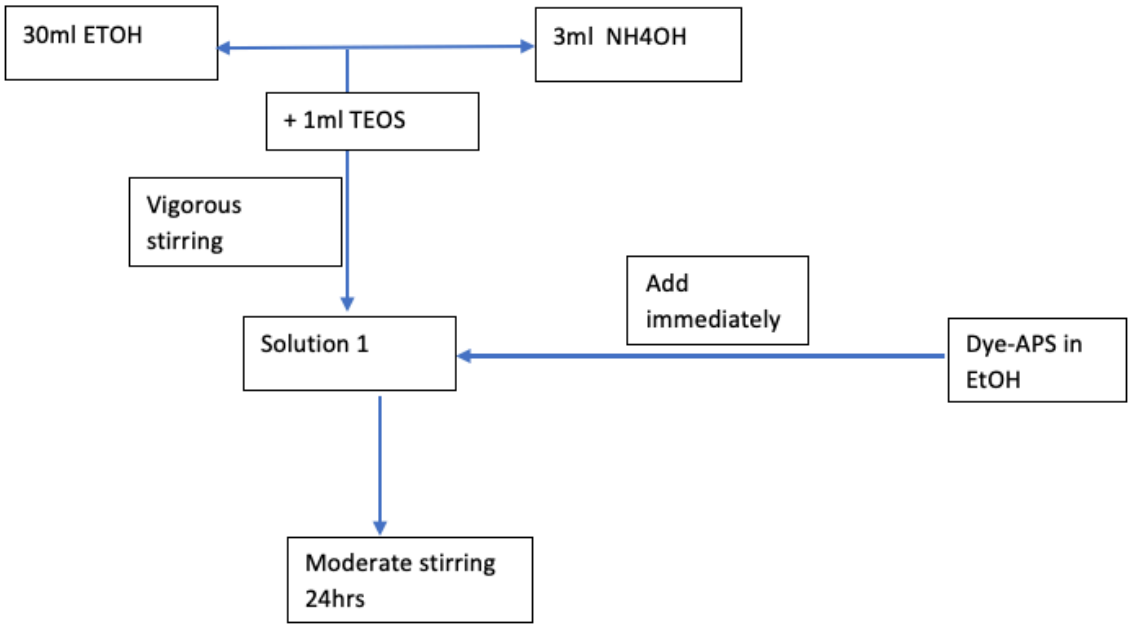

Figure 2-2 Procedure for making dye doped silica nano-particles

2.2 Bulk Fluorescence Microscopy

Bulk optical properties such as characteristic absorption and emission wavelengths, for dyes used was investigated using UV-visible absorption spectrometer (Shimadzu UV-2401 PC spectrophotometer). Fluorescence was acquired using a fluorimeter equipped with a xenon arc lamp and detector sensitive out to 900nm (PTI quant maser 40). Data was collected from solutions in a disposable plastic cuvette with a 1cm path length.

Fluorescence microscopy experiments were done on an inverted microscope, Olympus IX70 or IX71. Excitations were aligned into the back of the microscope and directed onto the sample via an objective lens (60x immersion objective or 40x air objective). A CCD camera (Andor Ixon) was used to check alignment and size of the beam. Epi-fluorescence is passed through the same objective and, by using appropriate emission filters and dichroic mirrors, is then directed through a 100μm multimode fiber to an avalanche photodiode (APD) detector. Collected fluorescence is recorded on either a Becker Hickl SPC-630 or Becker Hickl SPC-830 operating in reverse start/stop and FIFO modes as well as a National Instruments NI PCI-6602 fast counting board with in-house built acquisition software previously created by Jung-Cheng Hsiang, a former lab member.

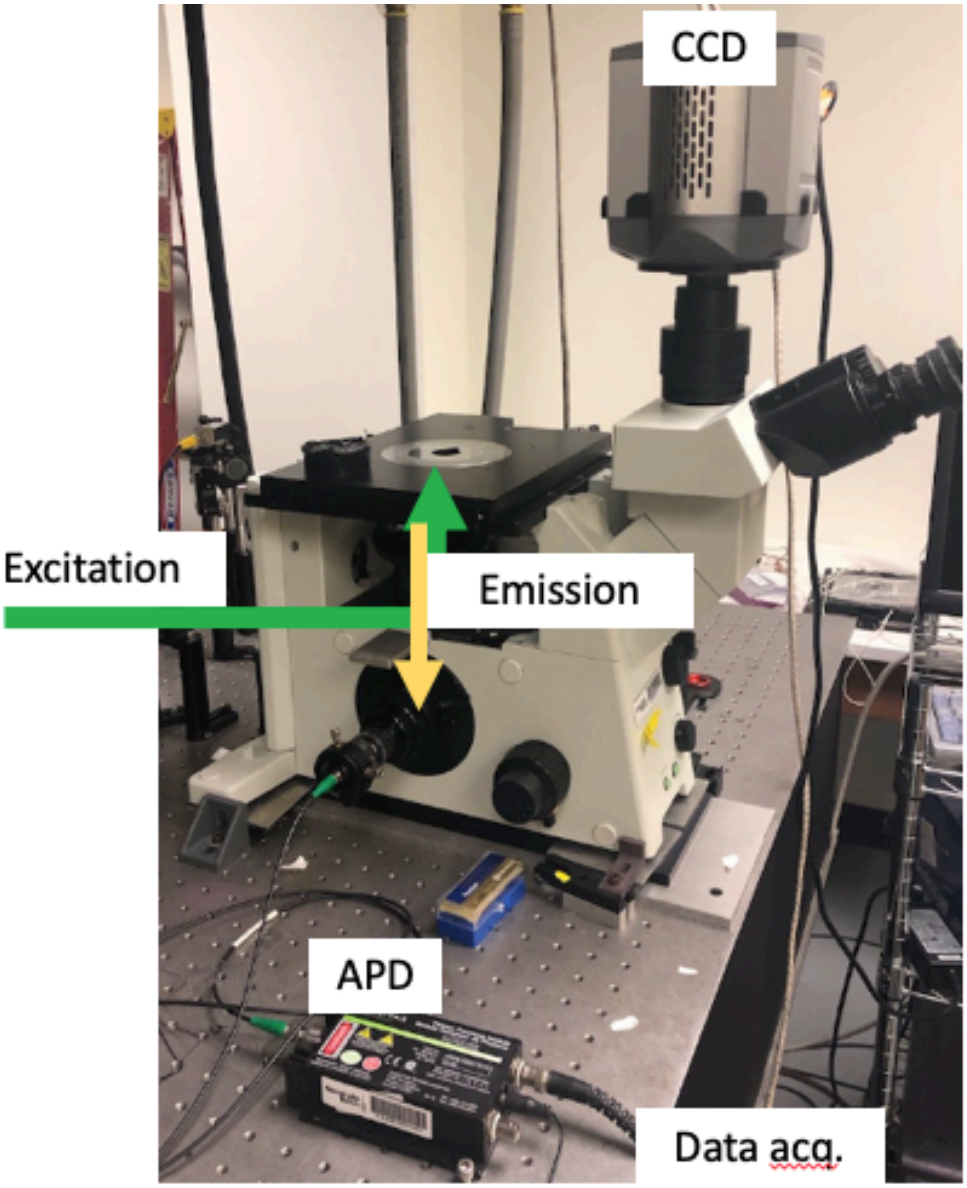

Figure 2-3 Microscope setup used for typical fluorescence experiments.

As excitations sources, lasers were employed and selected to match the absorption properties of the investigated dyes. Several types of lasers were used depending on the measurements. Table 2-1 gives a summary of fluorescence experiments for xanthenes and the corresponding excitation sources utilized.

Table 2-1 Excitation sources used for xanthene fluorescence experiments.

Dyes	Excitation type	Laser used
Rose bengal, Erythrosin B Eosin Y	CW Primary	543nm He-Ne (Melles-Griot, JDS Uniphase
	CW secondary	830nm Diode (Thorlabs, fiber-coupled) Ti:Sapphire (Coherent Mira 900)
	Pulsed Primary	532nm Diode (Picoquant, pulsed 100ps)
	Pulsed Secondary	830nm Diode (Picoquant, pulsed 100ps)
Fluorescein	CW Primary	488nm Argon ion (Coherent)
	CW secondary	637nm Diode (Thorlabs, fiber-coupled)
	Pulsed Primary	467nm Diode (Picoquant, pulsed 100ps)
	Pulsed Secondary	647nm Diode (Picoquant, pulsed 100ps)

2.2.1 Optical Modulation

2.2.1.1 Experimental Setup

Optical modulation was done by using both one and two laser schemes. For two laser schemes, primary and secondary excitation beams were combined on a dichroic mirror prior to entering the microscope. If the measurement is performed on an immobilized sample, a combination of half wave plates and polarizers are used to ensure identical polarization of beams. This is done by placing a polarizer before the microscope,

but after the two beams are aligned. The polarizer is adjusted such that power for the primary laser passing through it is maximized. A half wave plate is placed in the path of only the secondary laser and is adjusted such that the secondary polarization is aligned with the primary. Similarly, the half wave plate can also be used to adjust the primary polarization in order to match the secondary. The beams are focused through an objective onto the sample and x-, y- and z-axis alignment of the two beams is confirmed by the camera. Figure 2-4 gives a schematic overview of the beam paths and optical setups used for a typical optical modulation experiment.

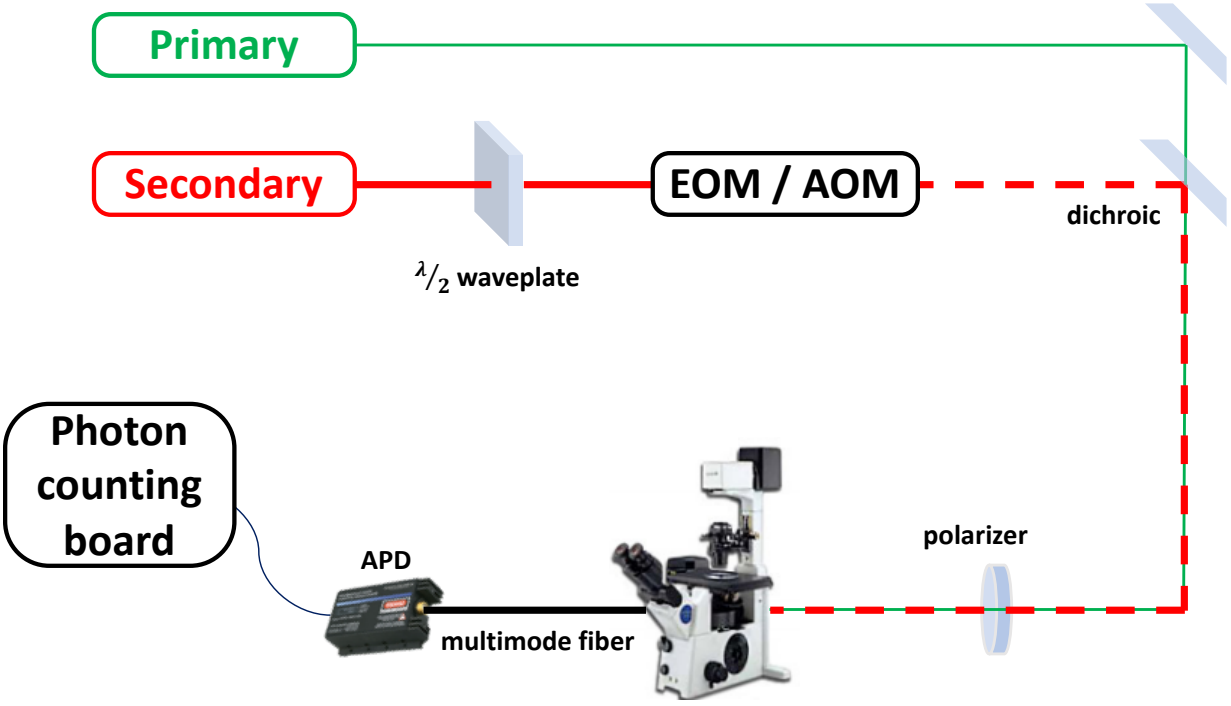

Figure 2-4 Experimental setup for typical fluorescence modulation experiments.

For modulation experiments, the beams are chopped using either an electro-optic modulator (EOM; Conoptics model 350) or an acousto-optic modulator (AOM). EOMs used were intensity modulators with a potassium dideuterium phosphate crystal serving as

the electro-optic media connected to drive the controlvoltages the crystal receives. An alignment tool is used to ensure most of the beam is going through the EOM crystal prior to placing the EOM on the mount. Adjustment knobs found on the mount can be used to fine tune the alignment through the EOM crystal in order to reach a rejection ratio (intensity of light exiting the EOM at max voltage vs min voltage) >100. A function generator is used to modulate the driver, and as a result, the EOM. Both square and sine waves can be used to achieve this modulation.

In some cases, AOMs were used to modulate lasers. In contrast to EOMs, AOMs make use of the acousto-optic effect whereby the refractive index of a crystal can be modified by an oscillating mechanical strain from a sound wave. A radio-frequency (RF) diver is used to send signal to a piezoelectric transducer attached to the crystal which generates sound waves that in turn create strain resulting in a change in the refractive index of the crystal, and therefore diffracting incoming light. As with EOMs, a function generator can be used to supply a modulated signal to the AOM driver. Alignment through the AOM is accomplished by a fine adjustment knob, until a rejection ratio usually >500 is achieved.

A

B

C

D

Figure 2-5 Picture of A) EOM and driver B) AOM and driver C) delay generator D) Function generators used in modulation experiments

Several modulation schemes were employed in order to extract the photophysical properties of the dyes. The setup used for Pulsed primary CW secondary with a <100kHz repetition rate and the setup for a simultaneous fluorescence/phosphorescence (fast lifetime/ slow lifetime) measurement are given below in Figure 2-6 and Figure 2-7 respectively. The delay generator shown is optional and is used when recording slow repetition rate signals on a short time window as is often the case for recording signals with higher resolution. In such situations where the repetition period is longer than the acquisition window the delay box is used to shift the pulse (which can appear anywhere within the repetition period) to appear in the window of the acquisition. Adjusting the cable length used for connections would accomplish similar goals but with less flexibility.

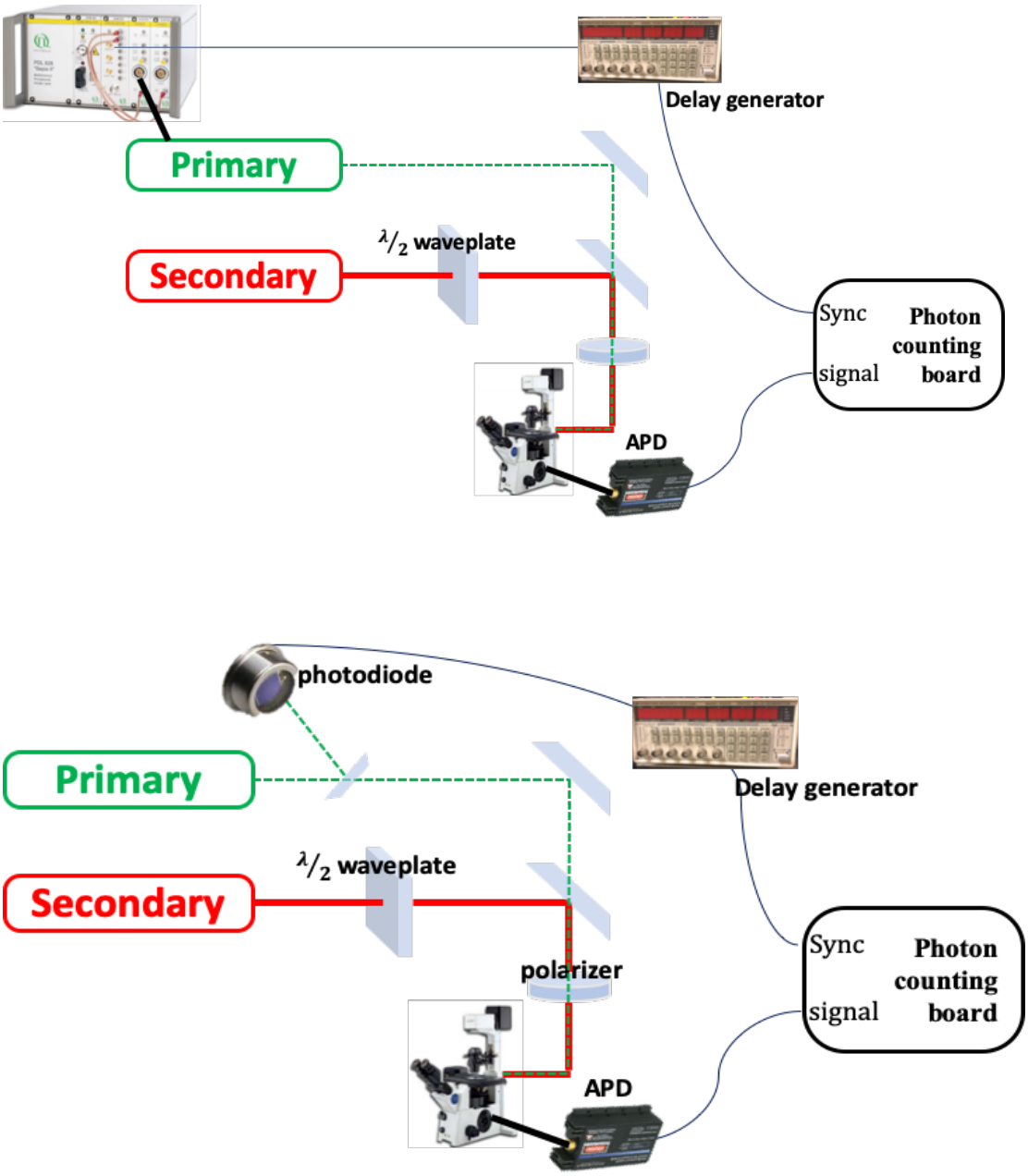

Figure 2-6 Schematic showing pulsed primary cw secondary experimental setup when A) there is a sync out signal from laser (picoquant) and B) no sync connection available (uniphase).

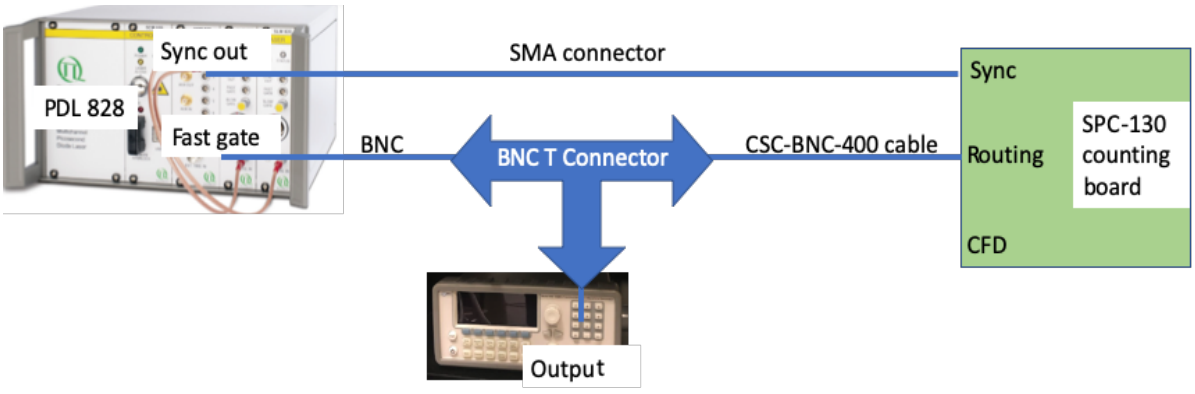

Figure 2-7 schematic for simultaneous fluorescence/phosphorescence lifetime measurement.

2.2.2 Time Correlated Single Photon Counting

Time correlated single photon counting (TCSPC) is a technique often employed for time resolved fluorescence measurements. The basis in TCSPC lies in its ability to detect and record the arrival of a single photon, relative to a reference signal, often coming from a sync signal of the excitation source. TCSPC measurements are often performed using fast repetition rate pulsed lasers (1-100 MHz), typically with pulse durations in the femtosecond to picosecond range and detectors with high sensitivity. As exemplified in Figure 2-8, each photon signal that the detector receives is digitized and builds up a photon distribution histogram that represents the waveform of the measured signal, often fluorescence.

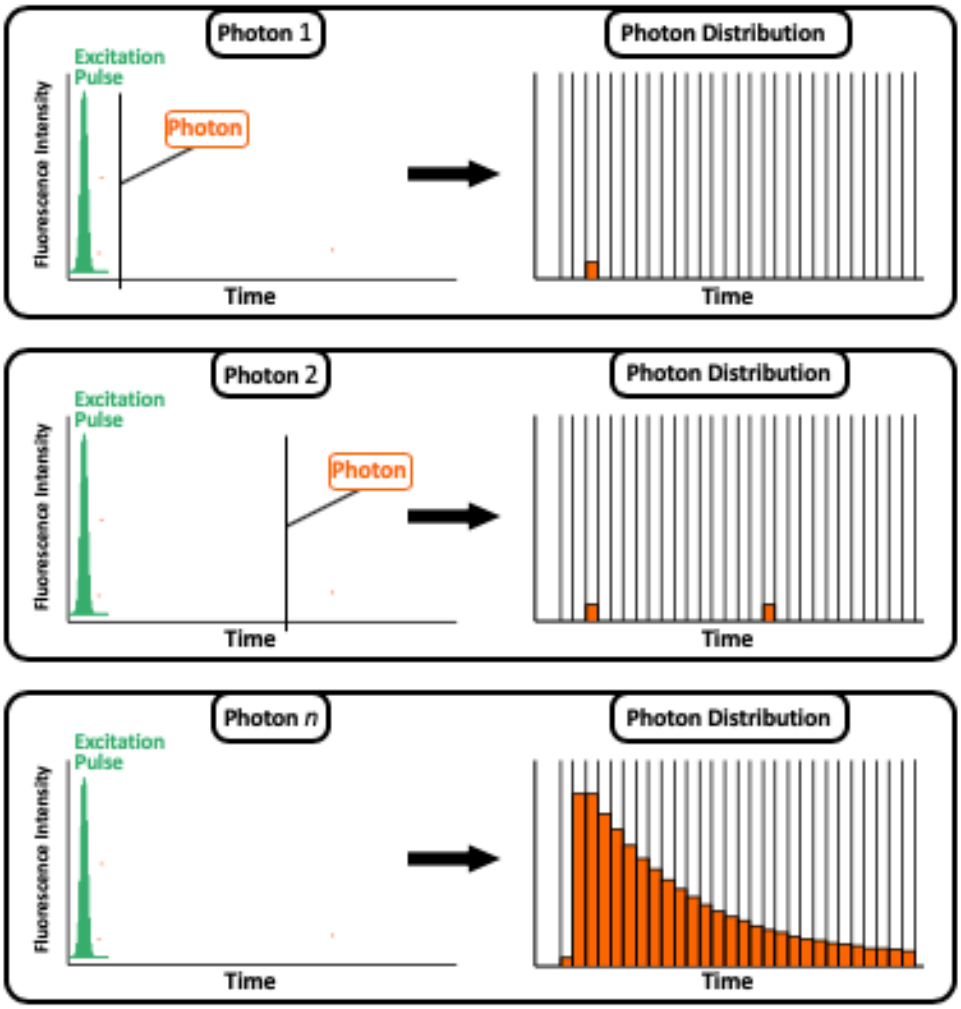

Figure 2-8 Diagram of the principle behind time correlated single photon counting (TCSPC) acquisition

Generally, TCSPC boards have two inputs that serve as the start and stop points in each cycle and correspond to the laser firing (reference) and the detection of a photon (emission). The histogram in TCSPC measurements are formed over several excitation-emission cycles in which the time difference between the reference signal and the emission photon is recorded for each cycle. Because photon detection at a certain time is random, it can be described in terms of a probability distribution. Figure 2-9 shows a simple schematic of a typical TCSPC setup. Because of the low probability of photon detection in

some applications, the reverse start/stop method is employed where a photon detection is used as the start signal and the laser sync signal as the stop.

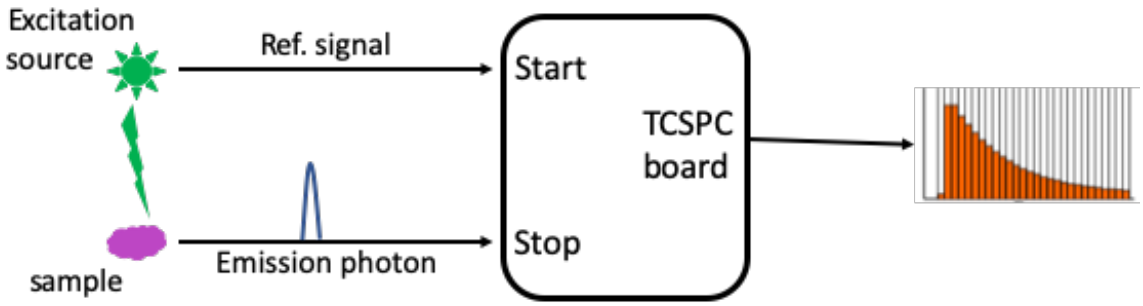

Figure 2-9 TCSPC inputs and electronics

2.3 Photoacoustic Experimental Setups

2.3.1 Photoacoustic Microscopy

2.3.1.1 Pulsed primary CW secondary excitation

PA signals were generated using a pulsed primary laser that satisfies both thermal and stress relaxation time conditions.[50-51] Pulsed primary 532nm laser (JDS Uniphase) operating at a 10kHz repetition and lower energy CW secondary co-illumination 830nm (Thorlabs fiber coupled diode) were used for photoacoustic signal generation and signal enhancement, respectively. Excitation beams were spatially combined outside the microscope on a dichroic mirror such that they overlapped at the microscope focal plane inside the phantom. The secondary laser was mechanically chopped at 1 kHz. The CW secondary laser alone does not generate PA signals. Photoacoustic signals were detected by a broadband submersible piezoelectric transducer with central frequency 10MHz (U8427003, Olympus NDT Inc, USA), amplified with a broadband amplifier (U8120004, Olympus NDT Inc, USA)

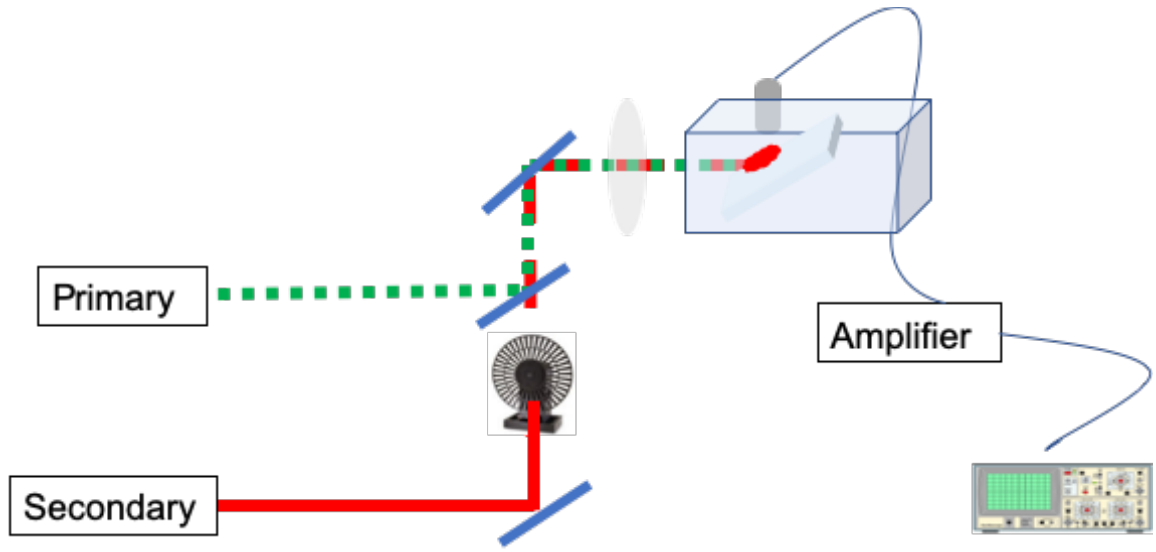

Figure 2-10 Experimental setup for pulsed primary CW secondary photoacoustic modulation

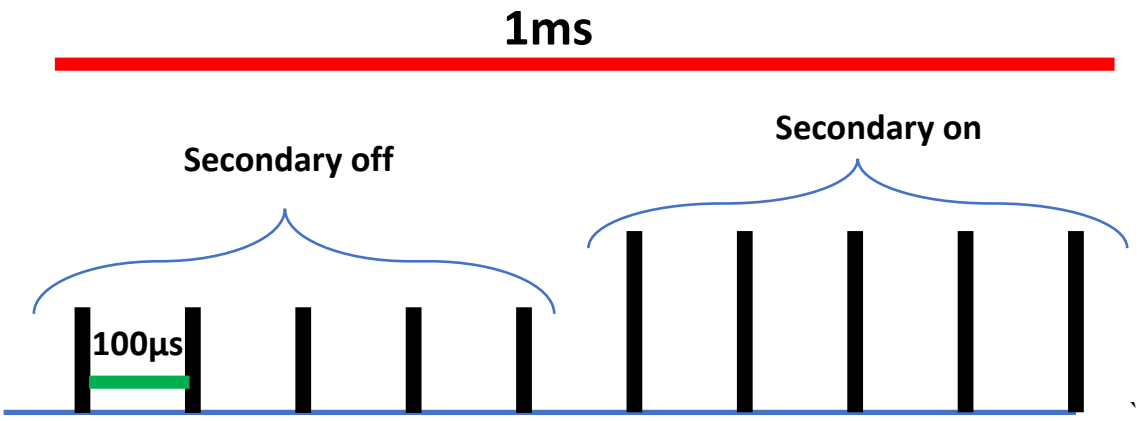

Figure 2-11 Schematic of photoacoustic signal response upon secondary laser modulation.

2.3.1.2 Pulsed primary pulsed secondary excitation

Photoacoustic microscopy measurements were done using a single element transducer with the sample immersed in a water tank for acoustic coupling. PA signals were generated using a sequential 532nm (SOL532-20, RPMC) laser followed by 1064nm

(SOL1064-40, RPMC) laser pulses operated at a 5kHz repetition rate with a pulse duration of 10ns for each. Signals were detected using a 3.5MHz center-frequency single-element ultrasound transducer (Olympus). The excitation beams were spatially combined on a dichroic and focused by a 10x microscope objective. The sample placement was adjusted to control the laser spot size. The RF signals were amplified and filtered using an ultrasound receiver (Olympus), and digitized with a 12-bit, 200MHz digitizer (National Instruments). A filter matched to the transducer's response was used to clean up the signal prior to envelope detection. Because the sample is flat, signals were treated as only appearing from a single point in time and any signal outside this range was treated as noise. The full set of responses becomes, in effect, a temporal recording sampled at 5KHz, with each data point corresponding to the PA response from an individual pulse.

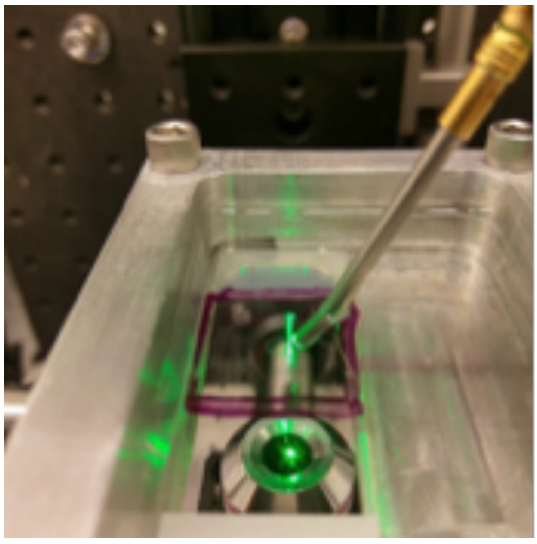

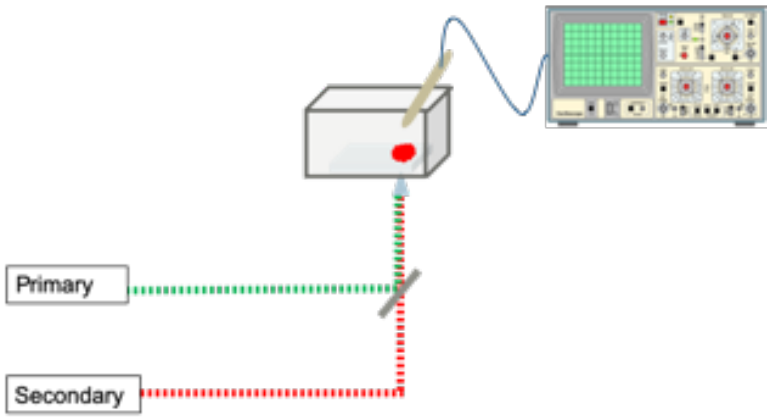

Figure 2-12 Photoacoustic imaging setup showing the sample stage (top) and typical beam path (bottom). Primary laser used 532nm pulsed and secnodary was 830nm CW or 1064nm pulsed

The modulation of the PA signal was done using both single modulation and dual modulation schemes. Single modulation was done by simply turning the primary laser (532nm) on and off at known intervals and recording the PA signals generated at 1064nm with and without the presence of the priming pulse.

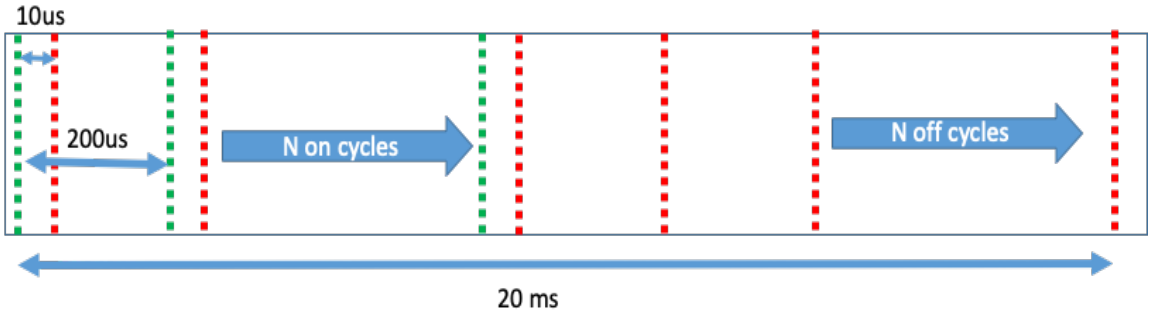

Figure 2-13 Photoacoustic modulation sequence for single laser modulation. Green line indicates pulsed primary (532nm) with red line representing secondary or probe (1064nm) pulse. The delay between primary and secondary was adjusted to limit overlap of signals

Photoacoustic modulation was also achieved by amplitude modulating both primary and secondary pulses. This was achieved by placing two beam choppers in each

of the beam paths before they were combined into one optical axis. Primary and secondary modulation frequencies were chosen to be arbitrary non-harmonic frequencies, however, as the chopper creates rectangular temporal modulation, harmonics will also be present. Primary and secondary modulation frequencies of 23Hz and 129Hz were employed, respectively. Fourier transforms of dual modulation schemes of our optically modulatable dyes yield PA signals that correspond to the sum (ν_+) and difference (ν_-) of the modulation frequencies of the two lasers, whereas un-modulatable absorbers such as blood only have signals at each individual modulation frequency, not the sum and difference frequencies.

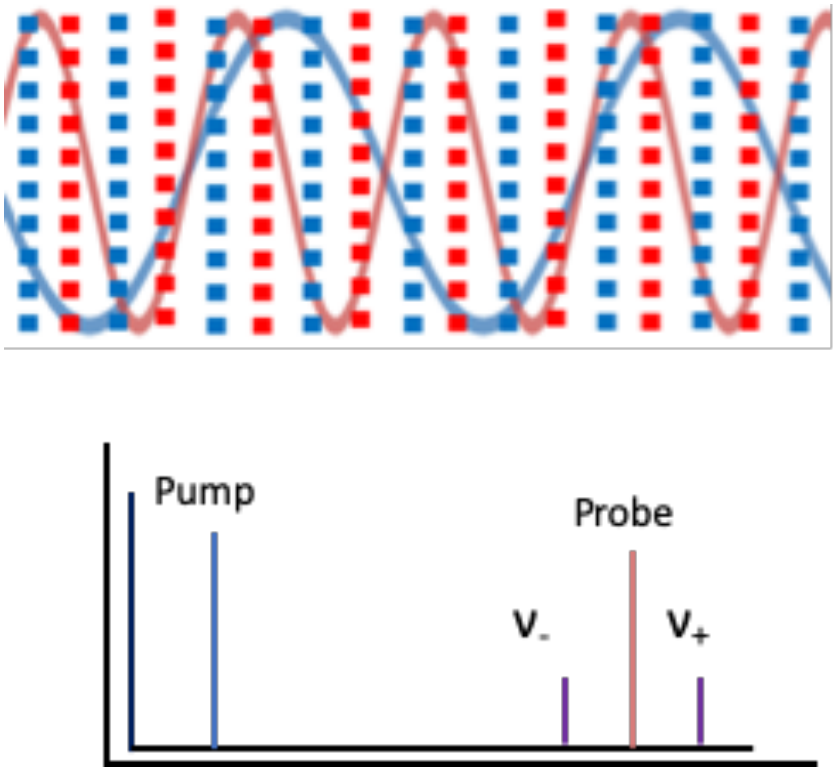

Figure 2-14 Dual modulation schematic of external waveforms applied to pulsed pump (blue) and probe (red) lasers operating at 5kHz (~10µs delay between pulsed) modulated at 23Hz for pump and 129Hz for probe and expected Fourier transform result of modulatable dyes

2.3.2 Array Based Photoacoustic Imaging

To perform wide field array photoacoustic imaging, we used either a commercial small animal ultrasound imaging system (Vevo 2100, VisualSonics) or a research-grade commercial ultrasound imaging system (Vantage 128, Verasonics Inc.) were used to render a B-mode photoacoustic image where a 2D image of a field of view is generated by simultaneously scanning a linear array of transducers. Two high-energy pulsed lasers (Tempest, New Wave Research, and Gemini PIV, New Wave Research) operating at 30Hz were used as the excitation sources. The setup was very similar to the aforementioned photoacoustic microscopy setup, however instead of focused light, full-field illumination was used. The optical axis was perpendicular to the B-mode plane of view of the ultrasound transducer to ensure good ultrasound and illumination overlap. Three acquisitions were taken: one photoacoustic image when both lasers fired, one photoacoustic image with only the 1064nm laser fired, and a third with only 532nm illumination. Similar to before, the 532nm radiation – when present – could be timed to arrive several few nanoseconds to microseconds prior to the 1064nm radiation. The final modulated signal was obtained by subtracting 532nm-only and 1064nm-only signals from the photoacoustic signal generated when both lasers are firing. Raw digitized data was immediately available, and software was written by Donald VanderLaan in the Emilianov group (School of Biomedical sciences) to perform image subtraction and SAPhIRe image recovery in real time, allowing for SAPhIRe images to be rendered live within 100 ms for 30 Hz laser excitation.

Figure 2-15 Picture of Vevo ultrasound imaging platform

CHAPTER 3. XANTHENE DYE PHOTOPHYSICS

3.1 Introduction

Xanthene dyes are one of the most commonly used types of fluorescent organic dyes. Fluorescein and rhodamine derivatives make up some of the most frequently used fluorescent tags. Due to the heavy atom effect, xanthene dyes that have heavy atom ring substitutions will exhibit higher triplet-state quantum yields. Higher triplet quantum yields will result in lower fluorescence making such dyes poor fluorophores, but ideal for optical modulation applications via SAFIRe.

Rose bengal (RB), Erythrosin B (EB) and Eosin Y (EY) are halogenated, fluorescein-derivative xanthene dyes with heavy atom substitutions. Generally, the more and the heavier the halogens, the greater the effect. Rose bengal, with both iodine and chlorine substitutions, has the highest triplet quantum yield in aqueous environments at 98%, while erythrosin B and eosin Y demonstrate 90% and 56% triplet quantum yields, respectively. [52-53] The large population build up in the long-lived triplet states of these xanthenes can be exploited in optical modulation schemes to give insight into the dynamics of the dark and bright states involved in the optical modulation process.

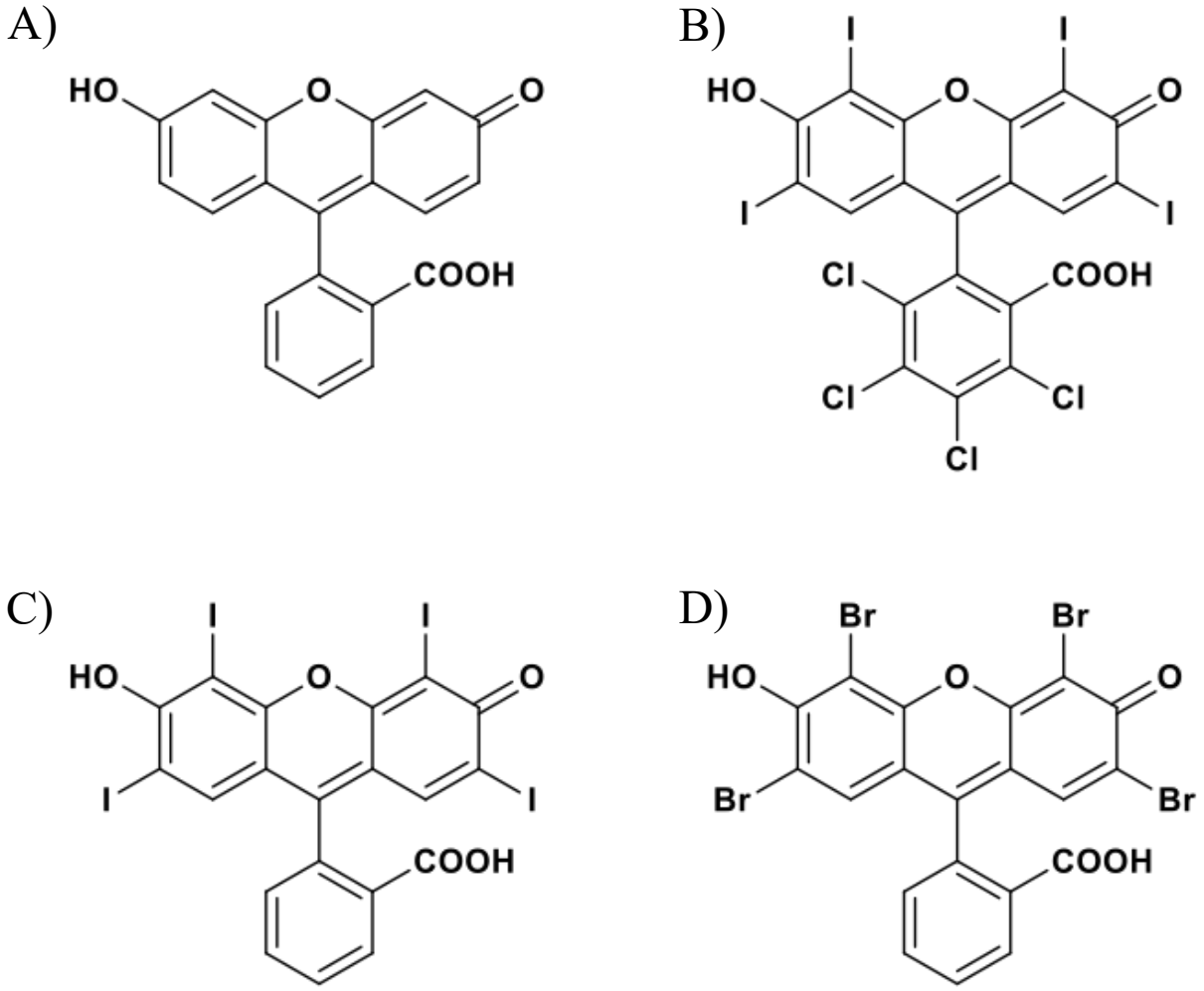

Figure 3-1 Chemical structures of investigated xanthenes. A) Fluorescein B) Rose bengal C) Erythrosin B and D) Eosin Y

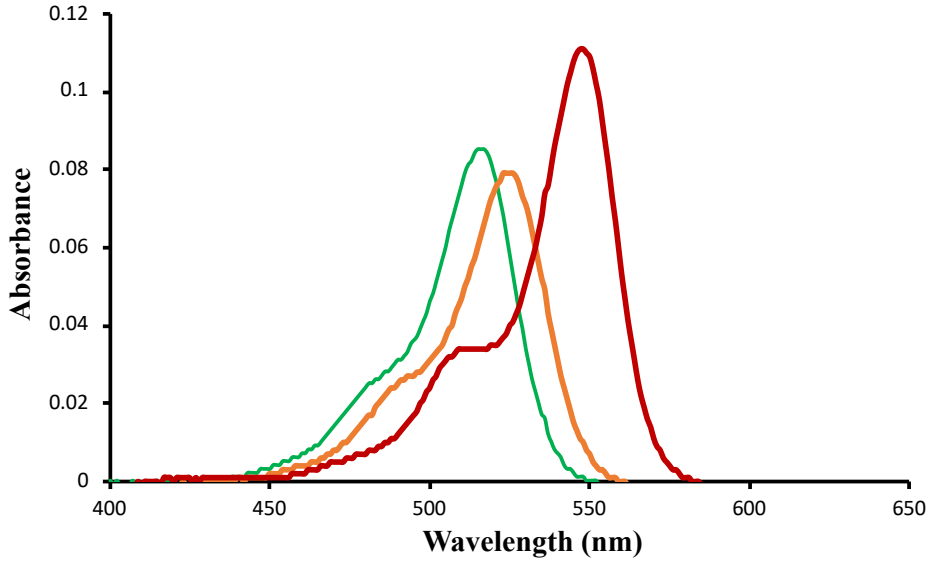

Figure 3-2 Absorbance spectra of 1µM water solutions of rose bengal (red), erythrosin B (orange) and Eosin Y (green)

3.2 Optical Modulation of Xanthenes

To understand and improve detection sensitivity, we studied fluorescein structural variants to assess how variations in environments and substituents could affect modulatability, and therefore signal recovery in high background conditions. Our specific emphasis is on understanding the bright state and dark state photophysics to enhance and tailor optically recovered ground state populations. The optimal wavelength for secondary excitation for these fluorescein derivatives has previously been investigated and shown to have significant enhancement values at secondary excitation wavelengths between 800nm and 950nm with a maximum around 900nm.[14] Enhancement in optical modulation refers to the increase in fluorescence signal upon secondary laser illumination and is given by Equation 4,

$$\frac{I_{2laser} - I_{1laser}}{I_{1laser}}$$ **Equation 4**

where I_{2laser} corresponds to fluorescence emission intensity when both primary and secondary lasers are on and I_{1laser} corresponds to emission intensity with only primary laser illumination. Because SAFIRe dyes use secondary lasers that are longer wavelength than the fluorescence no emission is expected with only secondary laser illumination. Intensity effects for the secondary laser were determined by fixing primary intensity while varying secondary intensity to determine maximum enhancement. A similar procedure was repeated to determine primary laser intensity effects on enhancement by fixing secondary intensity and varying primary intensity. Figure 3-3 shows the effects of increasing primary intensity and secondary intensity. Higher secondary intensity gives higher enhancement, whereas higher primary intensity reduces enhancement.

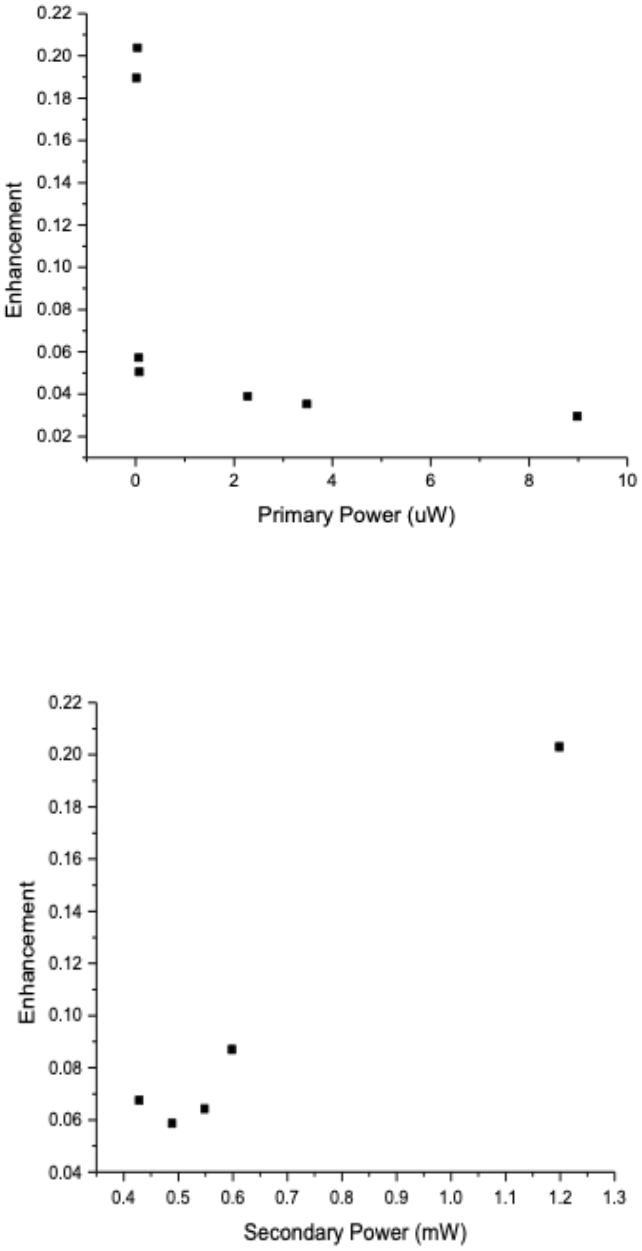

Figure 3-3 Enhancement dependence of rose bengal on A) primary intensity with secondary held constant and B) secondary intensity with primary held constant

Higher primary excitation is expected to yield higher enhancement by more rapidly populating the dark state. However, in rose bengal the reverse is observed with

enhancement only observed at low and very low primary excitation. The reduction of enhancement as primary intensity increases is most likely due to the direct primary laser-induced depopulation of the long-lived triplet state in rose bengal, leading to a reduction in the population available for secondary laser-induced depopulation. In fact, researchers have shown that the absorption cross-section of the triplet state at 532nm is comparable to that of the ground state absorption.[54] Moreover, upon using pulsed primary excitation (10kHz), the enhancement increases with higher primary excitation, further substantiating this description. This is because, when using pulsed excitation, secondary excitation can solely depopulate the triplet state in between primary pulses and without primary competition.

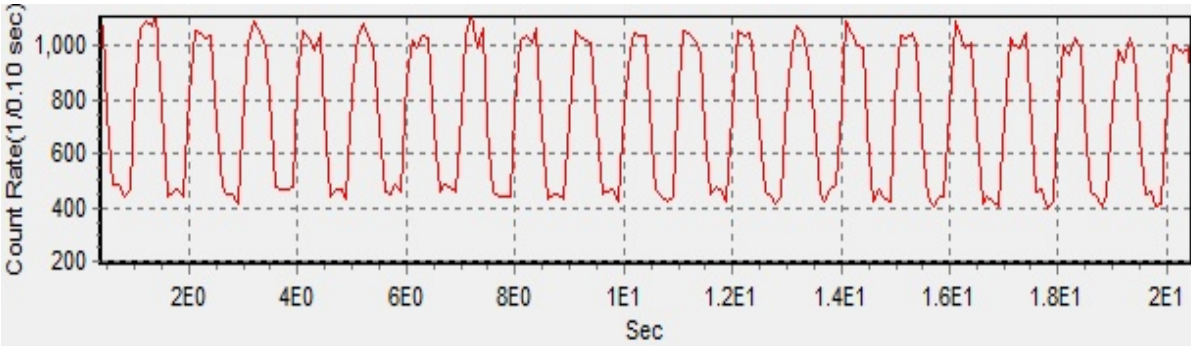

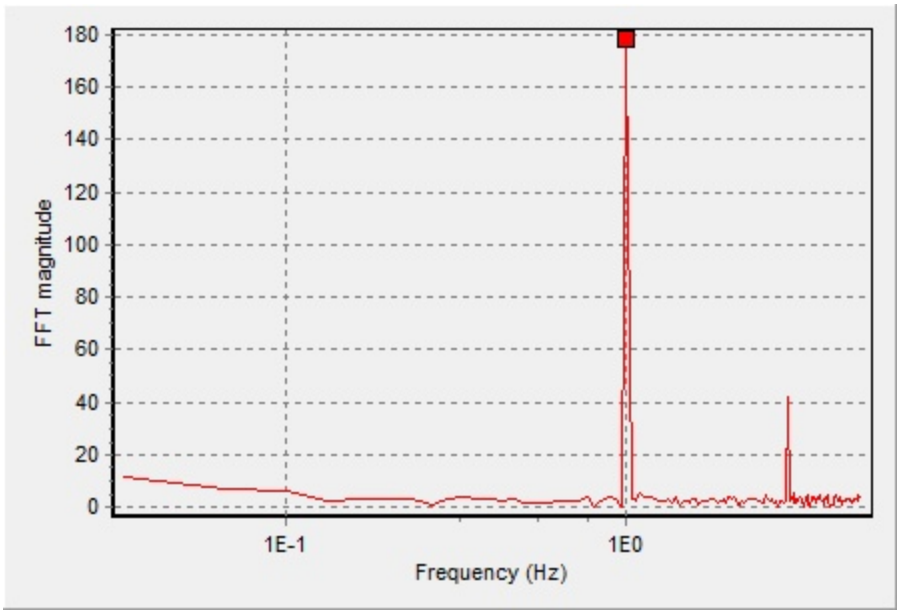

Figure 3-4 1Hz modulation of rose bengal fluorescence under 543nm primary and 830nm secondary coillumination and FFT of time domain signal showing a peak at the modulation frequency (1Hz).

The enhancement of these dyes increases with increasing triplet quantum yield with rose bengal giving the highest enhancement, followed by erythrosin B. Eosin Y, however, did not yield any enhancement and showed a decrease in fluorescence in an aerated solution due to eosin Y populating higher lying triplet states that lead to faster photo bleaching as described by Eggeling et. al.[55] When excluding oxygen during measurements, as was done by Richards and et. al., an increase in the enhancement for all dyes was observed, including for eosin Y. Since oxygen has been known to reduce significantly the lifetime of triplet states, limiting oxygen, either by flowing nitrogen throughout measurements or immobilizing dyes in a polymer matrix, provides a method for both increasing enhancement and studying the photophysical properties of dyes.

When using immobilized samples, the polarization of the excitations must be taken into consideration. Lasers produce polarized light which results in excitation of molecules

with dipoles oriented in the direction of excitation polarization. Since mobility, and therefore rotation, is restricted within immobilized samples, one must ensure that the polarity of the secondary laser is aligned with the polarity of the primary laser. If polarizations are not aligned, reduced enhancement is observed upon secondary co-illumination.

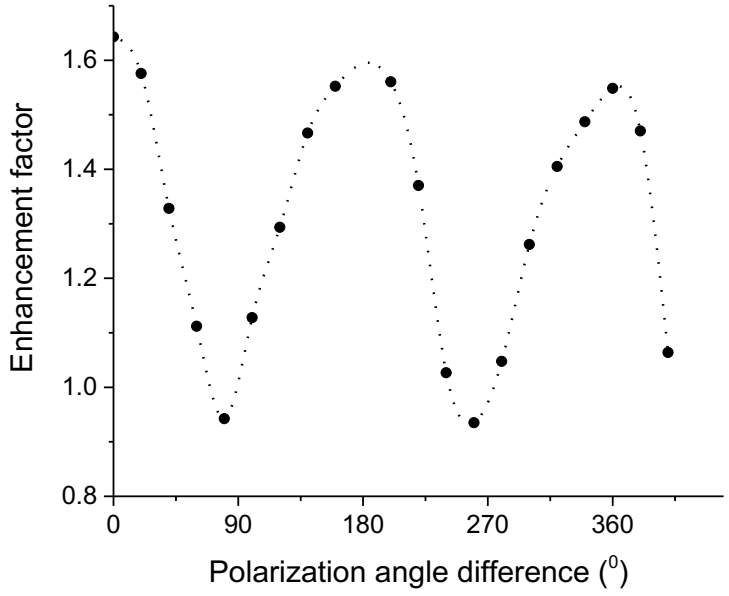

Figure 3-5 Polarization dependence of rose bengal enhancement in PVA films.

3.3 Triplet State Photophysics of Xanthene Dyes

Xanthene dye photophysics and dark state recovery were investigated to extract photophysical time scales. 1μM PVA solutions were drop cast on to a cover slip. In order to characterize the dynamics of the triplet state that gives rise to xanthene dye enhancement we employed a one laser modulation scheme similar to that done by Sanden et. al.[56] By using extended primary illumination periods one can achieve steady state triplet state populations. Upon tuning the primary laser off thermal recovery from the higher lying

triplet states repopulates the fluorescence generating manifold. This recovery is dependent on the natural decay out the dark state (τ_{off}^{o}) and the time between excitation periods, with longer off times giving higher recovery of fluorescence as the molecule has enough time to decay back to the ground state. By keeping the illumination period constant and varying the time the laser is off (T_{off}), one can affect the fraction of molecules in the bright state. This relationship is given by eq5:

$$\frac{n_B(t)}{n_{tot}} = 1 - \frac{\tau_{off}^{o}}{\tau_{on} + \tau_{off}^{o}} e^{\frac{-T_{off}}{\tau_{off}^{o}}} \qquad \textbf{Equation 5}$$

where n_B/n_{tot} is the fraction of molecules in the bright state, T_{off} is the recovery time between each excitation period and τ_{on} and τ_{off}^{o} correspond to the photophysical on and off times, respectively. By fitting the experimentally determined fraction of molecules in the bright state as a function of the laser off period (T_{off}) we can determine the natural dark state decay rate. This is illustrated in Figure 3-6 using a 543nm excitation source on PVA immobilized rose bengal. The data shows an increase in the initial intensity drop off as the time between laser periods is extended (longer off-times).

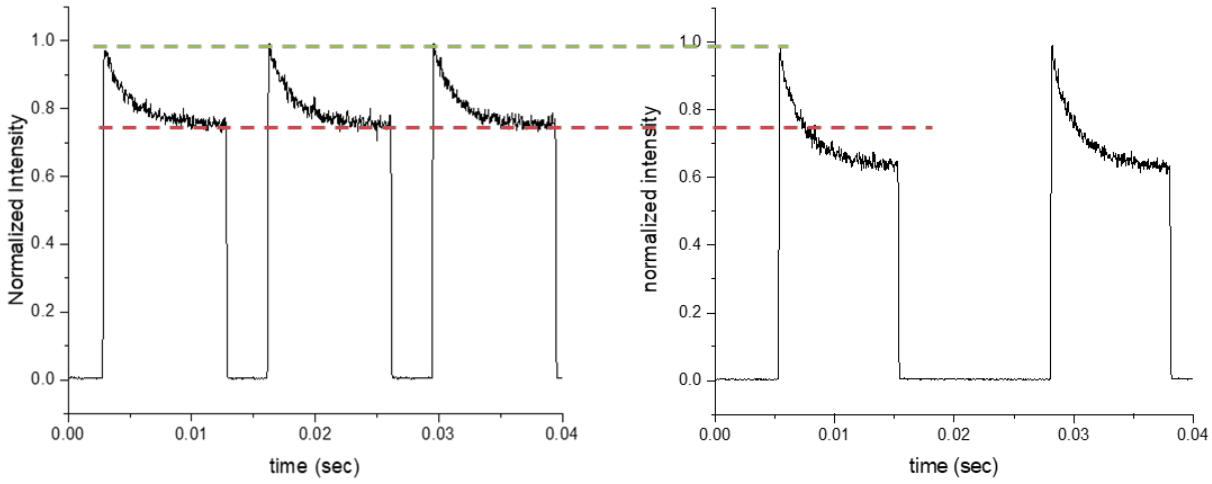

Figure 3-6 Fluorescence decay histograms showing ground state recovery for rose bengal using different primary laser off periods, T_{off}. Primary laser is turned on for 10 ms and off for A) 3 ms, B) 12 ms. For each panel, data were collected and ratios of initial to final intensities within the average primary illumination period, T_{on}, as a function of T_{off} are fit to Equation 4.

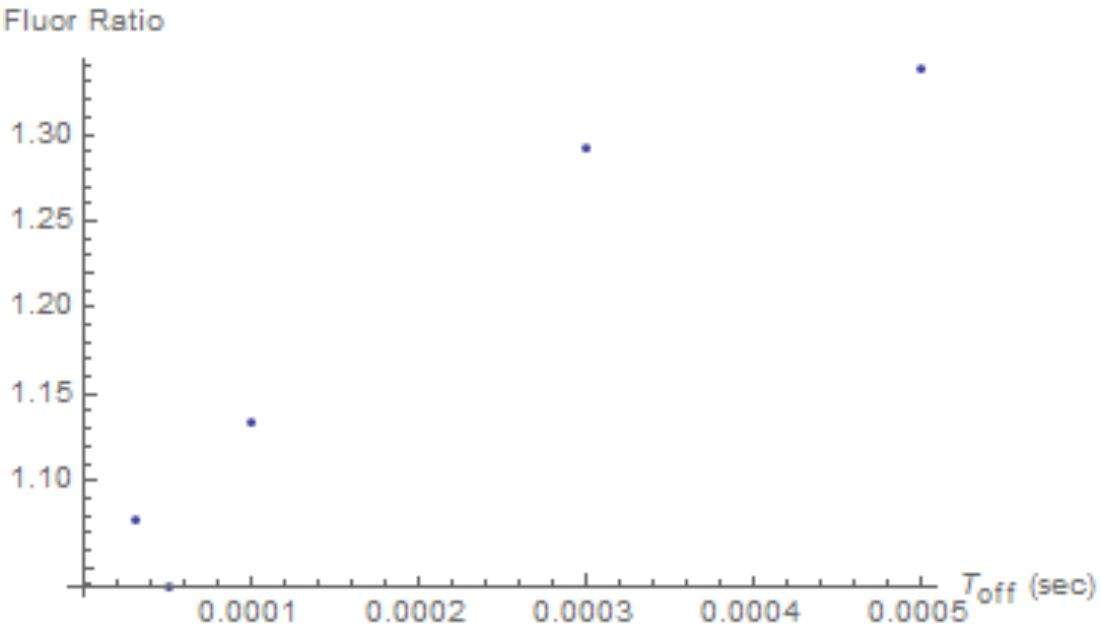

Figure 3-7 Plot of T_{off} versus fluorescence recovery ratio at different off times.

Even with the seemingly minor structural changes to Fluorescein, as indicated above, it is shown that modulation depth and photophysical parameters are strongly affected by substituent changes. Using aforementioned bright state recovery methods, photophysical timescales were extracted. Overall, modulation depth increases with increasing halogen mass, while the natural decay rate out of the dark state decreases with increasing halogen mass. The photophysical rates into and out of the dark state control the steady state dark state population. The larger the achievable steady-state dark state population, the larger the possible enhancement upon complete depopulation through secondary illumination. The results of the measurements are summarized in Table 3-1. The observed trend in the timescales show that the triplet lifetime scales inversely with the size of the halogen substituent. More over there is a large difference in the timescales in PVA immobilized dyes vs free dyes owing to the presence of higher amounts of oxygen in the latter.

Table 3-1 Summary of experimentally determined time scales for one-laser modulation of xanthenes

	τ_{off}
RB	200μs
EB	200μs
EY	4ms

3.4 Fluorescein Modulation

Fluorescein is the xanthene parent of the above dyes. Fluorescein is a highly fluorescent organic dye with peak absorption between 465-490nm and emission in the yellow-green with peak fluorescence between 520-530nm. Fluorescein fluorescence is pH sensitive with high emission attainable at pH 7.4. The high fluorescence quantum yield (~98%) of fluorescein has encouraged the use of this dye in a series of scientific and medical applications, ranging from use in ophthalmology as a stain used in observing eye surface damage[57] to intraoperative assessment of blood flow in grafts and resections.[58-59]

Modulation of immobilized fluorescein was previously reported, but at exceedingly high (MW/cm^2) secondary intensities,[55] and without identifying the nature of the states involved in such fluorescence modulation. Although fluorescein has a fluorescence quantum yield approaching 1, its halogenated derivatives rose bengal, erythrosin B and eosin Y, as previously mentioned, can produce very high triplet populations and are commonly employed as photosensitizers for their ROS generating capacities.

For modulating fluorescein fluorescence, we used a 488nm primary excitation followed by a 637nm secondary illumination, which yielded a 45% enhancement in PVA immobilized samples. A 568nm beam was also used as a possible secondary source, but did not produce any enhancement due to a larger cross-section for multistep photobleaching at that wavelength.[55] There was also no enhancement observed in solution, due to an extremely low triplet quantum yield coupled with a large oxygen quenching that limits triplet state population in xanthenes. We used a modulated 488nm laser to extract

out the natural triplet lifetime using the above method. Fitting the T_{off} versus recovery time ratio gives a natural rate of triplet decay of 12ms.

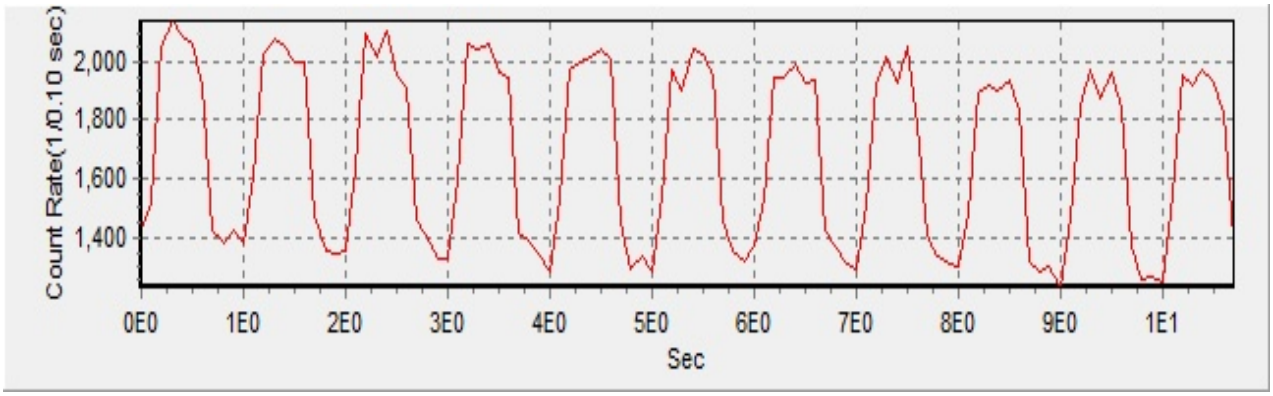

Figure 3-8 Fluorescence signal from fluorescein using 488nm primary and 1Hz modulated 637nm secondary. Data was binned at 1Hz

3.5 Conclusion

Using CW primary and CW secondary illumination, we showed that rose bengal, erythrosin B and eosin Y are all modulatable with green (543nm) primary excitation and ~800nm secondary excitation. Because modulation depth decreased with increasing primary intensity, we concluded that primary excitation also depopulates the dark state. pulsed excitation however showed no primary depopulation of the dark state as the secondary laser was able to sufficiently depopulate the triplet in between successive primary pulsed. As a result, when using pulsed primary excitation secondary-induced depopulation gives extremely large enhancements by removing the opportunity of the primary excitation from depopulating the dark state. Such pulsed-CW enhancement studies yielded strong modulation in both solution and when immobilized in PVA films.[14] Moreover, increasing molecular oxygen concentrations will lead to trplet state oxygen quenching and possible reactive oxygen generation which decreases the measured

xanthene dye triplet lifetimes (and steady-state populations), with triplet lifetimes for solutions reported to be ~2μs.

CHAPTER 4. OPTICALLY ACTIVATED DELAYED FLUORESCENCE

4.1 Introduction

Through utilization of molecular modulation schemes for optical control of dark and ground state populations, we have demonstrated up to 100-fold sensitivity improvements in fluorescence imaging by actively modulating and demodulating molecular fluorescence.[14, 26, 45, 60-61] Ideally, by absorbing at wavelengths longer than those of collected fluorescence, dark states ranging from photoisomers to triplet states can be employed because their populations compete with those of the ground state of the emissive manifold. Thus, intensity-modulated long-wavelength excitation dynamically depopulates these states, shuttling population back to the optically excitable ground state to increase primary laser-induced fluorescence emission.[12-14, 28, 60, 62]

An alternative approach to circumventing background is the use of fluorophores, with sufficiently long-lived emissive states, under pulsed excitation, then gating the signal collection to collect emission only after the shorter-lived background fluorescence has decayed away.[63-64] When dyes with long luminescence lifetimes are used, passive background removal approaches, such as time-gating, yield significant sensitivity improvements.[65] Lanthanides exhibit partially "spin-forbidden" transitions with very long-lifetimes, however these fluorophores have weak emissions that is spread out over large timescales. Alternatively, since each singlet state has a corresponding triplet level that is lower in energy thermally activated T_1 to S_1 reverse intersystem crossing becomes possible if this singlet-triplet gap is sufficiently small, allowing for a delayed fluorescence as T_1

population trickles back into the emissive S_1 state termed thermally activated delayed fluorescence (TADF).

TADF emitters generate long-lived emission in a different manner, as the ns-lived S_1 level is slowly repopulated by thermally induced leakage out of the long-lived triplet population. Increasing the singlet-triplet gap would eliminate TADF, as available thermal energy would become insufficient to repopulate a widely separated S_1 level. Chemical tuning of the triplet-singlet gap in a wide range of fluorophores has enabled TADF and triplet harvesting[66-68] effects that rely on strong coupling between excited triplet and singlet states. Providing the opportunity for time-gated detection many microseconds after most background emission has decayed away. TADF fluorophores have improved LED technology,[65-69] but they have yet to be effectively utilized in solution-based or biological fluorescence imaging. As an alternative, optically induced reverse intersystem crossing,[67, 70-71] could yield an additional active external control over the reverse process and drastically improve detection for a wide array of emitters.

Silver clusters are able to regenerate ground electronic state populations upon excitation of the dark state. Additionally, these clusters possess an additional fluorescence enhancement channel that results from optical excitation from the dark state back to the fluorescent excited state, and results in additional ns-lived fluorescence many microseconds after the pulsed primary excitation laser has passed. This optically activated delayed fluorescence (OADF) results from preparing the long-lived dark state through pulsed primary excitation, followed by near IR excitation of this dark state to regenerate the excited emissive state and high-energy fluorescence starting from the primary laser-prepared long-lived dark state. This technique has been employed successfully in FCS

studies of silver clusters to eliminate background and determine true modulatable dye concentrations in complex media.[71] Moreover, it opens the possibility of using OADF capable fluorophores for anisotropic measurements of slow-rotating proteins. Fluorophores with moderate to high triplet yields seem to be good candidates for strong OADF in organic emitters. As triplet states are likely to maintain good Franck-Condon overlaps with the emissive manifold and additionally may be excited at long wavelengths to yield reverse intersystem crossing, we investigated a family of xanthene dyes (rose bengal, erythrosin B, eosin Y, and fluorescein) for OADF.

In contrast to our previous description of enhancement as a direct pathway to the ground state from the dark state, OADF presents a more distilled understanding of the modulation paradigm. Related to previously described TADF molecules OADF dyes transition between dark and excited states due to secondary excitation. Because secondary excitation alone cannot cause excitation of molecules from the ground state, the additional fluorescence signal in OADF must arise from a secondary laser shifting population from the dark state (D_1) to the singlet excited state (S_1), which can subsequently relax to the ground state (S_0) by emitting a photon. This can be modelled using the simple three state system described before with an additional path form the dark state back to the emissive manifold (S_1).

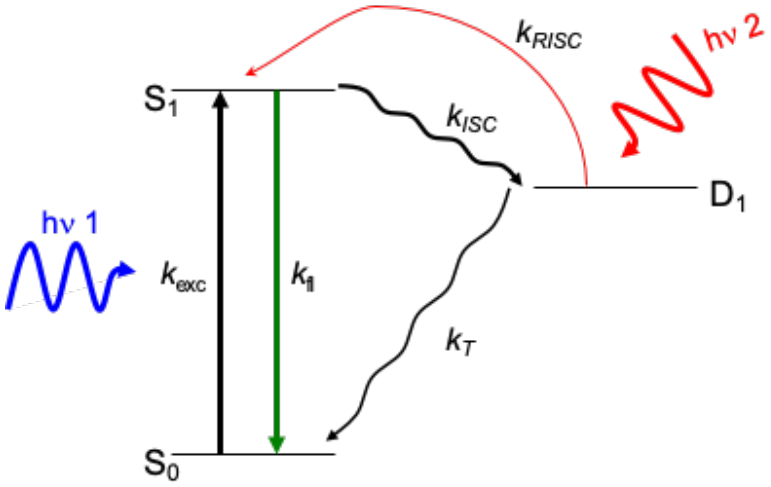

Figure 4-1 Jablonski diagram showing photophysical transitions present in OADF capable fluorophores.

4.2 OADF from Xanthenes

While secondary laser-induced repopulation of the ground state increases brightness through additional primary laser-excited fluorescence cycles, a simple Jablonski diagram (Figure 4-1) suggests that long wavelength secondary excitation could also repopulate the S_1 state to result in time-delayed, short wavelength optically activated delayed fluorescence (OADF). Larkin et. al. have previously reported on reverse intersystem crossing (RISC) from the first excited triplet state of RB to generate the singlet excited state.[52] This process of OADF, however, has remained unexplored as a competing enhancement mechanism. Both processes, OADF and direct ground state repopulation, would contribute to the overall enhancement and would therefore be difficult to distinguish with modulated CW excitations. Probing the xanthene triplet state populations with pulsed excitation clearly shows the additional fluorescence generated by optically accessing the long-lived triplet state. In contrast to our previous reports of modulated emission from rose bengal, erythrosin B, and eosin Y, secondary excitation not only produces additional

fluorescence photons by repopulating the ground state faster than it would naturally decay but can also transition back into the S_1 state to generate OADF. The same cohort of dyes can also enhance fluorescence by optically shifting dark state populations to the singlet excited state (S_1) leading to extra delayed fluorescence without additional primary excitation.

Eosin Y, erythrosine B, and rose bengal have increasingly large triplet quantum yields due to the heavy atom effect. As triplet quantum yield increases, fluorescence quantum yield decreases, rendering only fluorescein and eosin Y as reasonably bright fluorophores. The large triplet populations that can be generated under primary excitation make these ideal systems to study and utilize optically activated delayed fluorescence for high sensitivity detection. Because energy differences separating T_1 and S_1 states are typically very large, relative to available thermal energy, little to no thermally activated delayed fluorescence (TADF), resulting from thermally-induced reverse intersystem crossing from T_n to S_1, occurs. In these cases, optically induced reverse intersystem crossing may be able to efficiently regenerate the singlet excited state from the long-lived triplet leading to optically activated delayed fluorescence (OADF).

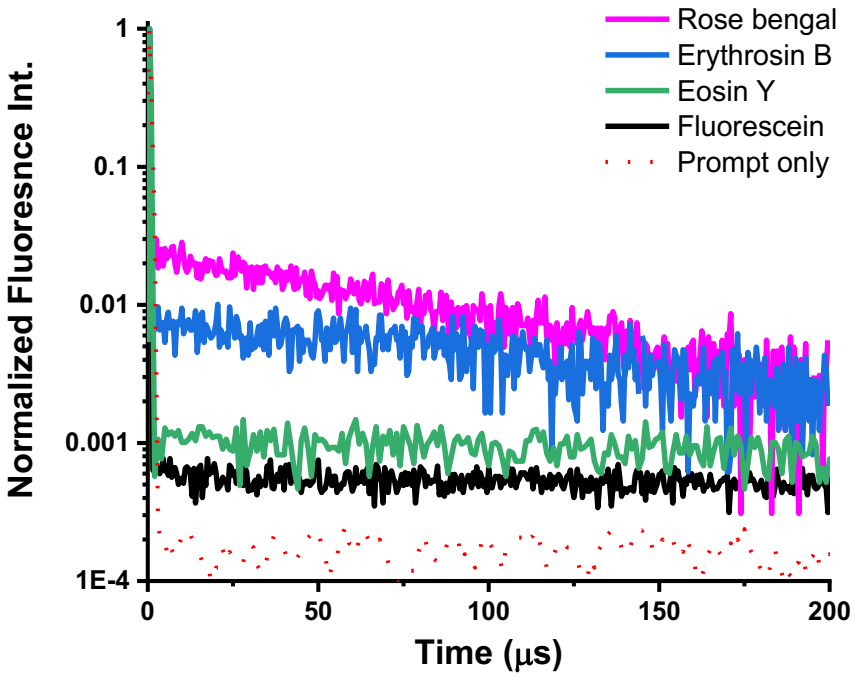

Figure 4-2 Normalized pulsed-cw fluorescence histograms of all studied xanthene dyes in PVA. OADF appears after the prompt fluorescence, with integrated OADF increasing with increasing triplet quantum yield along this series. Red dotted line shows prompt fluorescence with no OADF.

4.2.1 Pulsed-CW

As with our prior study demonstrating modulated fluorescence, a pulsed 532nm excitation source (~100ps pulse width) populates the excited singlet state which relaxes into the longer-lived triplet state. In this study, however, we depopulate the dark state with a near IR CW laser and measure the resulting orange fluorescence that arrives between the 10kHz-1kHz primary pulses – a region where no fluorescence should be seen unless re-pumped to S_1 from the T_1 state. Thus, OADF is clearly observed upon co-illumination with a second, longer wavelength laser (830nm) that excites the dark state population to the ns-lived fluorescent S_1 state. Since the secondary wavelength used (830nm) is lower energy

than the observed fluorescence (550-580nm), no fluorescence is generated with secondary illumination alone.

OADF results from the direct transition of fluorophore molecules between triplet and singlet excited states using lower energy secondary excitation. Primary excitation leads to population buildup in a long-lived dark state, with this population decaying back to the singlet ground state on some characteristic triplet time scale. However, upon secondary illumination the dark state population is re-pumped to the excited singlet manifold giving rise to additional fluorescence at delayed times. This secondary laser-induced OADF decays exponentially between each primary pulse and is directly proportional to the intensity of the secondary excitation.

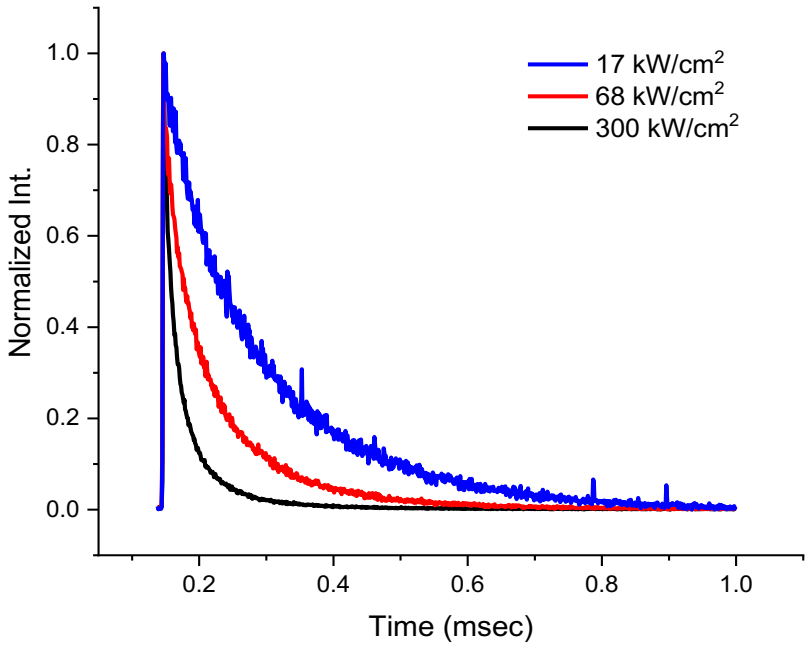

Figure 4-3 Fluorescence histogram of eosin Y in PVA films under constant pulsed primary (1kHz) excitation intensity and varying CW secondary coillumination showing that the decay constant decreases with higher secondary intensity.

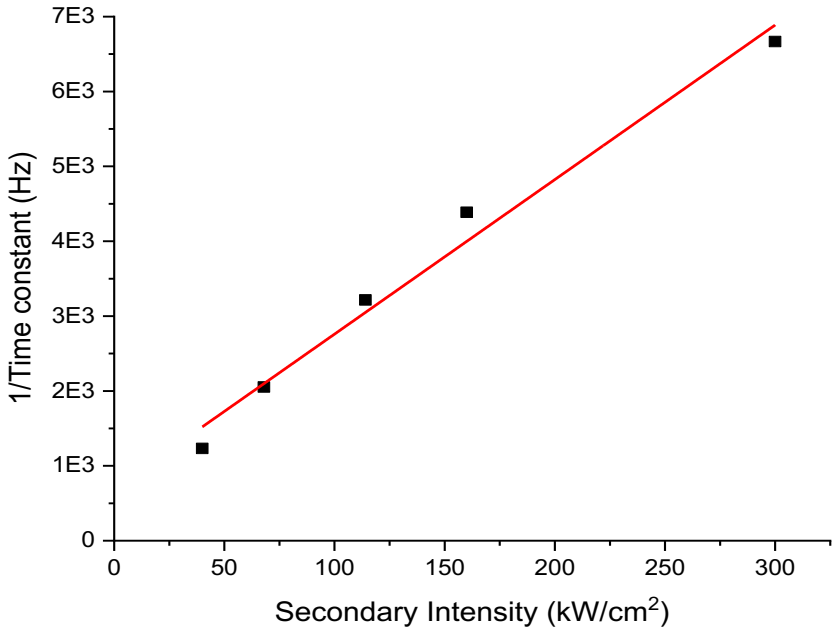

Figure 4-4 Plot of secondary excitation intensity versus inverse of decay constant for eosin Y to show their linear relationship. Extrapolating to the y intercept gives k_{off}^{0} which is the inverse of the natural triplet lifetime.

Population buildup occurs in the triplet state after pulsed primary excitation. The duration for which molecules exist this state corresponds to the inverse of the natural triplet lifetime (k_{off}^{0}). When co-illuminating with a long wavelength secondary excitation, a portion of the population in the triplet state will decay faster than the natural rate of triplet decay and is given by the product of the RISC quantum yield, the triplet absorption cross section and the intensity of the secondary excitation. The OADF decay after pulsed primary excitation is linearly dependent on the secondary laser intensity (Figure 4-3 and Figure 4-4). Higher intensities more rapidly depopulate the dark state and give higher initial OADF intensities, however integrated OADF intensities remain similar. For a given

secondary intensity, the measured rate constant out of the dark state, k_{off} is the sum of the natural rate out of the dark state (k_{off}^{0}) and the secondary induced rate and is given by:

$$k_{off} = k_{off}^{o} + \frac{\sigma_{risc} I_{\sec}}{h\upsilon} \qquad \textbf{Equation 6}$$

in which k_{off}^{0} is the natural rate constant for dark state decay, I_{sec} is the secondary laser intensity, hν is the secondary laser photon energy, and σ_{risc} is the action cross section for reverse intersystem crossing back to the singlet manifold. To investigate the relationship between secondary excitation intensity on the measured dark state lifetime (k_{off}) we measured fluorescence histograms at constant primary excitation while varying the secondary excitation intensities. The repetition rate of the pulsed primary laser used was 5kHz for rose bengal and erythrosin B, while a 1kHz repetition rate was used for eosin Y to ensure complete decay of the triplet between primary pulses. k_{off} can be determined by fitting an exponential decay function to the collected histogram. Plotting these measured rates at varying secondary intensities vs the secondary intensities yields a line with a y-intercept that corresponds to k_{off}^{0}. Although the dark state lifetime is oxygen sensitive and each halogenated xanthene has a large triplet quantum yield, we confirmed that the triplet is involved in OADF by an auxiliary measurement of phosphorescence lifetimes for comparison. Phosphorescence for each dye was measured by using multiple 532nm (100ps) excitation pulses followed by an extended off time to record the phosphorescence using a long pass emission filter that blocks fluorescence decay. The natural decay rate constant and phosphorescence lifetime for each xanthene in PVA are given in Table 4-1

Table 4-1 Triplet lifetimes of rose bengal, erythrosin B (EB) and eosin Y (EY) using 532nm pulsed primary excitation with coillumination at 830nm CW secondary.

	Triplet lifetime	Phosphorescence lifetime
RB	240 ± 24μs	316 μs
EB	420 ± 35μs	609 μs
EY	2.3 ± 0.5 ms	4.3ms
Flu*	12 ± 0.5 ms	

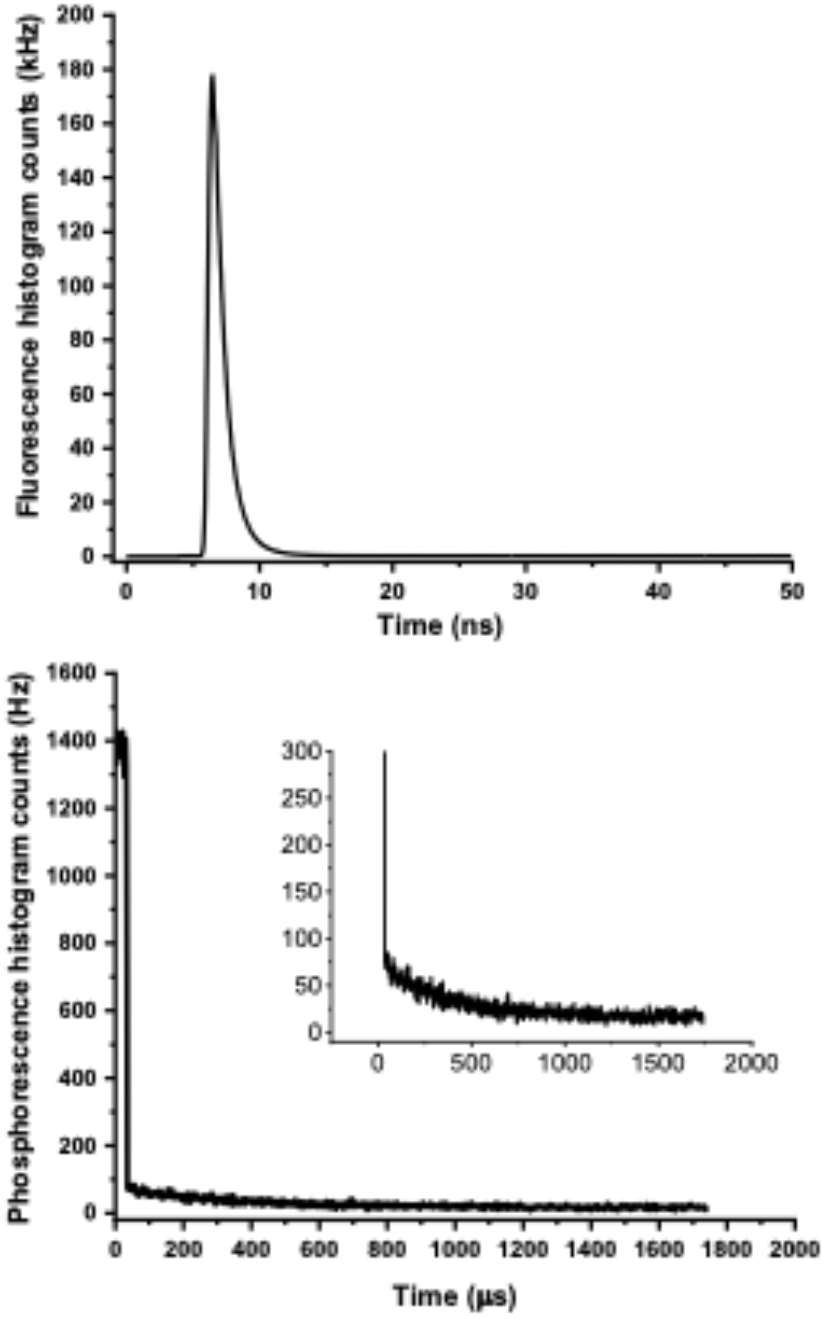

Figure 4-5 Histograms of simultaneous fluorescence lifetime and phosphorescence lifetime measurements of rose bengal in PVA. Top panel shows the fluorescence decay on a ns timescale and bottom panel shows the phosphorescence on a ms timescale.

The high fluorescence quantum yield of fluorescein yields extremely small amounts of OADF photons. Ultimately, this is insufficient to determine triplet lifetime, thus an alternate method using only a primary laser modulation was used. Upon absorption of primary laser there is a rapid decrease in fluorescence observed as molecules transitioning into the triplet state. Similar to the case described previously involving a pulsed primary CW secondary co-illumination, the lifetime of the observed fluorescence decay is a function of the rates into and out of the triplet state and depends linearly in the primary laser intensity (no secondary laser used). This scenario is described by eq.6; where I_{pri} and σ_{isc} are the primary laser intensity and the action cross-section, respectively.

$$k_{measured} = \frac{\sigma_{ISC}\, I_{Pri}}{h\nu} + k^0_{off}$$

Plotting the measured rate vs the primary intensity used will give the natural decay rate k^0_{off}, as the y-intercept. Using this method, the measured rate was found to fit to a bi-exponential decay, acknowledging that the goodness of fit is highest at higher secondary excitation intensities. The timescales were determined to be 12ms and 44ms. Considering the high photobleaching observed in PVA immobilized fluorescein, the slower time scale was assumed to represent the photobleaching rate while the time scale that was similar to that measured by ground state recovery method described in chapter 3 was assumed to be the natural triplet lifetime.

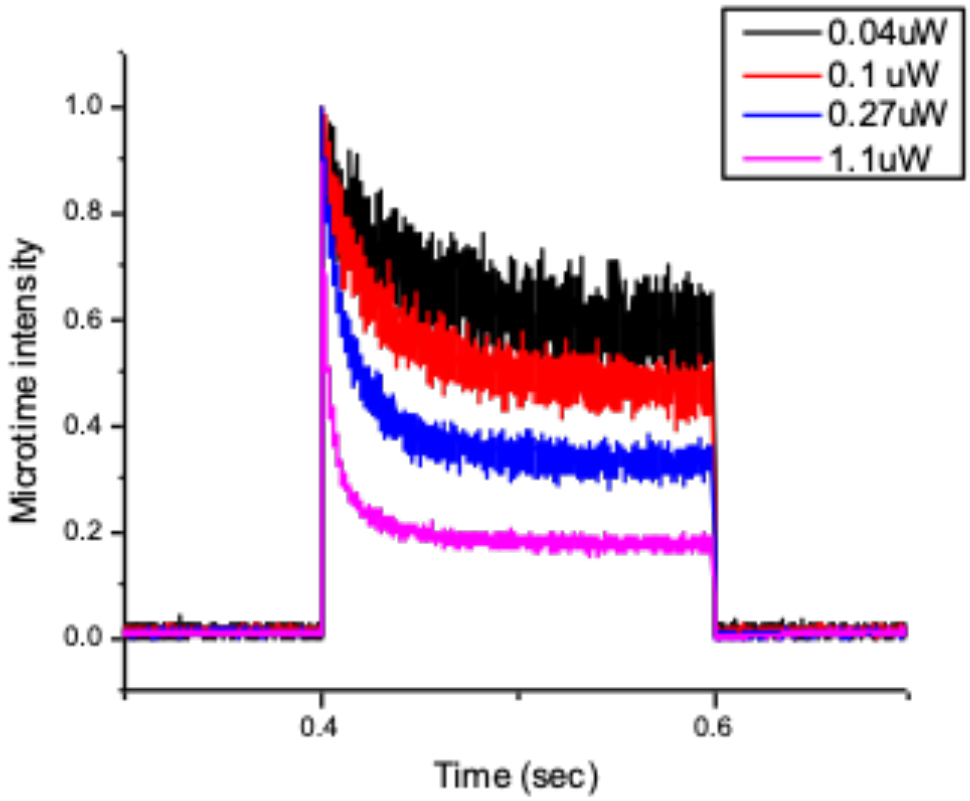

Figure 4-6 Fluorescence decay histogram of fluorescein under modulated 488nm excitation at varying intensities.

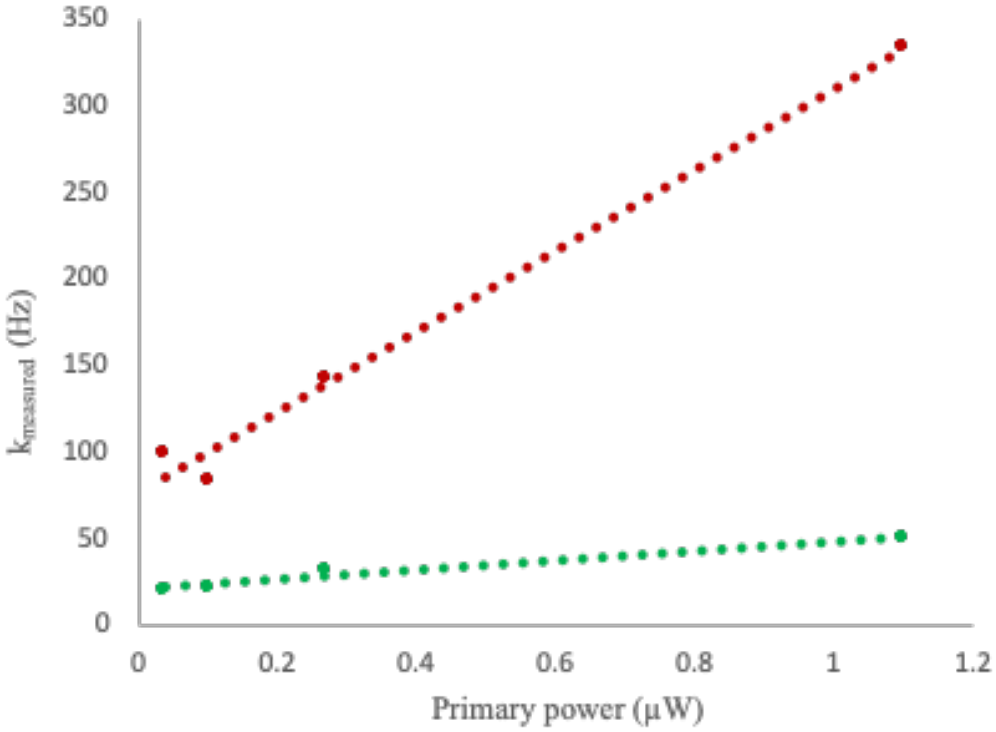

Figure 4-7 Plot of primary excitation power versus measured decay rate from the biexponential fit of fluorescein decay showing a linear relationship for both rates and an apparent convergence towards a single rate at lower excitation powers. The y-intercept gives the triplet lifetime (red) and photobleaching rate (green)

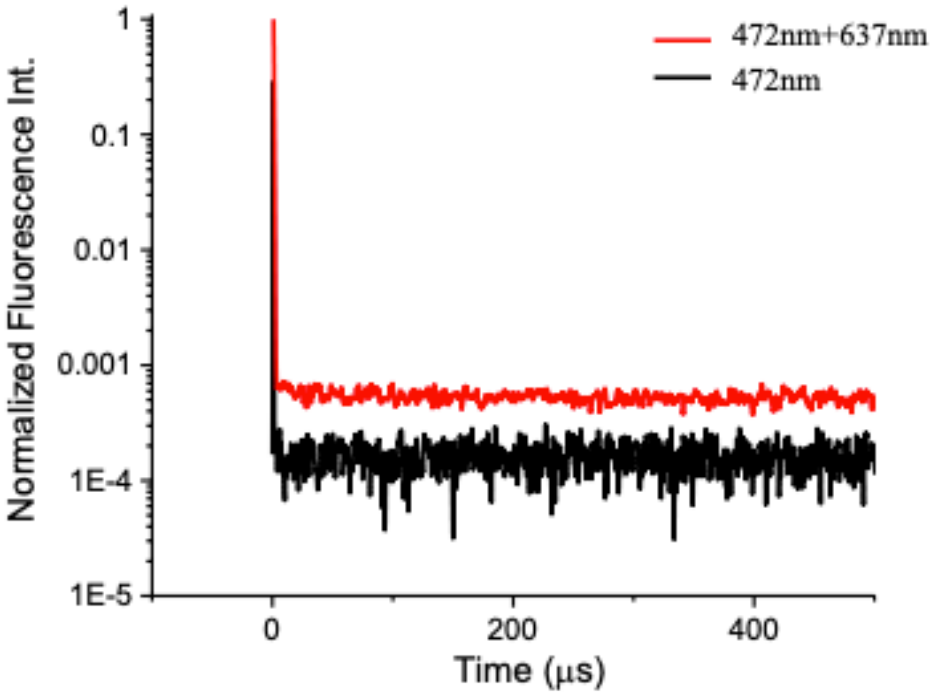

Figure 4-8 Fluorescence histogram showing OADF from fluorescein under pulsed primary (472nm) and CW secondary (637nm) excitation

As previously mentioned, triplet states are readily quenched by molecular oxygen, which hastens their non-radiative decay, and are therefore exceptionally environmentally dependent. By purging solutions with N_2 gas one can decrease O_2 content in the sample and extend triplet lifetime. Alternatively, immobilizing dyes in poly(vinyl alcohol) (PVA) films limits dye and oxygen mobility, largely eliminating oxygen-dye collision-based triplet decay. The effect of reduced oxygen interaction in the rose bengal is illustrated in Figure 4-9, showing a clear extension of the re-pumped fluorescence timescale when compared to RB in water. N_2 gas purging increase the dark state lifetime by a factor of 10, while PVA immobilization most dramatically extends the yield and timescale over which re-pumped fluorescence can be observed (up to >100 µs). Figure 4-9 shows the effect of

blowing continuous nitrogen on rose bengal solution. As seen in the figure the longer nitrogen is passed through the reaction chambers the longer the observed decay becomes.

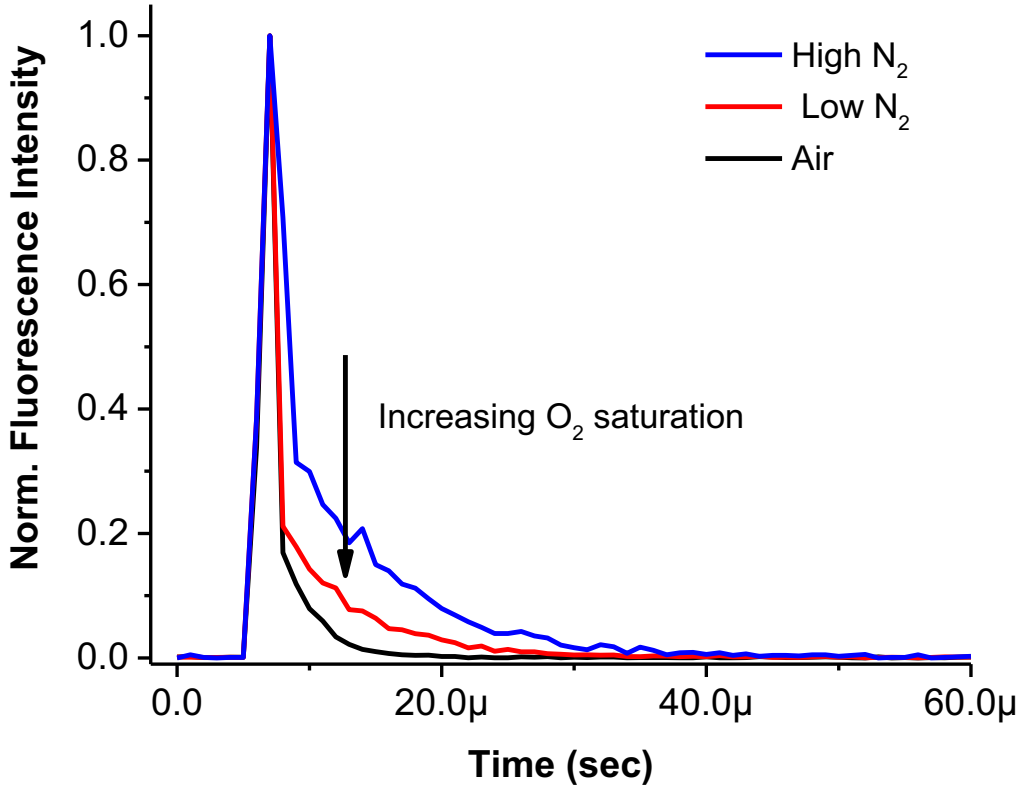

Figure 4-9 Fluorescence histogram of rose bengal solution under pulsed primary (10kHz) and CW secondary coillumination under varying levels of oxygen.

4.2.2 Pulsed-Pulsed

To characterize the additional fluorescence observed after primary-induced prompt fluorescence has decayed, we irradiated rose bengal with a pulsed 532nm and co-illuminated with an 830nm pulsed laser. Pulsed secondary excitation following an initial primary pulse shows that the delayed fluorescence (secondary induced) has similar decay characteristics to the prompt (primary induced) fluorescence observed. This further corroborates the additional signal observed as arising from the same state as observed

primary induced initial fluorescence. Contrary to what we have deduced in the case of pulsed primary co-illumination with the CW secondary laser, in this instance the upper limit of the OADF is given by the product of the triplet quantum yield and the reverse intersystem crossing quantum yield as each secondary pulsed gets one shot at depopulating the dark state. Therefore, even at high triplet quantum yields, such as what is observed in rose bengal systems, the relative OADF signal is a mere fraction of the prompt signal due to the low reverse intersystem crossing quantum yield. Decreasing the time between successive primary pulses can be used to increase the OADF contribution by increasing T_1 population through closely spaced successive excitation from the ground S_0 state. Figure 4-10 shows the increased pulsed-pulsed OADF intensity with increasing primary laser repetition rate. Similar experiments were carried out with erythrosin B and eosin Y.

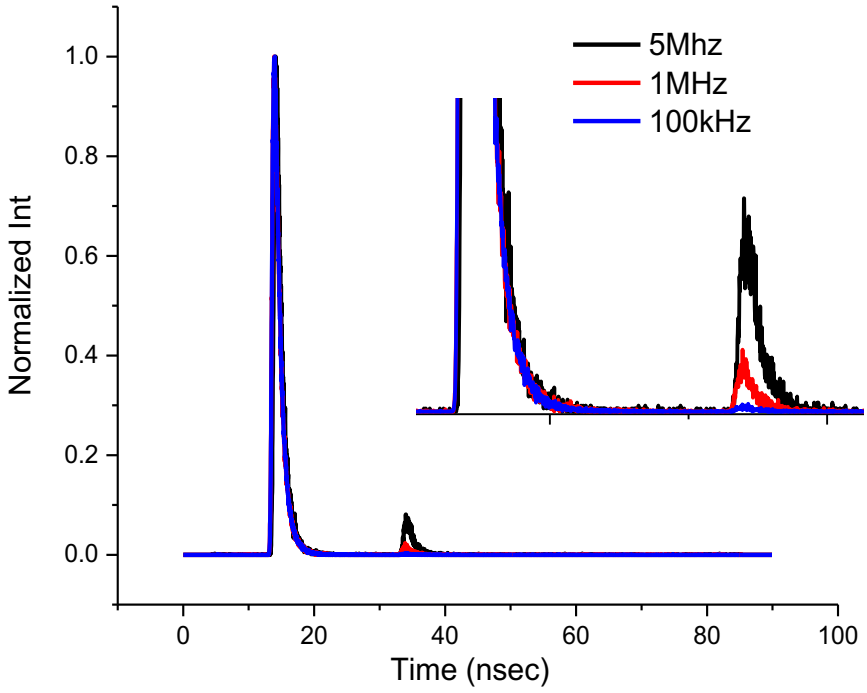

Figure 4-10 Fluorescence histogram of rose bengal in PVA with 532nm pulsed primary followed by 830nm pulsed secondary illumination. Inset shows the clear dependence of OADF on laser repetition rate.

4.3 Improved OADF Signals

Since the transition from dark state to excited singlet state is limited by the effective pulse width of the secondary laser, one can attain higher re-pumped fluorescence by having more secondary excitation cycles or using a CW laser to more thoroughly depopulate this state. By using bursts of CW excitation, we have shown that we can increase the observed OADF several-fold allowing for better detection over background. This approach paves the way for OADF to be used in existing confocal techniques.

Instead of giving multiple short pulses to increase T_1 population, use of a short burst of CW excitation as a (~1 μs) primary excitation pulse sufficiently enhances OADF, as continuous CW excitation generates many more excitations and a higher steady-state population in the triplet state. This is more obviously seen in the lower triplet quantum yield dye eosin Y than in rose bengal, as it can benefit from more excitations that shelve molecules in the triplet state. The ratio of integrated OADF to peak fluorescence (average intensity for burst excitation) in eosin Y increases from ~0.3 when using pulsed (100ps) excitation, to >10 when using long (50μs) primary excitation pulse widths coupled with CW (830nm) secondary OADF excitation.

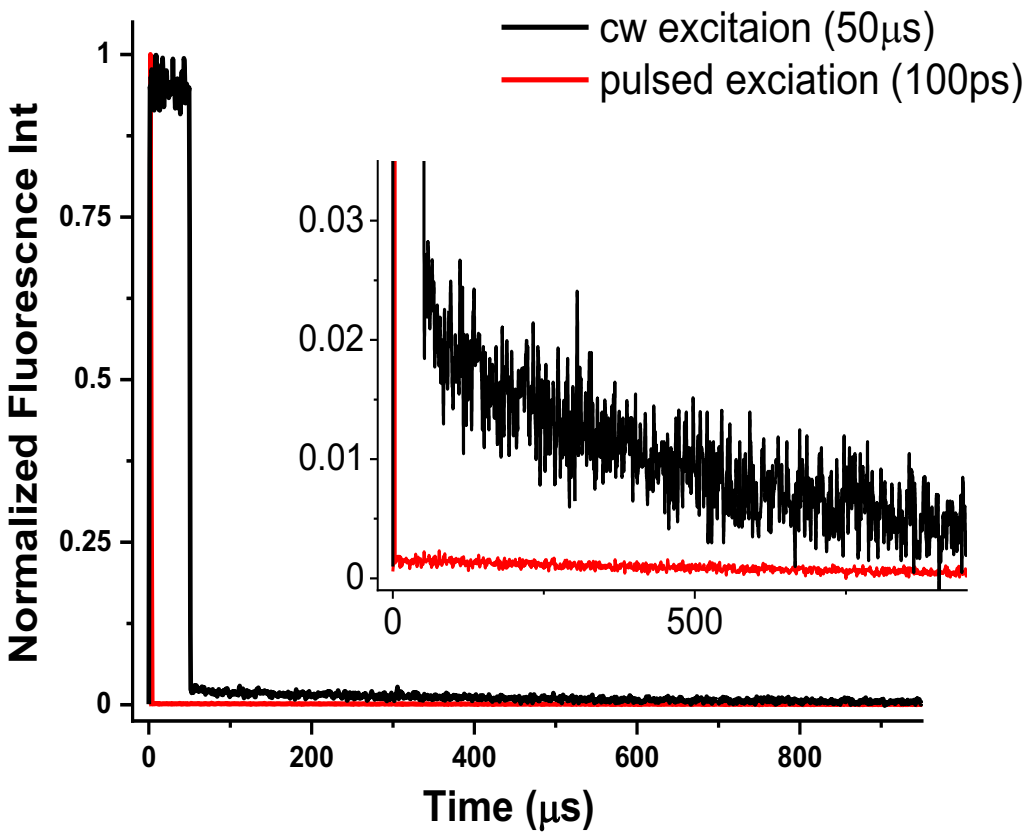

Figure 4-11 Fluorescence histogram of eosin y in PVA with pulsed 100ps excitation (red) CW 50μs pulsed width (black) primary excitation with simultaneous 830nm secondary illumination. Inset shows the clear increase of OADF in CW excitation over pulsed.

Additionally, using more excitation cycles of the S_0 to S_1 transition can lead to higher dark state buildup that can result in higher OADF photons upon secondary co-illumination and make even low triplet quantum yield dyes, with sufficiently long-lived transients, viable candidates for OADF applications. This is clearly seen in fluorescein where we used long excitation cycles (50μs), to observe OADF from its low quantum yield of << 1% triplet state and a lifetime of ~11ms. The ratio of total integrated OADF photons observed to average prompt fluorescence photons when using a 100μs pulse is 3.

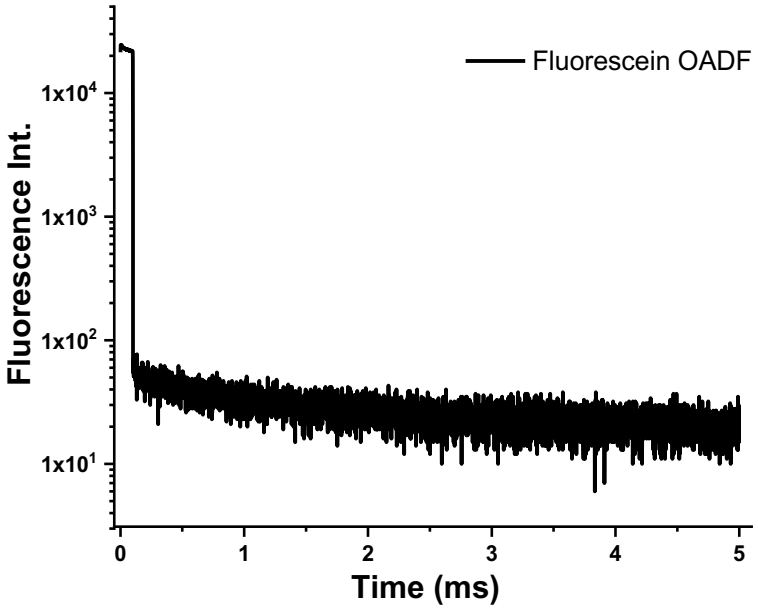

Figure 4-12 Fluorescence histogram of fluorescein in PVA under 50µs 488nm primary and 633nm CW secondary illumination exhibiting behavior characteristic of OADF.

As OADF results from the buildup of population in the triplet state, rose bengal shows the strongest OADF due to its high triplet quantum yield (~90%), followed by erythrosin B, eosin Y, and fluorescein. The lifetimes of these triplet states show the opposite trend with fluorescein having the longest-lived triplet state in PVA films.

4.4 Simulations of Xanthene OADF

The photophysics of these xanthenes was further modeled using a simple three state system represented in equation 7, consisting of a ground (S_0), first excited (S_1) and triplet (T_1) state. It should be noted that primary laser can also depopulate the triplet state, but that was not accounted for in this rate equations as the intensities were presumed to be very low to cause significant issues. Piecewise exponentiation of the rate matrix with experimental

and published rates and quantum yields for each state can be used to calculate the time dependent populations.

$$\frac{d}{dt}\begin{pmatrix} S_0 \\ S_1 \\ T_1 \end{pmatrix} = \begin{pmatrix} -I_{Pri}[t]\,\sigma_{S_0}\,\frac{\lambda}{hc} & k_f + k_{IC} & k_{T_1} \\ I_{Pri}[t]\,\sigma_{S_0}\,\frac{\lambda}{hc} & -(k_f + k_{ISC} + k_{IC}) & I_{sec}[t]\,\sigma_{T_1}\,\frac{\lambda}{hc}\,\Phi_{RISC} \\ 0 & k_{ISC} & -\left(k_{T_1} + I_{sec}[t]\,\sigma_{T_1}\,\frac{\lambda}{hc}\,\Phi_{RISC}\right) \end{pmatrix}\begin{pmatrix} S_0 \\ S_1 \\ T_1 \end{pmatrix}$$

Equation 7

The OADF generation for the xanthenes in PVA films was simulated with 532nm 100ps pulsed or continuous wave primary excitation and 830nm CW secondary excitations. Continuous wave burst excitation were used where appropriate with burst lasting 1μs for rose bengal and erythrosin B and 50μs for eosin Y as was done experimentally. The fluorescence lifetime in PVA was also measured using lifetime spectrometer (Edinburgh Instruments) and reconvolution fit gives a lifetime of ~1ns which was used in the simulations.

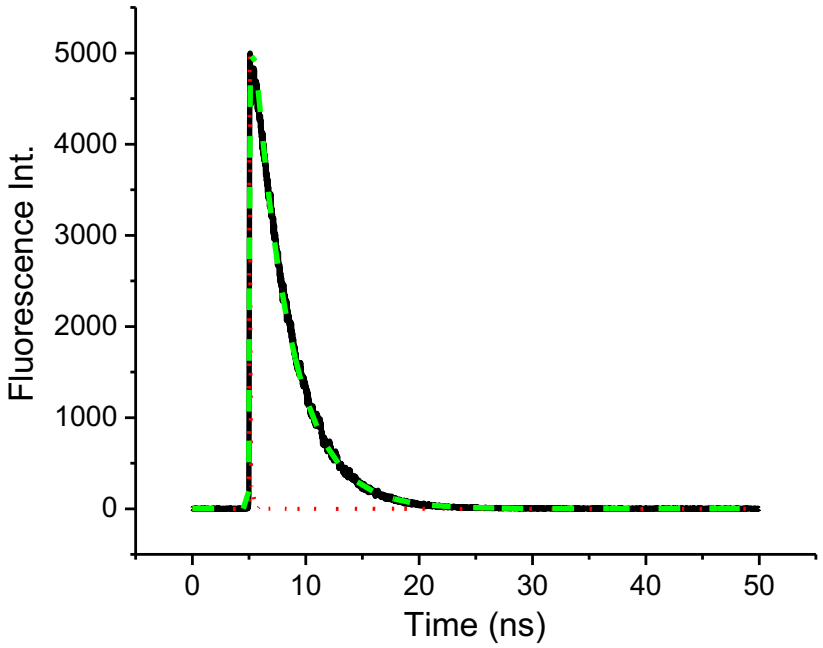

Figure 4-13 Fluorescence lifetime of xanthenes a reconvolution fit

The time-varying S_1 population is used as a surrogate for fluorescence intensity. The triplet lifetimes used for simulation are given in Table 4-1while all other relevant parameters are summarized below.

Table 4-2 Xanthene photophysical parameters used in simulations

	Rose bengal	***Erythrosin B***	***Eosin Y***
Triplet quantum yield ($\emptyset_T$)	93%	85%	45%
Reverse intersystem crossing quantum yield ($\emptyset_{risc}$)	1%	1%	1%

Simulated OADF: integrated prompt fluorescence ratios are similar to experimental results with integrated OADF intensity to prompt fluorescence ratios for pulsed cw

excitation giving 0.4, 0.8, 0.9 for eosin Y, erythrosin B and rose bengal, all lower than the triplet quantum yields used in simulations (Table 4-2). The results of simulation are given in Table 4-3 where burst integrated represents the ratio of the total OADF photons to the integrated prompt fluorescence while burst average is the ratio of the total OADF to the average photon intensity in the excitation period in the case of a cw burst excitation (1μs for rose bengal and erythrosin B and 50μs for eosin Y). The results underscore the ability of excitation period to dramatically affect the OADF capabilities of fluorophores. This increase in OADF ratio with longer primary excitation cycles is reproduced via simulation as shown in Figure 4-14 for eosin Y.

Table 4-3 Ratio of OADF photons to prompt fluorescence in simulated scenarios as well as experimental

	Pulsed-cw		**Burst integrated**		**Burst average**		**OADF fraction of enhancement**	
	exp	**sim**	**exp**	**sim**	**exp**	**sim**	**P-cw**	**burst-cw**
RB	1.1 ± 0.3	0.87	0.95 ± 0.03	0.77	2.04 ± 0.29	1.53	100%	94%
EB	0.83 ± 0.06	0.79	1.07 ± 0.1	0.7	2.02 ± 0.06	1.4	100%	88%
EY	0.24 ± 0.06	0.34	0.21 ± 0.03	0.24	20 ± 5	12	100%	48%

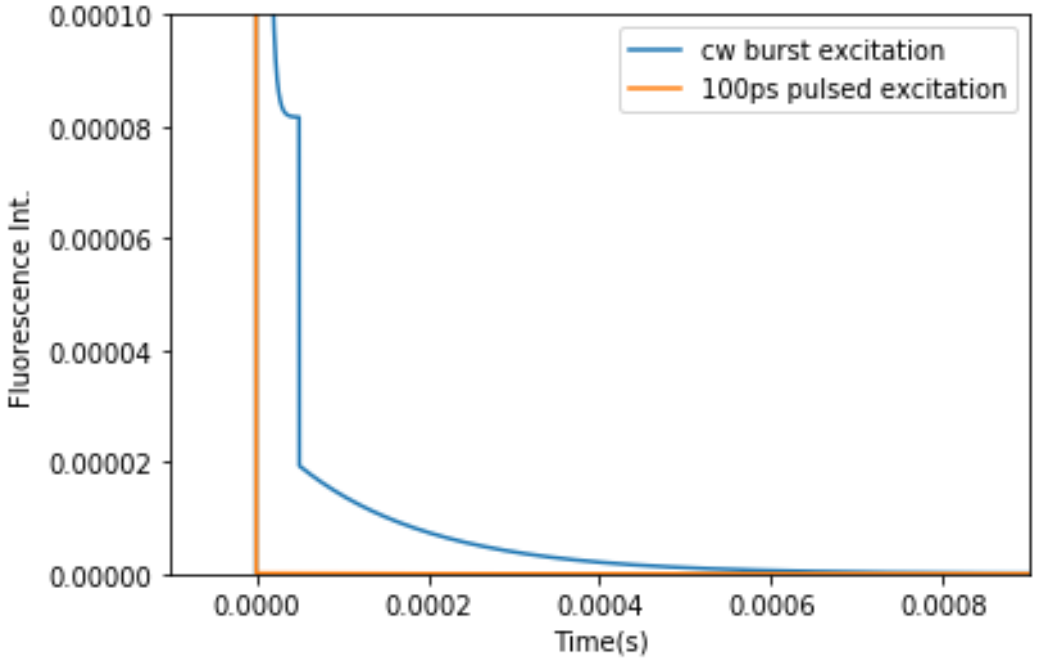

Figure 4-14 Fluorescence histogram of simulated eosin Y fluorescence under pulsed excitation (orange) and burst excitation (50µs) showing an increase in OADF with longer excitation cycles.

The results also show that the enhancement previously reported under pulsed primary excitation[14] was primarily through OADF and not by directly populating the ground state as previously thought. While the OADF contribution to enhancement for the xanthenes was determined to be ~100% under pulsed primary, longer burst cw excitation periods show an OADF contribution of 94% for rose bengal, 88% for erythrosin B and 48% for eosin Y

4.5 Conclusion

OADF results from the direct transition of fluorophore molecules between and triplet and singlet excited states using lower energy secondary excitation. Primary excitation leads

to population buildup in a long-lived dark state, which decays back to the singlet ground state on some characteristic time scale. However, upon secondary illumination of the dark state, the population is re-pumped to the excited singlet manifold and gives rise to additional fluorescence at delayed times. This secondary laser-induced OADF decays exponentially between each primary pulse and is directly proportional to the intensity of the secondary excitation.

By using pulsed primary excitation, we create periods where there is no primary excitation, and thus any photon generated as a result of secondary laser excitation between each period after the initial prompt fluorescence has completely decayed represents a sequential "2-photon" process in which the secondary induced photons are effectively free of additional background. This pulsed excitation is in contrast to our previously described CW-CW modulation scheme of these dyes,[14] where we probed the ground state process in addition to possible OADF from reversible excited states. Pulsed excitation allows us to emphasize the OADF over any ground-state processes allowing us to determine its contribution to overall enhancement. Our results underscore the fact that for the studied xanthenes, OADF offers the most optimal route to enhancement via optical modulation in lieu of directly populating the singlet ground state, which would lead to an increased peak fluorescence upon secondary co-illumination.

Since the transition from dark state to excited singlet state is limited by the effective pulse width of the secondary laser, one can attain higher re-pumped fluorescence by having more secondary excitation cycles or using a CW laser to more thoroughly depopulate this state. By using bursts of CW excitation, we have shown that we can increase the observed

OADF several fold allowing for better detection over background. This paves the way for OADF to be used in existing confocal techniques.

CHAPTER 5. PHOTOISOMER VS. TRIPLET MODULAITON IN MEROCYANINE 540[1]

5.1 Introduction

Cyanine dyes are characterized by polymethine chains of varying lengths. Symmetric cyanines exhibit particle-in-a-box-like states,[72-74] while merocyanines display asymmetric push-pull excited state characteristics.[75-76] Previous experimental and theoretical studies[45, 77-78] have demonstrated that cyanines readily photoisomerize to produce the ground state cis-isomer that is ~0.1 eV higher in energy than the all-trans ground state. Generally, the significant barriers to reverse isomerization cause these dark states to have lifetimes ranging from ~μs to seconds, and can yield relatively high dark state populations under steady-state excitation.[45, 74, 78-79] In addition to isomerization, the cis and trans states of these dyes can undergo intersystem crossing from the all-trans or cis excited state to yield the all-trans or cis triplet. The resulting triplet lifetimes are typically <10μs, especially in the presence of oxygen.[80-81]

[1] This chapter was adapted from previously published work and reproduced with permission from authors. Mahoney, D. P.; Demissie, A. A.; Dickson, R. M., Optically Activated Delayed Fluorescence through Control of Cyanine Dye Photophysics. *The Journal of Physical Chemistry A* **2019,** *123* (16), 3599-3606.

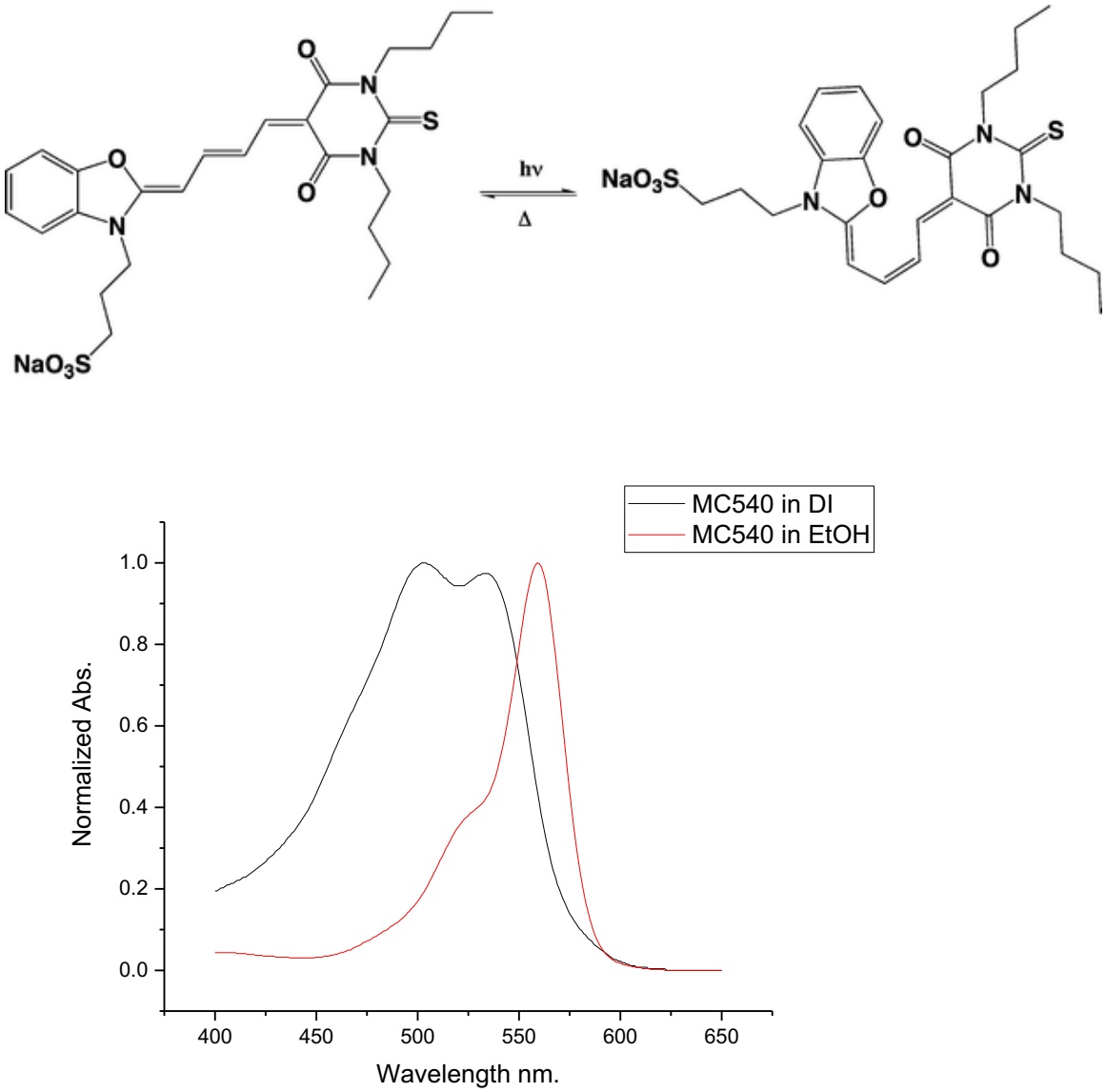

Figure 5-1 A) Photoisomerization in merocyanine 540 B) UV-vis absorption of merocyanine 540 in different media

Direct excitation of any dark state population has the potential to optically regenerate the ground state of the emissive manifold faster than would occur thermally.[10-11, 14] Our lab has previously shown that fluorescence from Cy5 and merocyanine 540 can be modulatable by optically depopulating the ~100 µs-lived cis-photoisomer states.[10, 45] Photoisomerization, however, results in a structural change with poor Franck-Condon

overlap of the cis-photoisomer ground state with that of the emissive trans excited state. Therefore, secondary co-illumination does not generate emission upon photoisomerization, and modulating the secondary light source can only directly modulate collected fluorescence by dynamically altering the all-trans ground state population, which itself is continuously excited by primary laser co-illumination. Transient absorption studies of these dyes have shown the presence of trans triplet states in both cyanines. Such states for Cy5 are blue shifted relative to the all-trans ground state absorption, while the merocyanine 540 triplet is red shifted from its ground state absorption and allow for the possibility of this trans triplet to under-go long wavelength modulation. Therefore, modulation observed in the case of merocyanine 540 has contributions from both isomerization and the intersystem crossing processes.

Molecules with small energy singlet-triplet differences allow thermally activated $S_1 \leftrightarrow T_1$ transitions that can result in delayed fluorescence, as T_1 population trickles back into the fluorescent S_1 state. In some cyanines, optical excitation generates a photo-reversible photoisomer that enables fluorescence modulation through long-wavelength co-illumination.[45, 77, 82] While shorter-lived triplet states are also produced, cyanines typically exhibit singlet-triplet gaps that are too large to facilitate TADF, so only prompt, ns-lived emission is observed. Unlike the photoisomer states, however, cyanine triplets are both electronically excited and likely to retain strong Franck-Condon overlap with the emissive excited singlet states. While both photoisomer and triplet dark states may be excitable with long wavelength secondary co-excitation, absorption by the higher energy triplet state offers the potential for low energy secondary illumination to re-pump the emissive singlet state through reverse intersystem crossing. Although optical modulation in cyanines has been largely described as resulting from optically shifting population from the dark state

back to the ground state of the fluorescent manifold,[10, 45] re-pumping of the emissive S_1 state to generate ns-lived fluorescence at much longer delays would offer an additional contribution to the total enhanced fluorescence. This OADF promises selective detection and background-free detection.

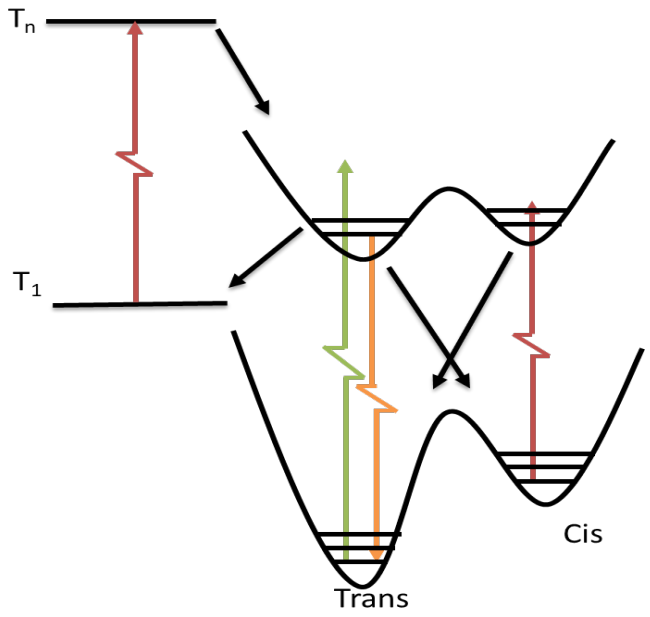

Figure 5-2 Jablonski diagram illustrating fluorescence recovery pathways via dark state recovery. Secondary excitation of the dark (cis) photoisomer regenerates the all-trans ground state of the fluorescent manifold. In contrast, secondary excitation of the all-trans triplet can regenerate the excited state of the fluorescent manifold through reverse intersystem crossing, resulting in Optically Activated Delayed Fluorescence (OADF).

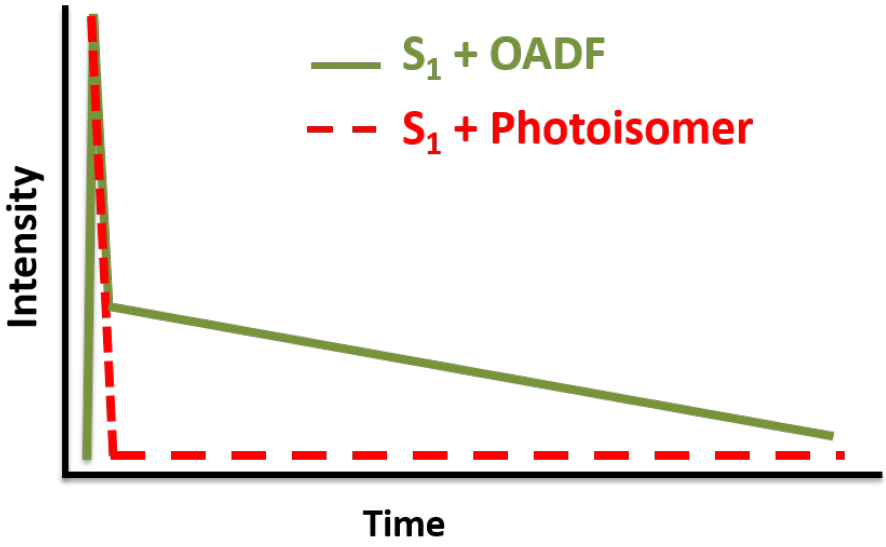

Figure 5-3 Schematic representation of a fluorescence histogram of the differences observed between modulation of a photoisomer (red) and a triplet that with OADF properties.

In addition to the known photoisomerization pathway described in earlier modulation schemes, optical excitation of merocyanine 540 can also generate ~μs-lived triplet states through intersystem crossing. Unlike photoisomerization, however, this triplet level is an electronically excited dark state that should retain strong Franck-Condon overlap with the S_1 level, enabling optically induced reverse intersystem crossing to generate additional fluorescence by avoiding a (non-fluorescent) cis-trans back-isomerization. Previous investigations of merocyanine 540 have determined the triplet absorption to be around ~600-650nm (overlapping with the photoisomer), with a ~1 μs lifetime.[83-86] Consequently, this chapter uses both CW and pulsed excitation to investigate the dark state photophysics of merocyanine 540 and distinguish modulation paths in merocyanine 540 by identifying OADF contributions to measured enhancements.

5.2 Dark-state Photophysics of Merocyanine 540

5.2.1 CW excitation

When probing merocyanine 540 with CW-CW excitation schemes, modulation resulting from the triplet state is indistinguishable from that of the photoisomer. Upon absorption of the primary laser, optically modulatable fluorophores such as merocyanine 540 transition to a thermally meta-stable dark state before relaxing back to regenerate the ground state. In the fluorescence signal, this is marked by an initial increase in prompt fluorescence followed by a decrease in the fluorescence signal to reach steady state that is dependent on excitation intensity. By quickly turning off the primary excitation, the buildup of population in the dark-states thermally recovers back to the emissive manifold. Because co-illumination with secondary long wavelength excitation causes optical depopulation of these dark-states we can eliminate the decay observed from square wave modulated primary excitation only.

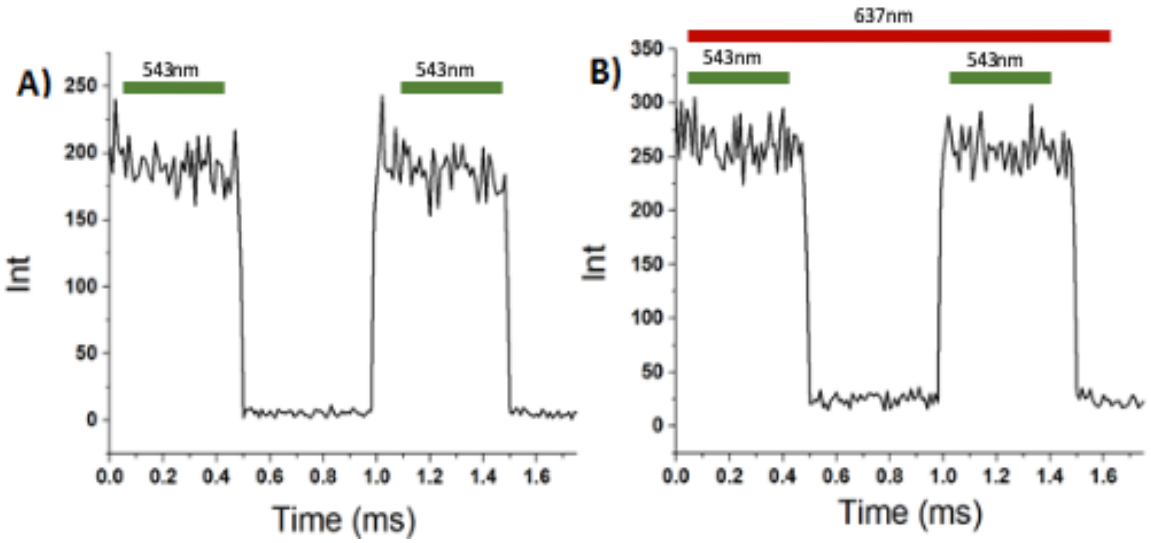

Figure 5-4 Fluorescence histogram of merocyanine 540 in water. A) Modulated CW primary excitation (543nm, 600 W/cm^2), B) modulated

primary plus constant (CW) secondary co-illumination (637nm, 10 kW/cm^2), showing elimination of fluorescence decay due to lack of dark state build up.

Alternatively, if the secondary illumination is performed in between successive primary only excitation periods, an increase in the initial prompt fluorescence is observed. This observation is due to the secondary laser optically depopulating the dark-state in favor of the fluorescence generating state.[87] Increasing the time between successive primary excitation periods without the use of secondary excitation can also accomplish, unless there are sufficient thermal populations in the higher lying dark-states.

5.2.2 Pulsed excitation

Modulation of merocyanine 540 was also investigated using a pulsed 532nm primary laser. Under pulsed primary excitation (pulse width 100ps), prompt ps and ns fluorescence is observed in solution and immobilized samples, respectively. Secondary co-illumination with previously used 637nm results in additional 580nm fluorescence, both within the initial prompt fluorescence and between primary laser pulses with the delayed 580nm fluorescence signal persisting past the decay of the initial prompt signal. This delayed signal represents the optically activated delayed fluorescence from merocyanine, and since OADF cannot arise from the photoisomer, it can provide a means of characterizing the triplet state dynamics of merocyanine 540.

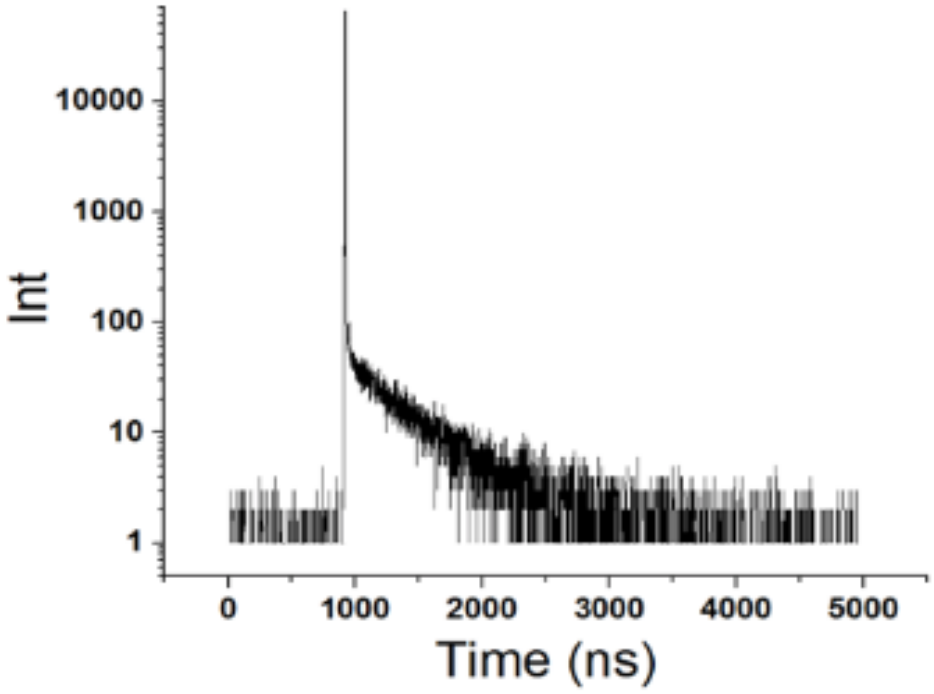

Figure 5-5 Fluorescence histogram of merocyanine 540 in aqueous solution using 532nm pulsed excitation (rep rate 10 kHz) with 637nm CW co-illumination showing an OADF tail persisting past 2µs.

The increase seen in the prompt fluorescence pulse arises from optical recovery of the ground S_0 state from both the photoisomer and from the triplet. This observation is due to the much longer-lived nature of the isomer,[86] though it is mostly dominated by the isomer. The longer-lived ~580nm fluorescence decay between primary pulses, with similar decay times as the prompt fluorescence, however, is OADF generated from exciting the triplet state with 637nm that is depopulated by cycling through the emissive S_1 level. Similar to the xanthenes, increasing the secondary intensity accelerates the decay of this delayed component. By plotting secondary intensity versus measured decay rate, we can determine the natural lifetime of the triplet state, according to Equation 5 which is given as the inverse of k_{off}^0. The triplet lifetime of merocyanine 540 in water was determined to be

~1µs, consistent with previously reported values.[86] Pulsed primary and pulsed secondary excitations also show that the additional fluorescence generated by the secondary laser has a decay constant similar to that of the triplet lifetime.

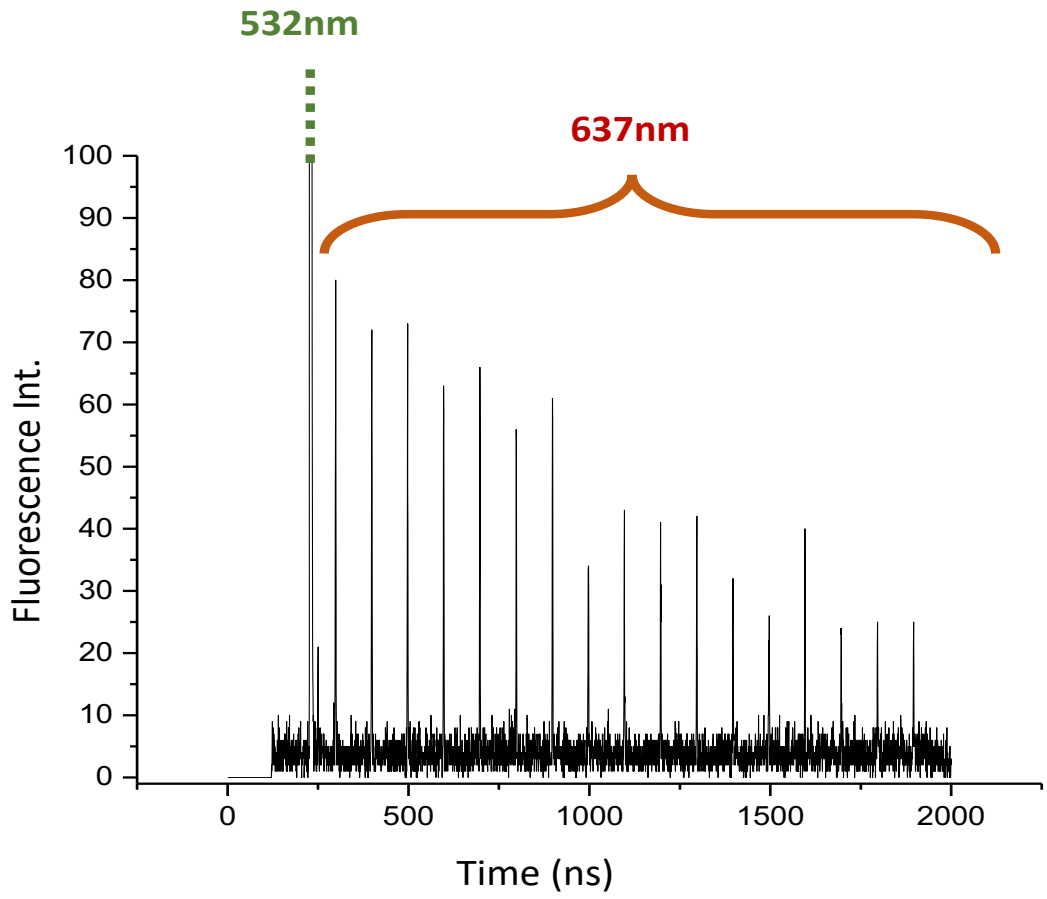

Figure 5-6 Fluorescence histogram of MC540 in water under pulsed 532nm primary (500kHz) and pulsed 637nm secondary excitation (10Mhz)

To further corroborate that the timescales observed in OADF are due to the triplet state we investigated merocyanine 540 photophysics in deoxygenated environments. Triplet state lifetimes typically decrease when oxygen is present, as triplet-induced singlet oxygen formation rapidly regenerates the singlet state of the dye. Similarly, immobilizing

dyes in poly(vinyl alcohol) (PVA) films limits dye and oxygen mobility, largely eliminating oxygen-dye collision-based triplet decay, and increasing barriers to isomerization. When purging merocyanine 540 solutions with nitrogen gas an increase in the measured OADF decay timescale was observed giving a triplet time scale ~15μs. An even greater increase in triplet timescales was observed upon PVA immobilization of merocyanine 540 with triplet timescales measured to be ~45 μs (Table 1). With these extended dark state lifetimes, the OADF contribution to the overall enhancement should rise in PVA compared to solution. The decay of the observed OADF was also measured using pulsed primary and pulsed secondary, giving a fluorescence lifetime of 1.7ns for both prompt and secondary induced OADF, as shown in Figure 5-8.

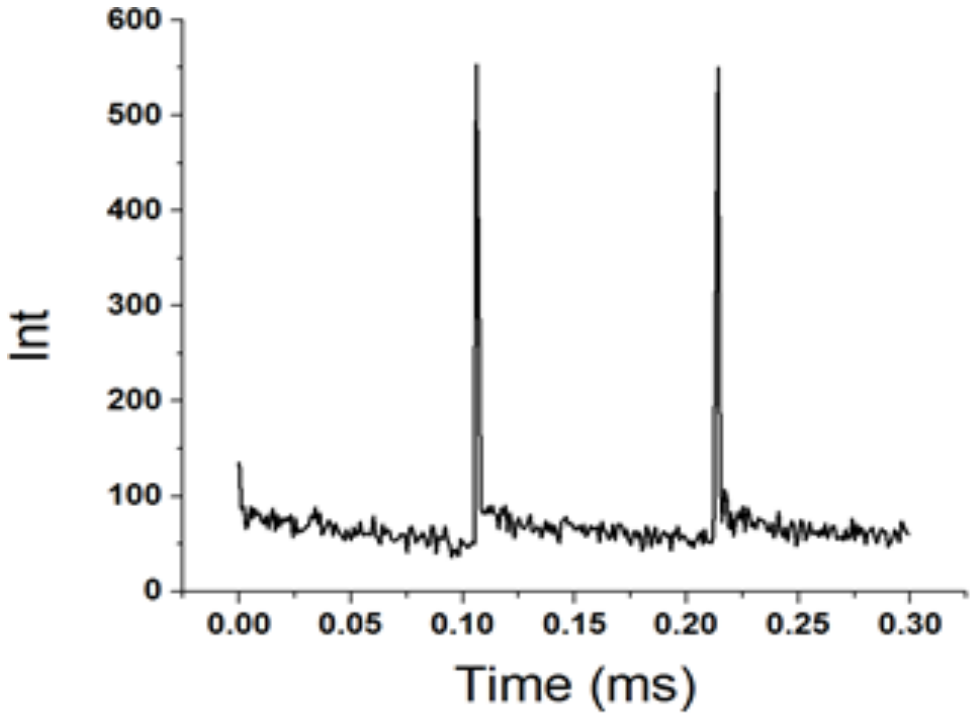

Figure 5-7 Fluorescence histogram of merocyanine 540 in PVA films under Pulsed primary and CW secondary excitation.

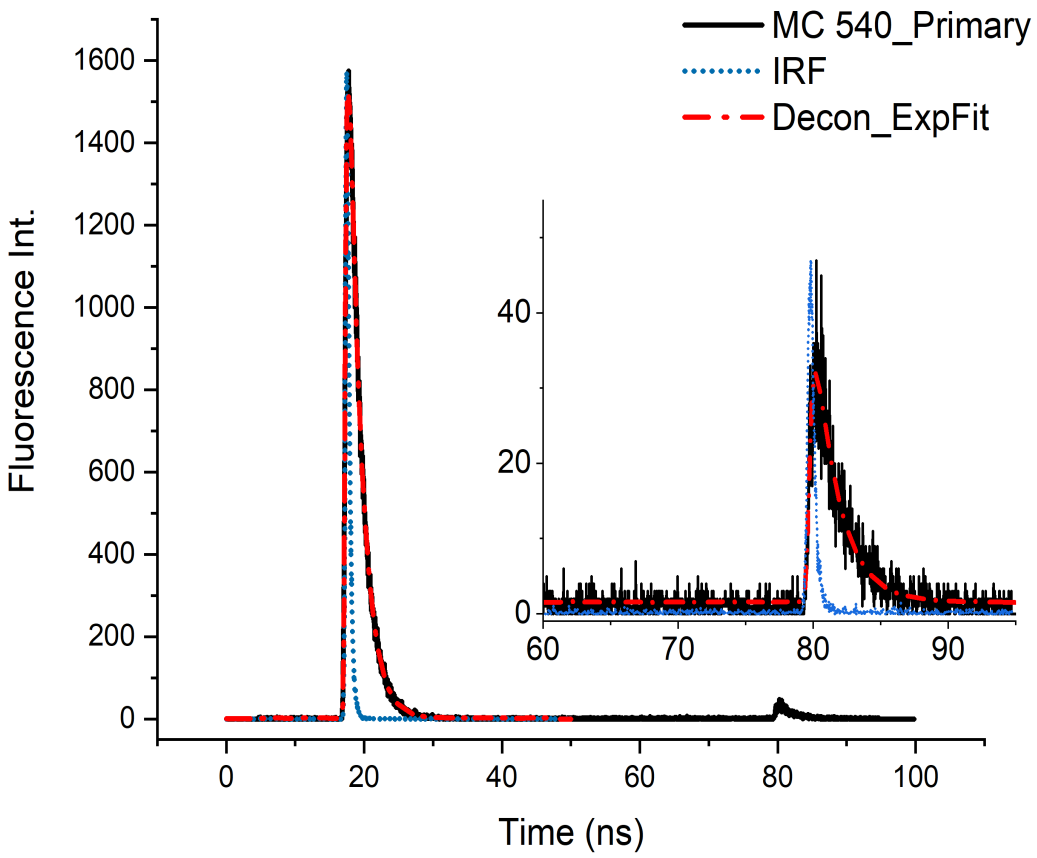

Figure 5-8 Fluorescence lifetime of Merocyanine 540 in PVA film using 532nm pulsed primary and 637nm pulsed secondary excitation. Inset showing the similar nano second decay nature of the OADF signal. A single exponential fit gives a lifetime of approximately 1.7ns for both prompt fluorescence and OADF

Table 5-1 Measured photophysical timescales of merocyanine 540

Fluorescence lifetime in water (k_f^{-1})	200 ps
Fluorescence lifetime in PVA (k_f^{-1})	1.7 ns
Triplet lifetime in water ($k_{T_1}^{-1}$)	1.18±0.18 µs
Triplet lifetime in water, N_2 purging ($k_{T_1}^{-1}$)	16.1±0.5 µs
Triplet lifetime in PVA ($k_{T_1}^{-1}$)	45.5±7.3 µs

5.3 OADF Properties

In order to figure out the OADF contribution to overall fluorescence in merocyanine 540, we measured the integrated primary induced fluorescence and the integrated secondary induced OADF tail. The total count rate of the detector during measurements was kept within a fraction of the repetition rate of the laser to ensure that the prompt peak was not saturated. By comparing the integrated secondary induced fluorescence to primary-induced fluorescence, OADF accounts for ~7% of the total fluorescence in PVA and 1% in water.

We measured the enhancements of merocyanine in PVA immobilized samples under pulsed primary CW secondary excitation to be ~50%**,** with OADF contributing 20% of the overall enhancement relative to enhancement of the prompt fluorescence in PVA immobilized samples. This ratio is the fraction of OADF (delayed) photons to the total

enhancement, or the relative contribution of T_1 to S_1 re-pumping relative to reverse isomerization induced by long-wavelength co-illumination.

5.3.1 Photophysical Simulations of merocyanine 540

Merocyanine 540 photophysics was simulated using a four-state system given by Equation 7, consisting of ground (S_0) and excited (S_1) singlet states and two dark states - one triplet state (T_1) and a ground cis isomer state (Cis_{s0}). Each of the two dark states can be optically depopulated at long wavelengths to regenerate the excited and ground singlet states, respectively. Experimentally determined quantum yields and extinction coefficients from all states[45, 85-86, 88-92] were combined with experimental excitation intensities and, where relevant, pulse widths. Fluorescence intensity is taken as the time-dependent S_1 excited state population. Time-dependent populations are calculated by piecewise exponentiation of the four-level rate matrix.

$$\frac{d}{dt}\begin{pmatrix} S_0 \\ S_1 \\ T_1 \\ CisS_0 \end{pmatrix} = \begin{pmatrix} -I_{Pri}[t]\,\sigma_{S_0}\frac{\lambda}{hc} & k_f & k_{T_1} & \left(k_{RISO} + I_{Sec}[t]\,\sigma_{ISO}\frac{\lambda}{hc}\Phi_{RISO}\right) \\ I_{Pri}[t]\,\sigma_{S_0}\frac{\lambda}{hc} & -(k_f + k_{ISC} + k_{ISO} + k_{IC}) & I_{Sec}[t]\,\sigma_{T_1}\frac{\lambda}{hc}\Phi_{RISC} & 0 \\ 0 & k_{ISC} & -\left(k_{T_1} + I_{Sec}[t]\,\sigma_{T_1}\frac{\lambda}{hc}\Phi_{RISC}\right) & 0 \\ 0 & k_{ISO} & 0 & -\left(k_{RISO} + I_{Sec}[t]\,\sigma_{ISO}\frac{\lambda}{hc}\Phi_{RISO}\right) \end{pmatrix} \begin{pmatrix} S_0 \\ S_1 \\ T_1 \\ CisS_0 \end{pmatrix}$$

Equation 8

Simulations using experimental intensities, rate constants, forward and reverse quantum yields, and absorption cross sections yield CW-CW enhancements of ~75%, pulsed-CW enhancements of 50%**,** with OADF contributing 20% of the overall enhancement relative to enhancement of the prompt fluorescence in PVA immobilized samples. This ratio is the fraction of OADF (delayed) photons to the total enhancement, or the relative contribution of T_1 to S_1 re-pumping relative to reverse isomerization induced

by long-wavelength co-illumination. The excellent match between experiment and simulation using literature and experimentally relevant parameters enables us to determine the relative contribution of OADF to the overall fluorescence enhancement. In the case of zero oxygen-induced decay and a short primary pulse width, relative to the MC540 fluorescence lifetime, the maximum ratio of integrated OADF signal to prompt fluorescence should be no greater than the triplet quantum yield (9 %)[85], as molecules can be excited no more than once for each primary laser pulse.

Table 5-2 Photophysical parameters used for simulation

Fluorescence lifetime* ($\boxed{k_f^{-1}}$)	1.7 ns (PVA)
Triplet lifetime* ($\boxed{k_{T_1}^{-1}}$)	45 µsec
Isomerization lifetime[86] ($\boxed{k_{Iso}^{-1}}$)	6.5 ms
Fluorescence quantum yield (Φ_F)	0.27
Triplet quantum yield[85] (Φ_T)	0.09
Isomerization quantum yield (Φ_{iso})	0.1
Reverse intersystem crossing quantum yield[83] ($\boxed{\Phi_{RISC}}$)	0.75
Reverse isomerization quantum yield ($\boxed{\Phi_{RISO}}$)	0.0015

Singlet absorption cross section (σ_{S_0})	4.9 x 10^{-16} cm^2
Triplet absorption cross section (σ_{T_1})	5.7 x 10^{-18} cm^2
Isomer absorption cross section (σ_{ISO})	4.9 x 10^{-18} cm^2

Pulsed primary (532nm, as above) and pulsed secondary excitation (647nm, ~100 ps pulse width) was also used to demonstrate that the secondary laser excites ns-lived fluorescence by repopulating the S_1 level from a long-lived dark state. In this experimental configuration, prompt (532nm-excited) fluorescence still results from primary excitation, but OADF results from pulsed secondary excitation at 647nm, delayed in time from the primary 532nm excitation. The secondary induced fluorescence peak is only present if the primary laser has prepared the triplet state. OADF generates similar 1.7ns-lived, ~580nm fluorescence that decays with dark state population, consistent with the pulsed-CW data. At a lower energy than the collected fluorescence, secondary 647nm illumination produces no fluorescence without a preceding primary excitation. Due to a large reverse intersystem crossing rate (0.74),[89, 91] the integrated intensity of OADF from each secondary pulse can reach up to one percent of that from the prompt fluorescence peak. In the most idealized scenario this ratio is given by the product of ISC (0.09)[85] and RISC (0.74)[89, 91] quantum yields. Simulations have reproduced the pulsed-pulsed, pulsed-cw OADF signals seen in experiments (Figure 5-9).

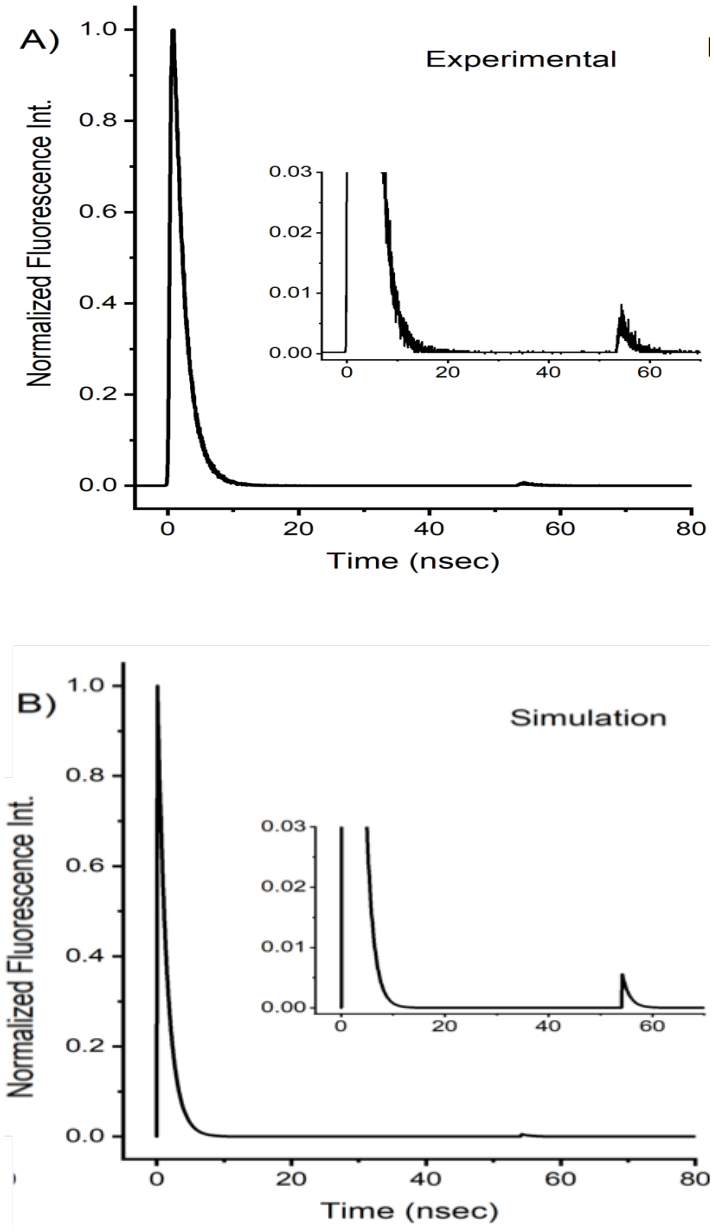

Figure 5-9 Fluorescence decay histograms showing A) experimental and B) simulated results of merocyanine 540 in PVA under consecutive 532nm and 647nm pulsed illumination.

In merocyanine 540, optical modulation can result from both photoisomerization and intersystem crossing but with very different outcomes. If the depopulated dark-state is a photoisomer, then the process is non-radiative as the energy is readily lost through

conformational changes between cis and trans configurations, and no emission is observed as there is poor overlap between the Franck-Condon states of cis and trans isomers. Triplet states, however, are able to reverse intersystem cross back to the singlet emissive manifold to generate additional delayed fluorescence. Pulsed primary excitation is crucial for distinguishing these mechanisms and elucidating the photophysical contributions of OADF to optical modulation. Adjusting experimental conditions to limit interaction with oxygen result in increased triplet populations and higher OADF. This, in combination with the correspondence of OADF/prompt fluorescence ratio to the triplet yield, suggest that MC540 delayed, ns-lived OADF results from long-wavelength optical excitation and RISC from the previously prepared triplet state, observed at much longer times after the prompt, primary-induced emission decays away. Forward and reverse photoisomerization gives rise to modulation on much longer timescales due to the longer (~6.5ms) dark state lifetime,[86, 91-92] but without OADF.

5.4 Conclusion

Long-wavelength optical recovery has been reported for both merocyanine 540 and Cy5. However, in merocyanine 540 the ns-lived fluorescence emission can be re-pumped by exciting the long-lived triplet with a red shifted secondary laser, many microseconds after primary laser excitation has been turned off. In merocyanine 540 the appearance of re-pumped emission between primary laser pulses opens the possibility of designing organic OADF capable fluorophores for applications in background-free signal recovery. The advantage in OADF capable fluorophores lies in its ability to drastically extend the timescales over which fluorescence can be observed.

Whether from a triplet or other excited dark state, the ability to tune excited dark state lifetime as well as the longer wavelength fluorescence re-pumping should open new avenues in background-free optical detection. Merocyanine 540's unique photophysics with both photoisomer and triplet dark states having absorptions that are red-shifted relative to its fluorescence allow examination of these different states. CW-CW and pulsed-CW excitation schemes demonstrate that merocyanine 540 is capable of both ground and excited state recovery. This first organic OADF emitter is not only a common fluorophore in biological labeling,[93-94] but also provides a roadmap for creating other molecules capable of OADF by using dark state lifetime and re-pumped fluorescence as an additional dimension in fluorescence detection.

CHAPTER 6. SYNCHRONOUSLY AMPLIFIED PHOTOACOUSTIC IMAGE RECOVERY (SAPHIRE)

6.1 Introduction

There is a great need for the development of imaging and detection technologies that can diagnose small, early stage pathologies deep within tissue. While a range of medical imaging modalities hold promise, none are perfect and many suffer from issues regarding sensitivity, resolution, complexity/expense, or ionizing radiation[51]. Optical imaging and fluorescent labeling, in particular, have revolutionized cell biology research, but direct imaging in deep tissue is limited by the high optical scattering for both excitation and emission[95-96]. Conversely, less sensitive approaches, such as ultrasound, offer excellent penetration, but poor contrast that relies on differences in mechanical properties within tissues. Combining optical excitation and acoustic detection, photoacoustic (PA) imaging is particularly promising as optically generated acoustic waves are less susceptible to scattering and readily detected with ultrasonic transducers.[50, 97-100] Many endogenous agents, such as blood, produce strong photoacoustic signals and enable natural contrast for imaging vasculature. However, these and other natural absorbers simultaneously limit deep tissue and small pathology imaging, especially in the presence of blood.

PA signals result from impulse optical excitation of strongly absorbing species that undergo efficient non-radiative decay[50, 101]. Such rapid deposition of energy in the surrounding tissue generates an acoustic signal that can be detected with ultrasonic transducer arrays and used to reconstruct images of optical contrast agent location. While strongly absorbing dyes such as methylene blue and indocyanine green have been used to

label and recover PA signals from sentinel lymph nodes[102-104], very high dye concentrations must be targetable to the pathology of interest and multispectral or other approaches used to visualize signals in the presence of high background in-vivo. To circumvent the need for high dye concentrations, non-degradable, noble-metal nanoparticles and carbon nanotubes have been explored as PA contrast agents[98, 105-111]. For use of high concentration dyes or non-clearable nanoparticles as contrast agents, both acute and long-term toxicity concerns need to be addressed[112-114]. Although strong signals are always beneficial, background suppression can even more drastically improve sensitivity to smaller and deeper pathologies. This chapter builds on previous modulation results in fluorescence imaging and investigates applicability in photoacoustic background suppression.

6.2 Photoacoustic Modulation

As described in previous chapters, optical modulation has been effective in suppressing background via Synchronously Amplified Fluorescence Image Recovery (SAFIRe). In this technique, primary and secondary lasers are used to modulate ground and dark-state populations, respectively.[10, 61] Because optical contrast is directly modulated, these concepts should be directly transferrable to PA detection and yield strong PA signals that are essentially independent of background absorbers. Similar to fluorescence imaging, photoacoustic contrast is also generated by optical absorption, thereby opening the possibility of gating signals by optically controlling dye populations in ground and intermediate states.

Optical modulation in photoacoustics (SAPhIRe), utilizes modulatable dyes that have long-lived intermediate states with distinct absorption spectra. The primary/pump laser prepares the intermediate state population while the delayed, long-wavelength

secondary/probe laser excites the prepared intermediate state to regenerate the ground state. As intermediate states last for many microseconds, acoustic waves generated by pump and probe lasers should not overlap temporally, enabling removal of all non-gated PA signals of endogenous chromophores via SAPhIRe, and result in background free PA signals.

PA signals are maximized with strongly absorbing chromophores that efficiently dump absorbed excitation energy in their surroundings through rapid non-radiative decay. Put simply, strongly absorbing, low fluorescence quantum yield fluorophores make for ideal PA contrast agents. The high triplet quantum yield of the xanthene, rose bengal, makes it an ideal choice to investigate optical modulation in photoacoustic imaging.

6.3 Single Element Photoacoustic Modulation

6.3.1 Pulsed Primary - CW Secondary Illumination

Initial investigations of photoacoustic modulation were performed using pulsed 532nm primary (10kHz repetition, 60 mJ/cm^2 fluence) and lower energy 830nm CW secondary co-illumination (fluence 200mJ/cm^2). In this study, primary laser excitation alone (532nm) yields strong photoacoustic signals (~ 10MHz frequency) from rose bengal. Secondary illumination, however, only depopulates the primary laser-prepared dark state of rose bengal without generating any photoacoustic signal by itself as described in Section 1.5. The secondary laser was mechanically chopped at 1 kHz. Because the primary laser had a repetition rate of 10kHz, a contrast agent with an intermediate lifetime >100μs needs to be used. If not, the population in that state would decay back to the ground state naturally between each subsequent primary pulse, in which case no difference would be observed with or without secondary illumination.

PVA immobilized rose bengal has an efficiently populated, long-lived dark state (~250μs) due to limiting oxygen quenching. This dark state absorbs broadly, enabling long wavelength secondary (830nm) co-illumination to more rapidly deplete the triplet in favor of the ground state. Modulating the secondary laser thereby modulates RB ground state population and therefore PA signals resulting from ground state absorption at 532nm. 532nm-excited PA signals under co-illumination at 830nm are ~2-fold larger than those from primary pulsed excitation alone (Figure 6-1). The true gain, however, is in signal visibility as modulation of the CW laser selectively modulates only the RB signal, thereby enabling its selective recovery. The Fourier transform shows the unique signature of the modulatable PA dye signal at 1kHz (Figure 6-3)

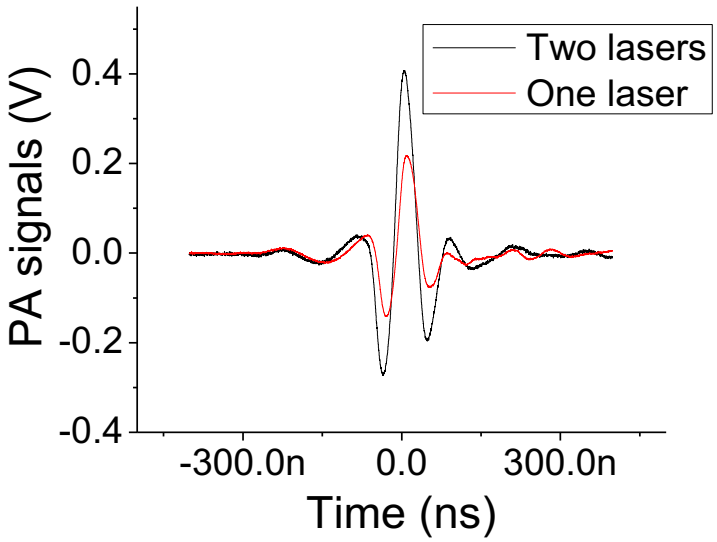

Figure 6-1 Photoacoustic signal comparison between one and two laser illumination

The initial results observed with the rose bengal were very promising. A Fourier transform of the photoacoustic signals gave a peak at 10kHz corresponding to the repetition rate of the primary laser. When a modulated, the secondary laser is also used at peak

modulation frequency, 1kHz. For this case, the 1kHz peak is observed, along with peaks corresponding to the sum and difference of the frequencies of the primary repetition rate and the secondary modulation frequency.

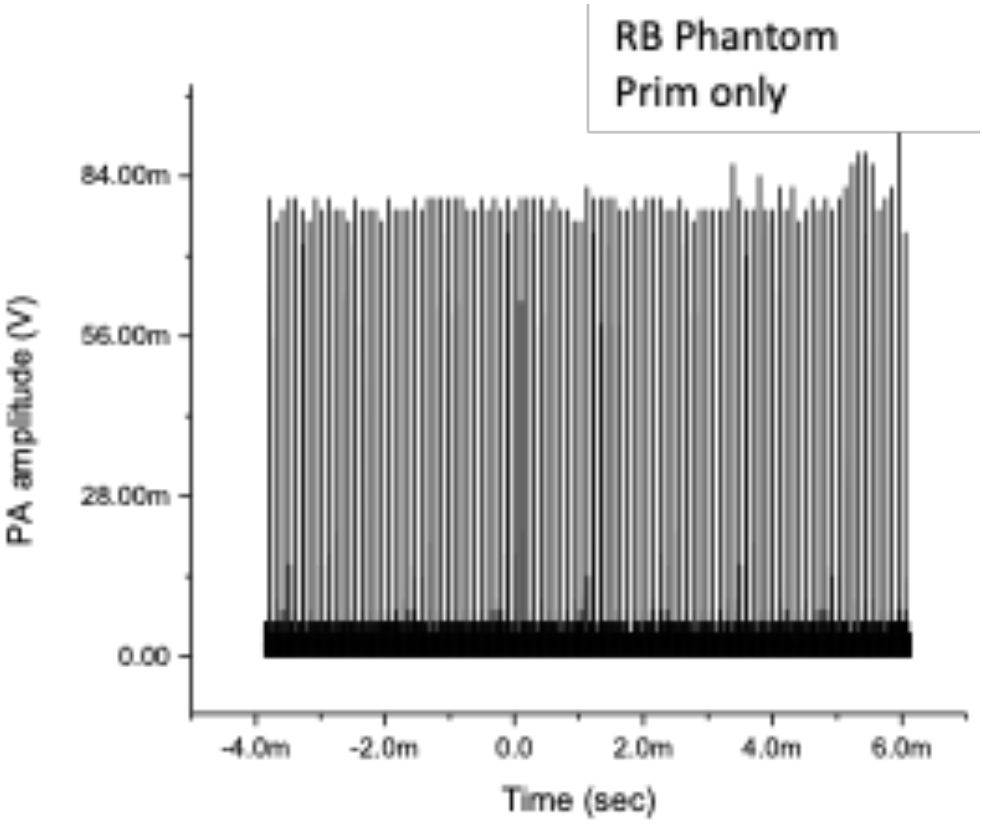

Figure 6-2 Photoacoustic signal from rose bengal PVA phantoms under primary only (532nm 10kHz) excitation

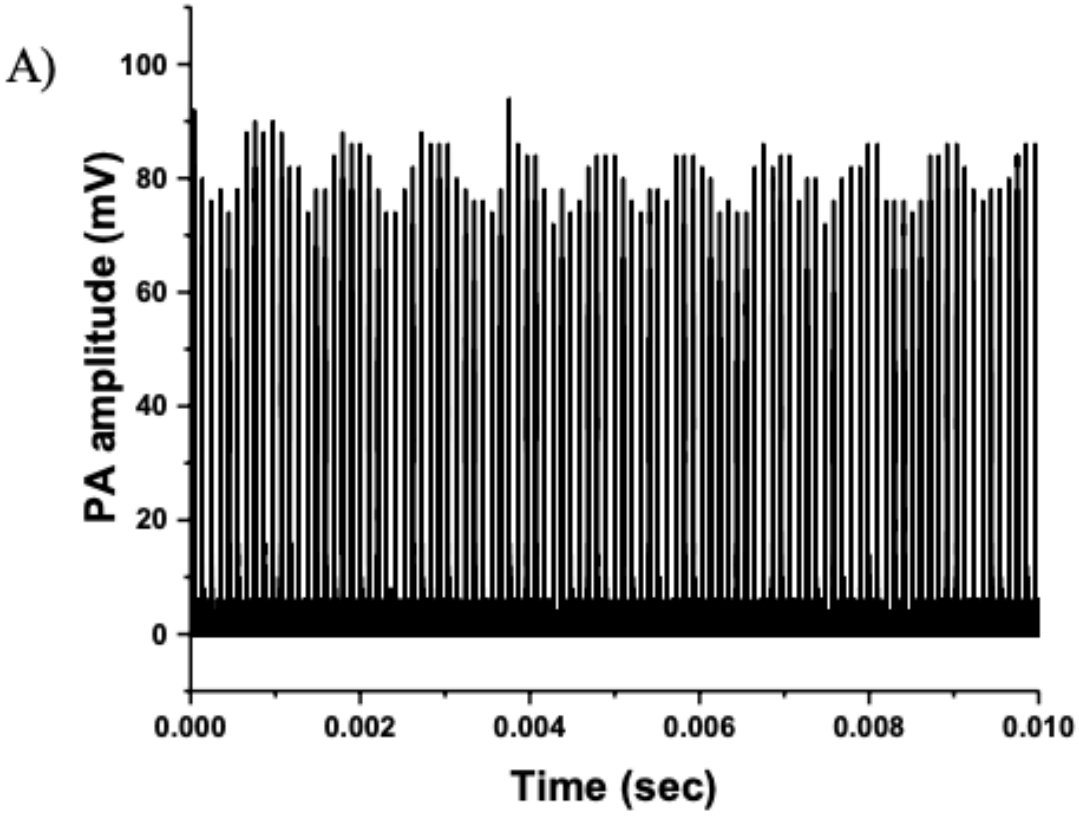
A)
PA amplitude (mV)
100
80
60
40
20
0
0.000
0.002
0.004
0.006
0.008
0.010
Time (sec)

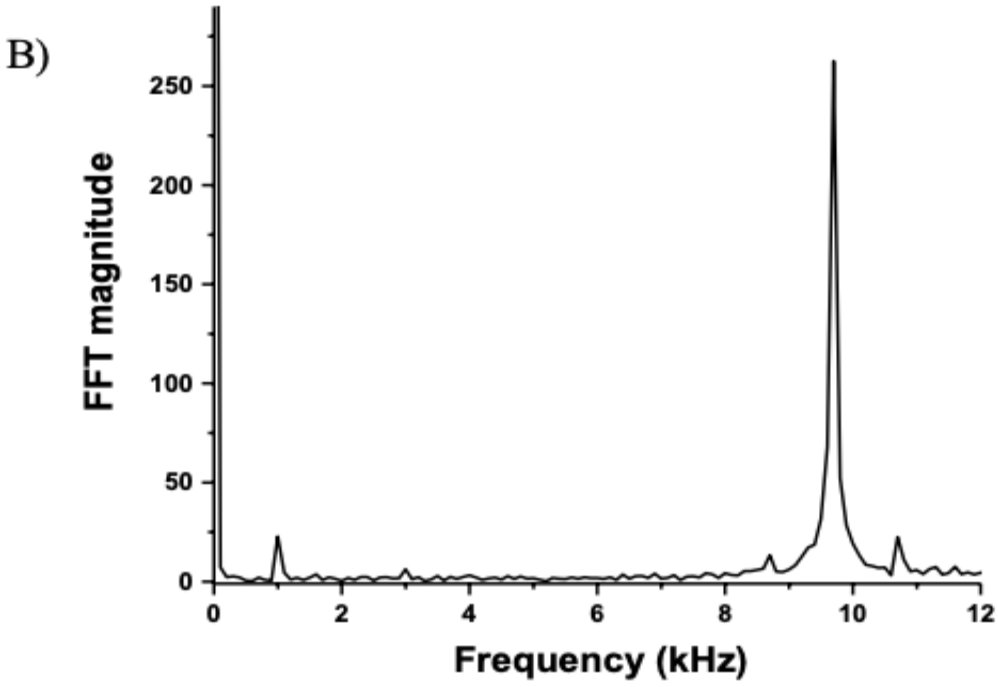
B)
FFT magnitude
250
200
150
100
50
0
0
2
4
6
8
10
12
Frequency (kHz)

Figure 6-3 A) Photoacoustic signal from eosin Y PVA phantoms with 532nm 10kHz primary excitation with co-illumination at 830nm (CW) secondary laser modulated at 1kHz. B) FFT of modulated signal showing peaks at both primary laser repetition rate and secondary modulation and their sum and difference.

Unfortunately, upon further investigation and comparison with a non-modulatable control such as graphene, which has a broadband absorption but no long-lived transient state, we observed similar modulation of the photoacoustic signals generated as seen in Figure 6-4, which should not be the case.

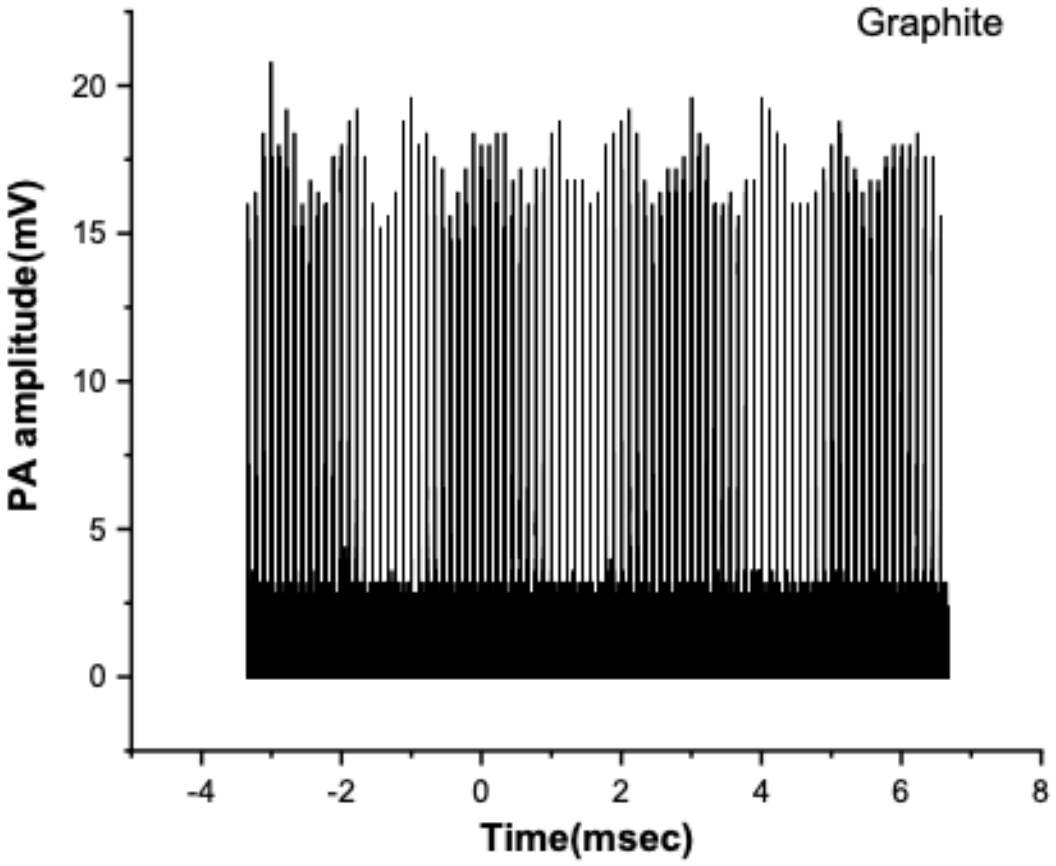

Figure 6-4 Photoacoustic signal from graphite PVA phantoms with 532nm 10kHz primary excitation with co-illumination at 830nm (CW) secondary laser modulated at 1kHz showing similar modulation of primary induced photoacoustic signal upon CW secondary modulation

The modulation-like response is a result of the increase in temperature that is likely a result of the presence of a continuous wave secondary illumination. Researchers have shown that the tissue Grüneisen parameter, Γ, is affected by temperature and is given by Equation 8. Γ is a dimensionless, multicomponent parameter which represents the thermoelastic properties of the material.[115-116] It has contributions from the specific heat capacity at constant pressure (C_p), speed of sound for longitudinal waves (V_s), and the coefficient of thermal expansion (β). The latter two are temperature dependent quantities. Shah et. al. has shown that a temperature increase from 20^0C to 30^0C results in a 50% increase in β.[117] Thus, one must ensure that PA modulation does arise from modulating the sample temperature due to laser illumination, but instead comes from modulation of contrast agent populations.

$$\Gamma = \frac{\beta V_s^2}{C_p} \qquad \textbf{Equation 9}$$

6.3.2 Pulsed Primary - Pulsed Secondary Illumination

In order to circumvent the heat generation upon secondary laser illumination, we worked with Donald VanderLaan in the Emelianov group at Georgia Tech to implement pulsed primary and secondary excitation schemes with photoacoustic detection. Pulsed primary laser (532nm, 5kHz repetition rate) along with a pulsed secondary (1064nm, 5kHz repetition rate) both with 10ns pulse widths were used as primary/pump and secondary/probe lasers. A short delay (100ns-10μs) was introduced between the primary and secondary laser pulses, with the secondary laser firing after primary, to temporally resolve the pump- and probe-induced photoacoustic signals from each other. The primary laser was allowed to fire for the first half of the period and turned off for the latter half

while the secondary fires all the time. For the modulatable dyes there should be no signal from the 1064nm illumination if there is no 532nm preceding it. The setup and the pulse sequences used are given in Figure 2-12 and Figure 2-13 respectively. Moreover, because both lasers used are pulsed lasers, temperature increase is no longer an issue. Because the samples used are flat, signals can be thought of as appearing from only one point in time on the ultrasound recording, allowing us to consider any other signal outside this narrow window as pure noise. Treating the signal in this window as a single data point, we can assume that signal is a single data point every 5KHz, with each data point corresponding to the photoacoustic response from each primary or secondary pulse. Because we are only interested in seeing the signal response from secondary excitation with and without primary, we can record only the time when the secondary laser fires (circled region in Figure 6-5) and ignore any photoacoustic signal generated by primary excitation. Figure 6-6 shows the results obtained under 532nm and 1064nm co-illumination for rose bengal, where no signal is observed when exciting at 1064nm alone without 532nm pre-illumination.

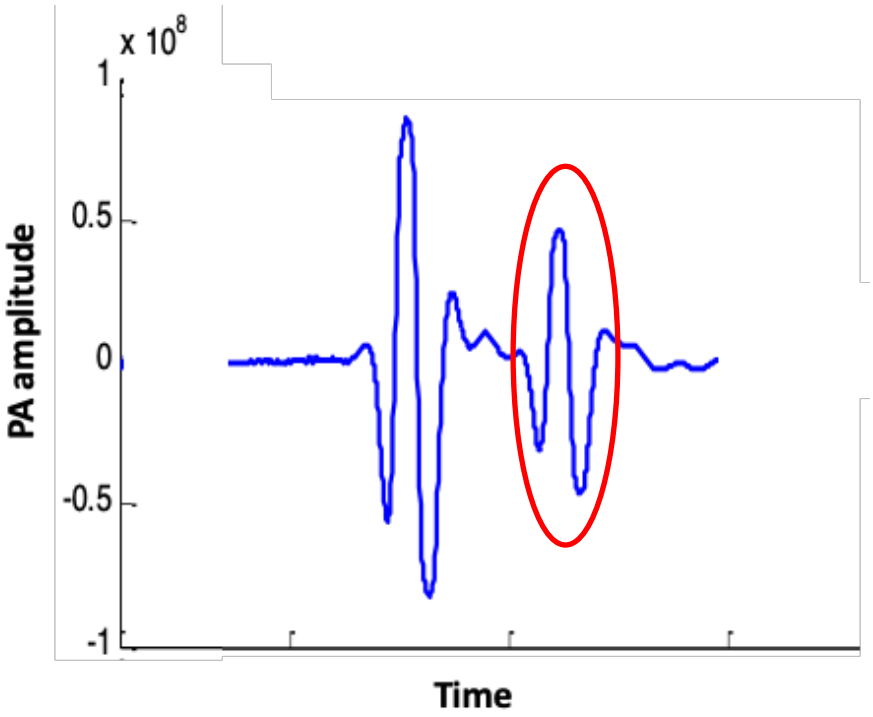

Figure 6-5 Photoacoustic signal generated by illumination at 532nm and consecutive 1064nm of rose bengal in PVA phantoms. Red circled region shows location of signal due to 1064nm and only that is monitored.

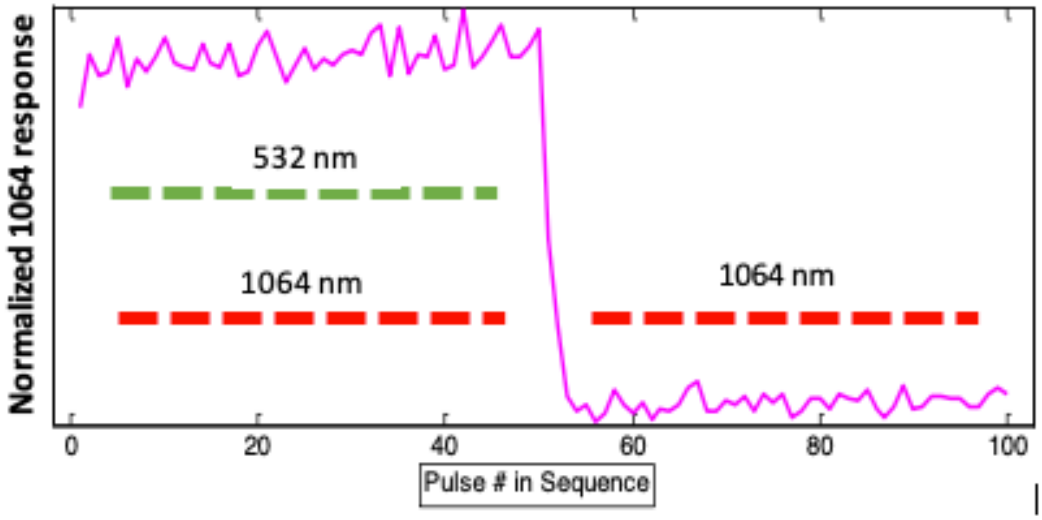

Figure 6-6 Photoacoustic signals generated by multiple 1064nm excitation pulses of rose bengal in PVA phantom with and without 532nm pre-illumination showing no signal generation with 1064nm only. First 50

pulses have a 532nm pump pulse 10μs prior to the probe 1064nm pulse while the last 50 only have 1064nm probe pulses clearly showing that there is no 1064nm response when primary (532nm) laser is turned off.

6.3.3 Dual Laser Modulation

We next employed a dual modulation scheme where we used external choppers in the path of each beam as shown in Figure 2-14. Both primary and long wavelength secondary illumination generates photoacoustic contrast from our dyes, but unlike the endogenous contrast agents, the secondary-induced signal in the optically modulatable dyes is only present if the primary pulse initially prepared this intermediate state. Dual modulation of the primary and secondary lasers will yield PA signal that correspond to the sum (ν_+) and difference (ν_-) of the modulation frequencies of the two lasers, whereas endogenous agents will only have signals at the corresponding modulation frequencies and not the sum and difference frequencies. Because the signals at ν_+ and ν_- are effectively background-free, detector noise becomes the main limit to signal visibility enabling improvements in signal. These approaches have enabled us to selectively recover dye signals from otherwise overwhelming background environments. As absorption is modulated through dynamically altering ground state populations, we have demonstrated the ability to modulate photoacoustic signals as well.

To create modulatable photoacoustic (mPA) contrast agents for detection in blood-laden background, we increased local modulatable dye concentration through incorporation in (biodegradable) silica nanoparticles. We incorporated rose bengal into sub-100nm diameter silica nanoparticles using a modified Stöber process described in section 2.1.3. Rose bengal-doped SiO_2 nanoparticle (RB-Si NP) size was confirmed via TEM (Figure 6-7). UV-vis measurements of RB absorption coupled with measured

nanoparticle particle densities were used by a lab member Md Shariful Islam to reveal a per-particle RB concentration of ~ 5mM.

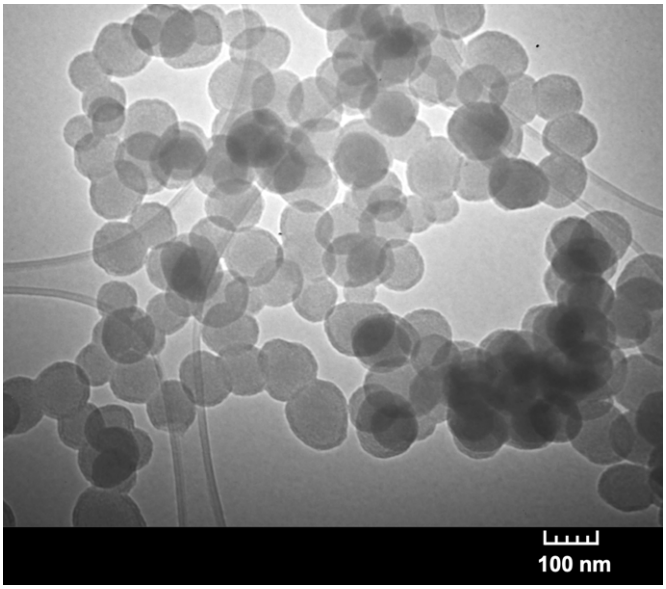

Figure 6-7 TEM of rose bengal doped silica nanoparticles (Diameter = 95±14nm)

Encapsulation in silica nanoparticles lengthens the triplet lifetime of rose bengal by limiting the oxygen mobility or by reducing oxygen access to the dye triplets. As both fluorescence modulation and PA modulation rely on optically controlling intermediate state populations, modulated fluorescence and triplet lifetimes of rose bengal in silica particles were characterized with fluorescence as a surrogate using previously described dual laser techniques. The modulation depth (the increase in fluorescence with two lasers over one laser) of silica nanoparticles was determined to be ~40% and the OADF decay method was used as a direct measurement of the triplet state lifetime which was determined to be ~20 μs – long enough to probe the optically gated probe PA signal while temporally separating it from the pump-induced photoacoustic signal. Though a delay was used in this instance it was not necessary.

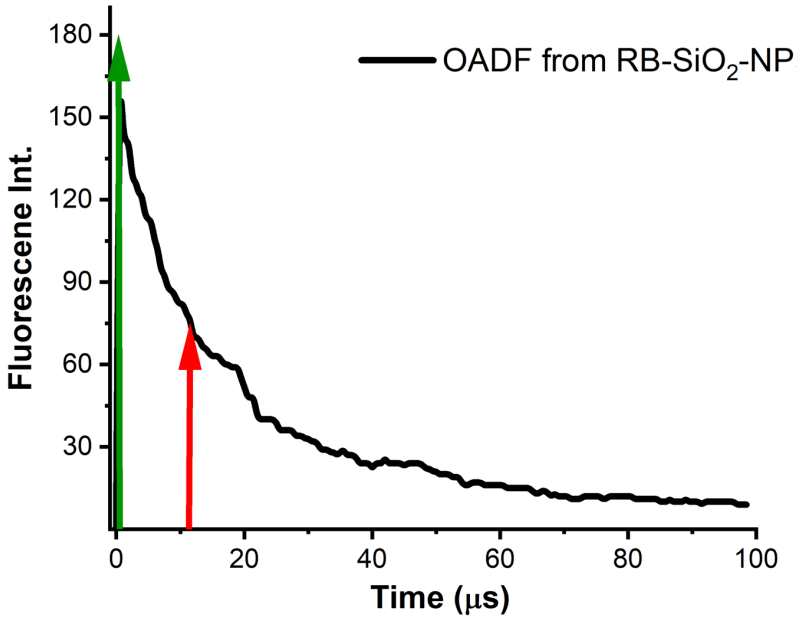

Figure 6-8 OADF decay of RB-SiO_2 nanoparticles upon probe illumination with green arrow indicating time of pump and red showing probe delay. Exponential fit of this decay indicates an intermediate state lifetime of 20 μs

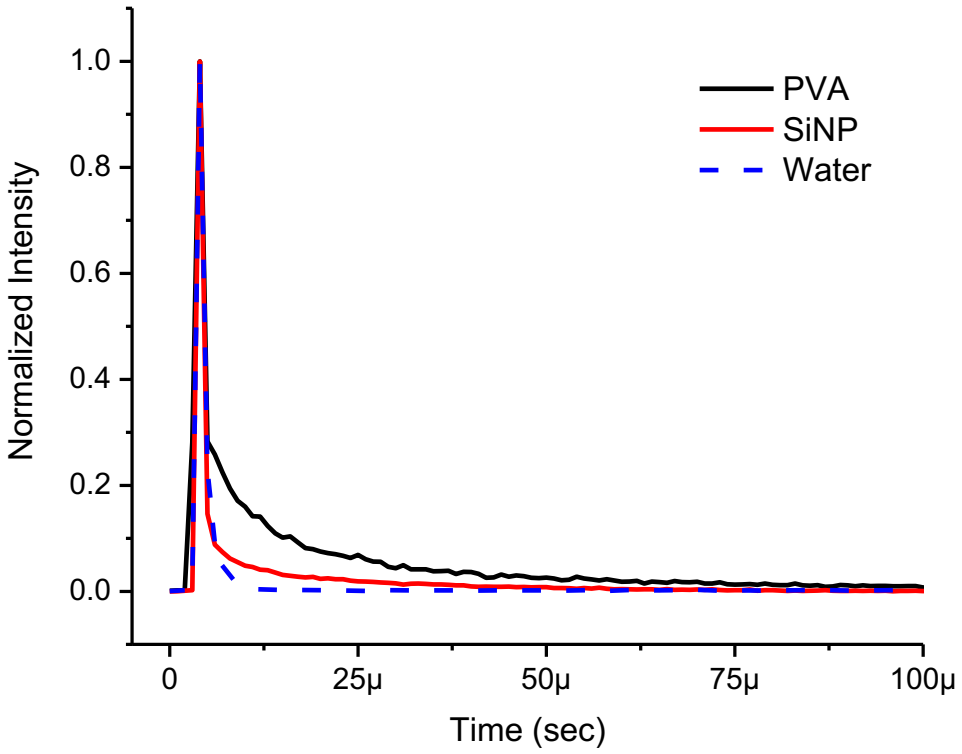

Figure 6-9 Comparison of OADF decay of rose bengal in silica nanoparticles, immobilized in PVA and in water solution showing PVA having longest triplet lifetime followed by silica nanoparticles.

In order to check if we could recover or modulatable silica nanoparticle signals from a blood background we mixed our RB-SiO_2 nanoparticles in 10% blood solution. 532nm and 1064nm lasers were used as pump/primary and probe/secondary excitation sources, respectively. The lasers were operated at a 5kHz repetition rate and both had pulse durations around 10ns. Laser pulse energy was controlled such that the local fluence was 35mJ/cm^2 and 48mJ/cm^2 for the 532nm pump pulse and 1064nm probe pulses, respectively. Independent amplitude modulation of the pump and probe excitation beams was accomplished via beam chopper placed in each of the beam paths prior to where they combine onto one optical axis. Pump and probe modulation frequencies were 23Hz and 129Hz. Modulated photoacoustic (mPA) signals of dyes are proportional to the product of

primary and secondary intensities. Consequently, independent modulation of both excitation lasers generates PA signals corresponding to the sum and difference of the two lasers' modulation frequencies, see Figure 6-10. This sequential two-photon process was only observed from our modulatable dyes. Because signals from any (non-modulatable) endogenous chromophores would only be linearly dependent on either individual laser intensity, and not their product, signals appearing at the sum and difference frequencies essentially background free.

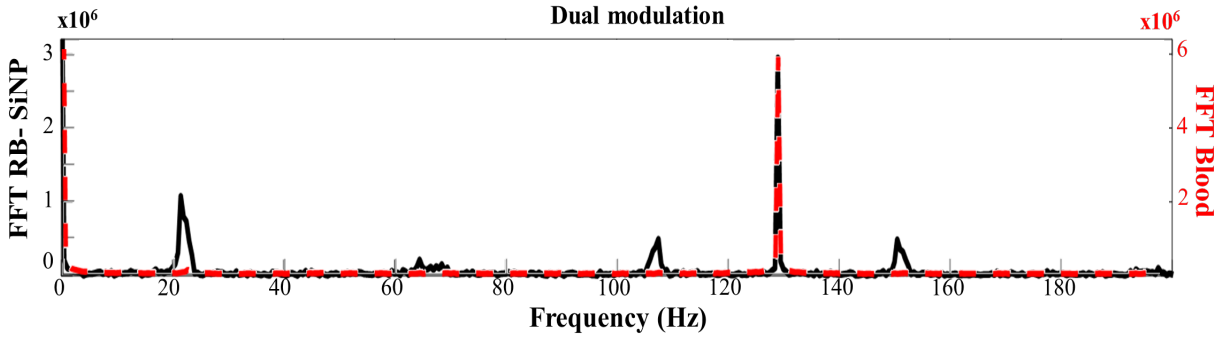

Figure 6-10 Photoacoustic signal from RB-SiO_2NP (black) and blood (red) under primary 23Hz and secondary 129Hz dual modulation showing the prescence of peaks at the sum and difference frequencies of the modulation in the RB-SiO_2NP but not in blood.

6.4 Array Based Modulated Photoacoustic Image Recovery

6.4.1 Phantom Modulation

The method was tested on a tissue-mimicking phantom using full-field photoacoustic imaging. Figure 6-11 shows a photograph of the phantom used. The bulk material was composed of tissue-mimicking synthetic rubber (Hummic Medical #5 gel) mixed with 2% silica powder to provide ultrasound scattering. Within the rubber body were placed two blood-laden inclusions, one with and one without RB-SiO_2 NPs added. The

inclusions were constructed by using tissue mimicking alginate phantoms, where both nanoparticle suspensions and blood were mixed with 10%wt sodium alginate solution in a 1:1 volume ratio and poured into a template. Crosslinking occurs by submerging templated solution into a calcium-containing aqueous solution ($CaCl_2$) for 10 minutes, after which the template can be removed, and inclusions incorporated into larger bulk synthetic rubber phantom.

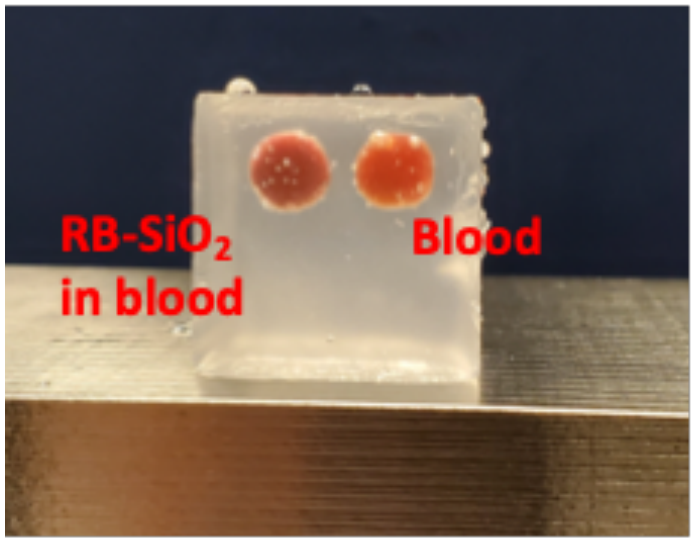

Figure 6-11 Picture of phantom used for array based imaging. The two separate inclusions with a mixture of rose bengal doped silica nanoparticles and blood and only blood are made from alginate where the clear part is made of bulk rubber with silica powder added for scattering.

Pulsed pump excitation at 532nm (~10ns, 30 Hz, 30mJ/pulse) generates strong photoacoustic signals from blood and from RB-SiO_2 nanoparticles. Pulsed probe excitation at 1064nm (~10ns, 30 Hz, 30mJ/pulse) also generates photoacoustic signals from blood, but no signals from RB-SiO_2 nanoparticles are produced unless it is pre-illuminated at 532nm. Such optical preparation of the intermediate state enables simple subtraction of 1064nm-generated signals, with and without 532nm pre-illumination, to selectively

recover pure RB PA signals. We constructed tissue phantoms to assay detection of RB@SiO_2 nanoparticles in blood-laden inclusions via photoacoustic imaging (SAPhIRe). While both samples showed pump-only and probe-only PA signals, only phantoms containing RB-SiO_2 nanoparticles exhibited additional probe-induced signals that had to be preceded by 532nm pump excitation to prepare the intermediate state. Phantoms were imaged using both ultrasound and photoacoustic detection with a research-grade commercial ultrasound imaging system (Vantage 128, Verasonics Inc.), along with two Nd:YAG lasers (Tempest, New Wave Research, and Gemini PIV, New Wave Research). The two beams were spatially combined on a dichroic mirror and passed through a diffuser before impinging on the phantom, which was submerged in a water tank to provide ultrasound coupling with the detection transducer. Illumination was normal to the ultrasound imaging plane. Each SAPhIRe image was generated by subtracting a single probe-only PA image from that resulting from consecutive pump (532nm) and probe (1064nm) excitations. Delay between pump and probe was set to 8 μs to minimize overlap betwen photoacoustic signals generated by each laser while retaining significant intermediate state population. Software was written to perform image subtraction and SAPhIRe image recovery in real time, allowing for SAPhIRe images to be obtained within 100 ms for 30 Hz laser excitation. As shown in Figure 6-12 the RB-SiO_2-NP inclusion generates no 1064nm-only-induced PA signals, however, when primed by 532nm, the large photogenerated intermediate state population responds strongly to the subsequent 1064nm pulse. The blood inclusion responds identically to the 1064nm irradiation, regardless of initial excitation by 532nm, enabling direct subtraction of 1064-generated PA signals to near perfectly eliminate blood PA signals.

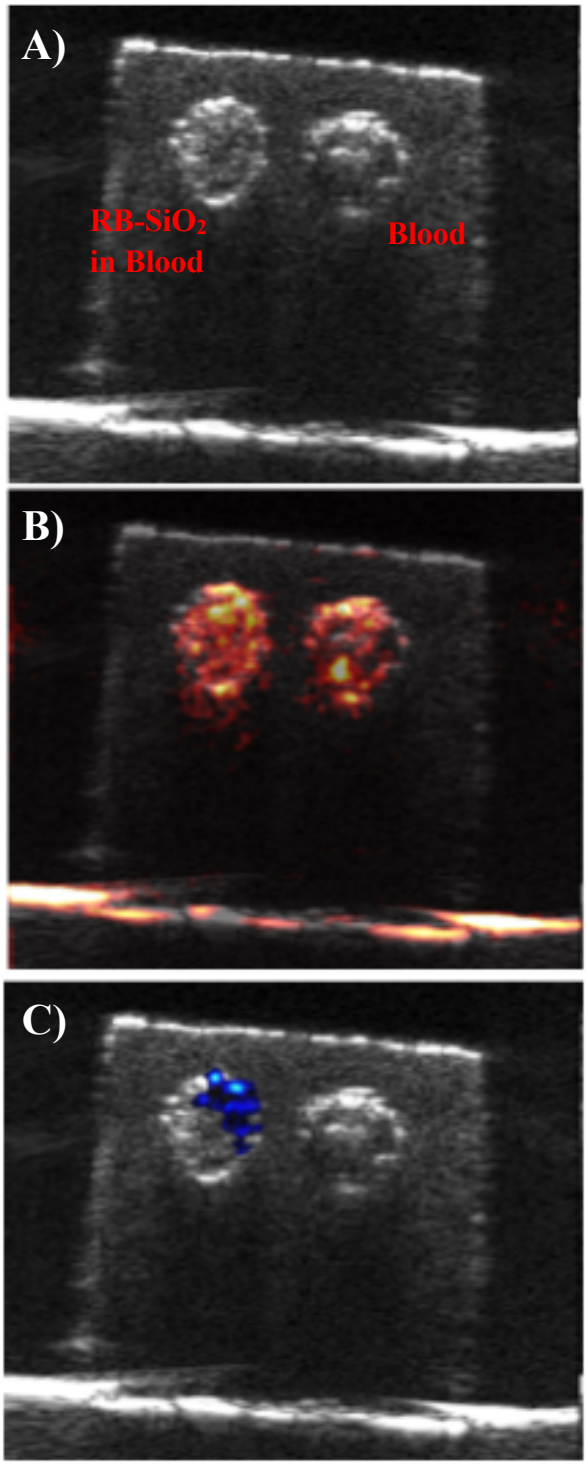

Figure 6-12 A) Ultrasound image of phantom showing both inclusions. B) photoacoustic signals from 532nm pump overlaid on ultrasound showing signal from both inclusions. C) SAPhIRe image generated by subtracting PA signal obtained with probe laser (1064nm) only from signal obtained

with both pump and probe (532nm + 1064nm) showing suppression of background (i.e., blood) signal.

6.4.2 Ex-Vivo Imaging

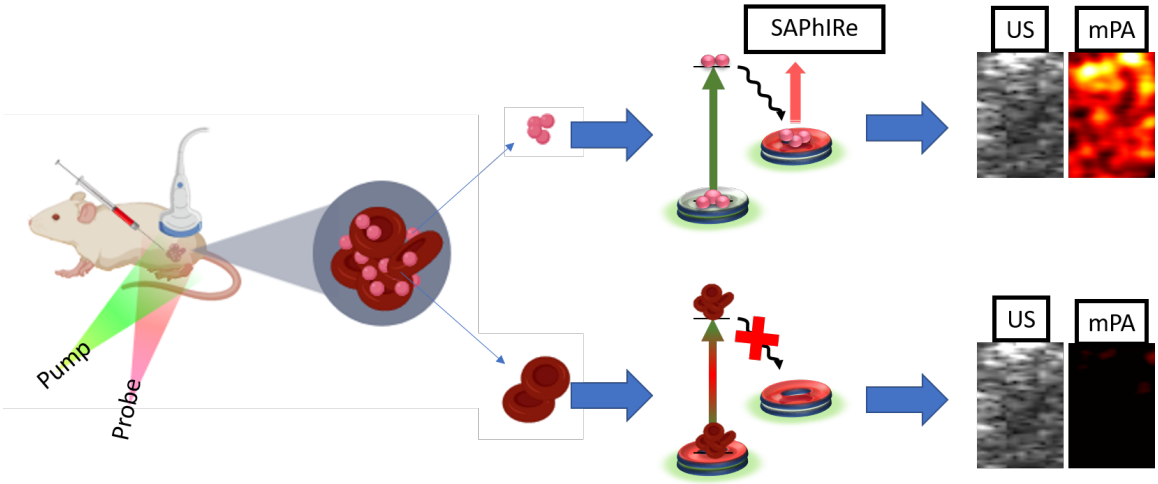

Figure 6-13 SAPhIRe imaging paradigm illustrating the different photophysical states affected by excitation at 532nm (green arrow) and 1064nm (red arrow) in optically modulatable (OM) contrast agents versus blood.

To demonstrate the potential of SAPhIRe, even while using poorly penetrating 532nm pump excitation, we intramuscularly injected 50 μL of aqueous solutions of RB-SiO_2 nanoparticles into the left hamstrings of intact rat carcasses. Rodents were imaged and illuminated from opposite sides, with the US transducer lateral and the optical excitation impinging on the medial surface (Figure 6-14). Fur was removed from both surfaces, but skin was intact. Ultrasound and photoacoustic images (16 by 40 mm) are shown in Figure 6-15, rendered with logarithmic compression. Dynamic range is 40dB for US and 32dB for PA and SAPhIRe images, with below-range signals mapped transparently for color data. The bolus injection is discernable via both SAPhIRe and US, the latter due to the relatively high scattering by the particles of US, enveloped in the less echoic muscle

tissue. Strong PA signals dominate the component images where the light enters the tissue, as expected with intact skin. Despite the strong subsurface fluence effects, the bolus injection is readily apparent in the composite SAPhIRe image, as background PA is nearly completely suppressed. The injection trajectory, from the US image perspective, was directed upward, arriving from below – so expected trace signal is observed in SAPhIRe from contrast that leaked out through the injection tract. PA signal is absent on the left sides of all images as this region was not illuminated with either laser.

Despite very strong contrast, the optical fluences employed were far below ANSI limits: The incident 532nm pump radiation was 3 mJ/cm^2, while the 1064nm probe fluence was 7 mJ/cm^2. This implies we would have been able to successfully detect far lower concentrations of particles, because, i) the signal strength here is already very high, and ii) we are able to increase the laser intensity by a factor of ~15 before exceeding ANSI limits.

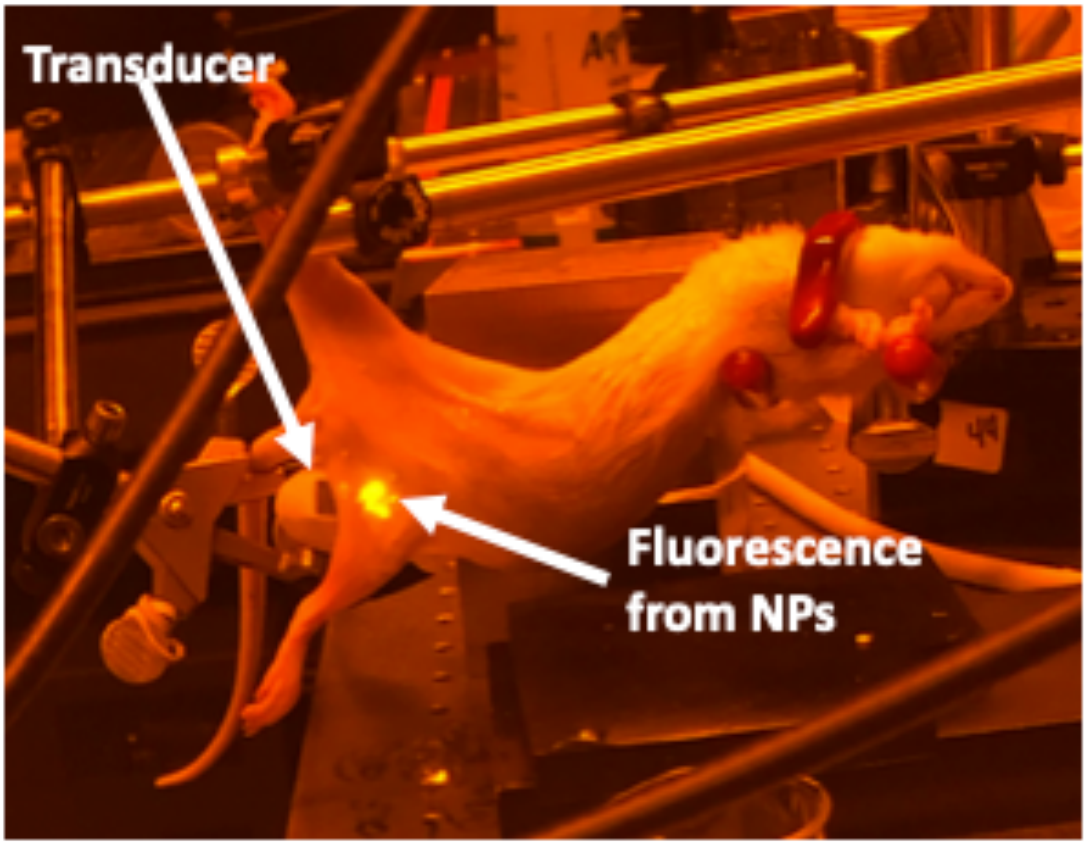

Figure 6-14 Photo of the rat carcass used and experimental setup for photoacoustic modulation. Photo was taken when 532nm was firing through filters that block both 532nm and 1064nm, which facilitates the visibility of fluorescence from the bolous injection of RB-SiO_2 nanoparticles.

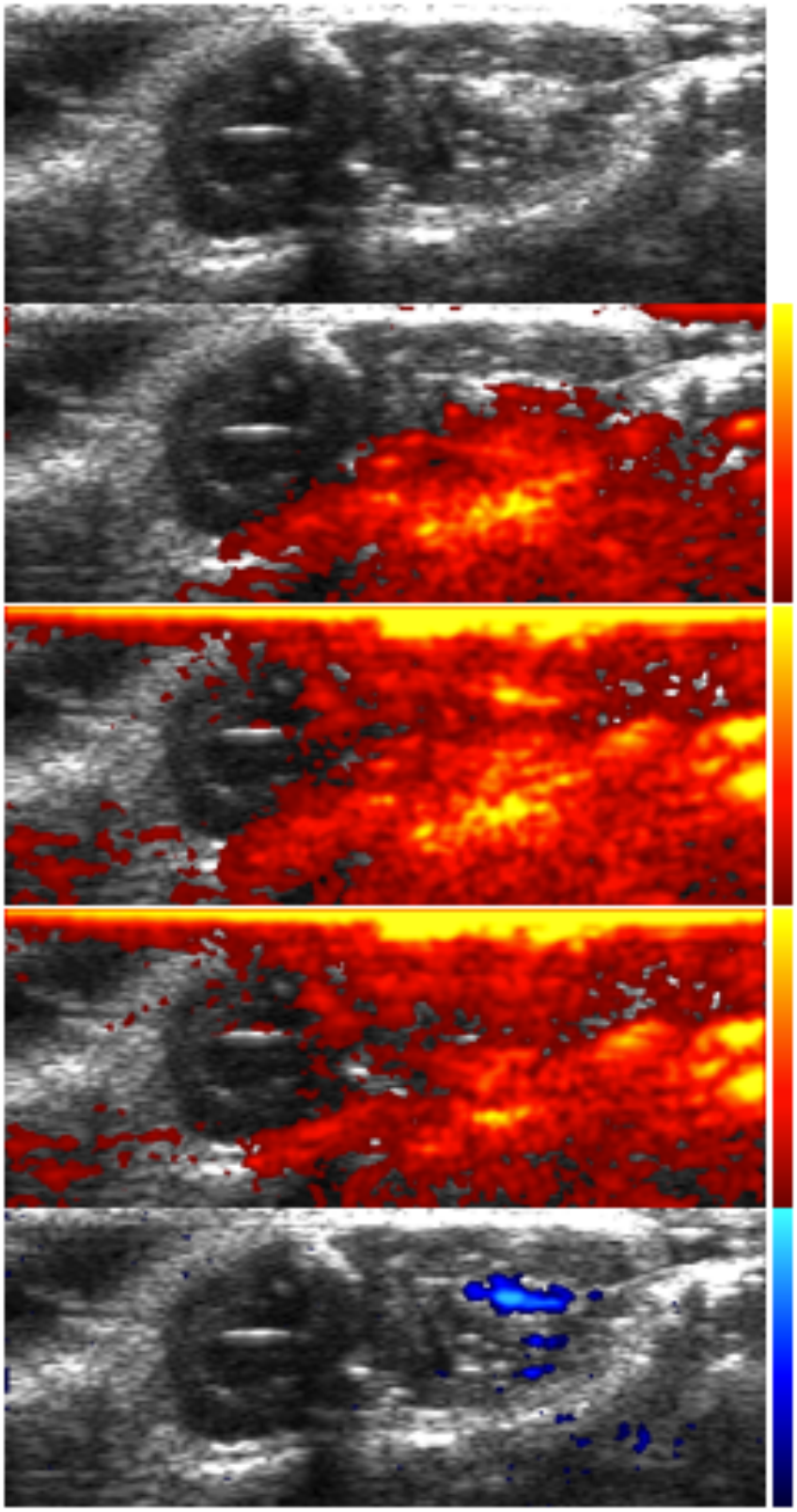

Figure 6-15 Ex-vivo photoacoustic results. A) Post-injection ultrasound image. The bolus is visible as an oblong echoic region. B) PA overlay using both pump and probe excitations. C) PA overlay using pump excitation. D) PA overlay using probe excitation. E) SAPhIRe overlay. The bolus (echoic US region) and SAPhIRe signal overlap very well. Signal also present along the injection trajectory. All images have 40dB and 32dB dynamic range for US and PA / SAPhIRe, respectively.

6.5 Conclusion

Modulated photoacoustic excitation of optically modulatable dyes enables similar depth penetration, but complete background avoidance as compared with standard single-laser photoacoustic detection. Because signals of interest are shifted to background-free detection windows, signal visibility and sensitivity become limited only by detector sensitivity. We have presented a real time background rejection paradigm for PA imaging with significant signal enhancements over background. RB-SiO_2-NP not only allow for background suppression in photoacoustic imaging, but also offer a path to a dual imaging modality of modulated photoacoustic and fluorescence imaging (SAFIRe). Further SAPHIRe/SAFIRe techniques can be used to distinguish among several probes simultaneously using contrast agent photophysical properties.

CHAPTER 7. CONCLUSION AND FUTURE OUTLOOK

The fluorescence modulation based on dark state photophysics has been studied in xanthenes and merocyanine 540. These transient states offer different modulation properties depending on their fluorescence recovery pathways. For xanthenes, modulation can be achieved either by accessing the singlet excited state (S_1) through RISC from a higher triplet excited state (T_n) or by returning to S_0 through non-radiative pathways. Dyes with heavier halogens attached to the chromophore will give higher triplet quantum yields but will also have relatively faster triplet lifetimes.[118] Fluorescein, despite being an excellent fluorophore, has also been shown to have significant triplet population recovery under oxygen deprived conditions.

Merocyanine 540, on the other hand, has both photoisomer and triplet dark-states that take part in long wavelength modulation. Through pulsed excitation we showed that the photoisomer dark state molecules return to the emissive manifold's ground state (trans-S_0) while the triplet dark state molecules return to the excited state (trans-S_1), yielding additional fluorescence. In all the studied systems, oxygen has been shown to play an important role in the modulation dynamics of triplets. Conditions that limit oxygen concentration or mobility have been shown to increase OADF percentage. With these guiding insights, other fluorescent molecules with similar photophysical properties can be designed and tested for potential applications in background-free fluorescence and/or photoacoustic imaging.

The ultimate goal of using modulation for photoacoustics is to develop a noninvasive molecular imaging technology, ultrasound guided modulated photoacoustic

imaging (US-mPA) and demonstrate the developed approach in the background-free detection of micrometastases in sentinel lymph nodes using murine model of metastatic breast cancer and finally enabling design and development of a clinical imaging system and contrast agents for background-free molecular imaging of various other pathologies. This approach makes use of previously discussed optically activatable imaging contrast agents in combination with the corresponding PA/ultrasound imaging device.

Future directions for this project involve selecting modulatable dyes with red shifted absorptions such as small atom silver clusters and cyanines. Because, 532nm excitation wavelength is too short to be practical for medical imaging small atom silver-DNA clusters with 650nm/710nm (absorption/emission) will be synthesized and encapsulated in silica nanoparticles as per published procedure. [119-120] Furthermore, since the silver clusters degrade into silver ions and short ssDNA oligos once the encapsulating silica nanoparticle dissolves, they offer a means of easily clearing the body. Because triplet states are oxygen dependent, triplet lifetimes of the optically modulated contrast agents can be explored for use in investigating oxygen saturation of local environment.

Oxygen accessibility for each silica encapsulated dye can be determined by determining the triplet lifetime of each nanoparticle under varying oxygen levels in a controlled gas experimental chamber. Rb-SiO_2-NPs have been shown to be have a response to varying oxygen concentrations as shown in Figure 7-1. In an improvement to the methods presented here oxygen sensitivity of future optically modulatable nanoparticle contrast agents needs to be determined in a closed system with known oxygen concentrations. Figure 7-1 shows how the triplet lifetime of rose bengal loaded silica nanoparticles changes with oxygen concentration.

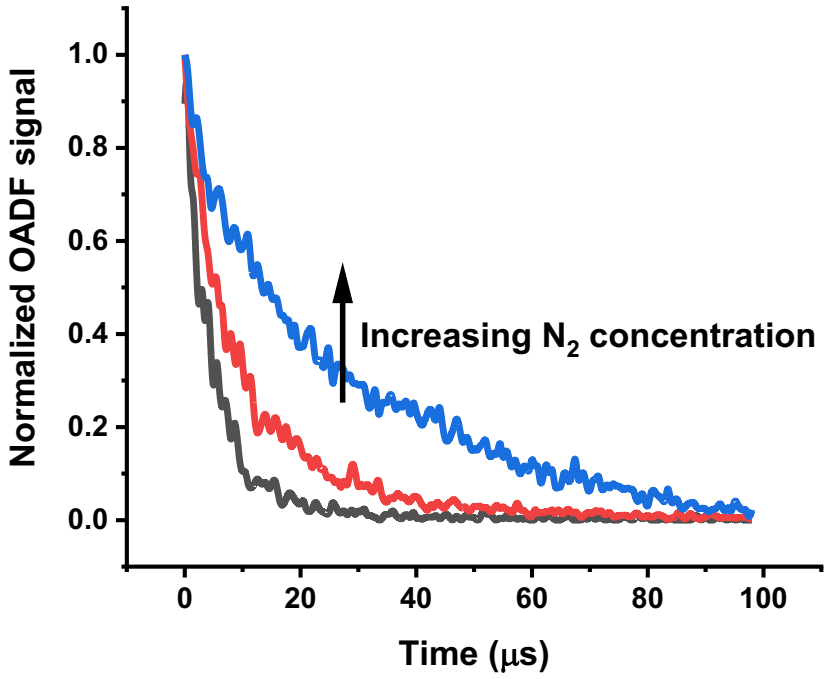

Figure 7-1 OADF from Rb-SiO_2-NPs showing change in triplet lifetime under varying oxygen concentrations. Experiement was done in an open system with constant nitrogen flowing above the sample.

In order to ensure delivery of these optically modulatable nanoparticles to the desired area these nano particles will be outfitted with targeting antibodies that select for HER2 which is overexpressed in breast cancer. Moreover, controlling the oxygen concentration allows for a near exact determination of lifetime that corresponds to each oxygen environment. This allows us to create a calibration curve of triplet lifetime vs oxygen concentration. This calibration curve will be created by using fluorescence but needs to be validated using PA measurements. In order to do this the secondary probe signal delay can be varied to map out the decay of the corresponding state. successful generation of this calibration curve will allow us to differentiate between contrast agents

experiencing different oxygen saturation levels simply by measuring the lifetimes of the dark states, ultimately allowing us to identify hypoxic conditions.

This technique makes it possible for dual ultrasound and photoacoustic imaging in which the ultrasound generated can act as a secondary image to outline the imaging environments. Because the nanoparticles will be targeted, they will selectively interact with membrane receptors on cancerous cells and can be used to determine micrometastases in sentinel lymph nodes. Moreover, the oxygen sensitivity of the triplet lifetime will allow for mapping out the hypoxic conditions in the imaging environment.

REFERENCES

1. Weissleder, R.; Pittet, M. J., Imaging in the era of molecular oncology. *Nature* **2008,** *452* (7187), 580-9.

2. Tokunaga, M.; Imamoto, N.; Sakata-Sogawa, K., Highly inclined thin illumination enables clear single-molecule imaging in cells. *Nature methods* **2008,** *5* (2), 159-61.

3. Sevick-Muraca, E. M.; Houston, J. P.; Gurfinkel, M., Fluorescence-enhanced, near infrared diagnostic imaging with contrast agents. *Curr Opin Chem Biol* **2002,** *6* (5), 642-50.

4. Truong, L.; Ferre-D'Amare, A. R., From fluorescent proteins to fluorogenic RNAs: Tools for imaging cellular macromolecules. *Protein science : a publication of the Protein Society* **2019,** *28* (8), 1374-1386.

5. Zorrilla, S.; Rivas, G.; Lillo, M. P., Fluorescence anisotropy as a probe to study tracer proteins in crowded solutions. *Journal of molecular recognition : JMR* **2004,** *17* (5), 408-16.

6. Zorrilla, S.; Lillo, M. P., Quantitative investigation of biomolecular interactions in crowded media by fluorescence spectroscopy, a good choice. *Current protein & peptide science* **2009,** *10* (4), 376-87.

7. Taylor, B. N.; Mehta, R. R.; Yamada, T.; Lekmine, F.; Christov, K.; Chakrabarty, A. M.; Green, A.; Bratescu, L.; Shilkaitis, A.; Beattie, C. W.; Das Gupta, T. K., Noncationic peptides obtained from azurin preferentially enter cancer cells. *Cancer research* **2009,** *69* (2), 537-46.

8. Feng, Y.; Mitchison, T. J.; Bender, A.; Young, D. W.; Tallarico, J. A., Multi-parameter phenotypic profiling: using cellular effects to characterize small-molecule compounds. *Nature reviews. Drug discovery* **2009,** *8* (7), 567-78.

9. Monici, M., Cell and tissue autofluorescence research and diagnostic applications. *Biotechnology annual review* **2005,** *11*, 227-56.

10. Fan, C.; Hsiang, J.-C.; Dickson, R. M., Optical Modulation and Selective Recovery of Cy5 Fluorescence. *ChemPhysChem* **2012,** *13* (4), 1023-1029.

11. Petty, J. T.; Fan, C.; Story, S. P.; Sengupta, B.; Sartin, M.; Hsiang, J.-C.; Perry, J. W.; Dickson, R. M., Optically Enhanced, Near-IR, Silver Cluster Emission Altered by Single Base Changes in the DNA Template. *J. Phys. Chem. B* **2011,** *115* (24), 7996-8003.

12. Hsiang, J.-C.; Jablonski, A. E.; Dickson, R. M., Optically Modulated Fluorescence Bioimaging: Visualizing Obscured Fluorophores in High Background. *Acc. Chem. Res.* **2014,** *47* (5), 1545-1554.

13. Chen, Y.-C.; Jablonski, A. E.; Issaeva, I.; Bourassa, D.; Hsiang, J.-C.; Fahrni, C. J.; Dickson, R. M., Optically Modulated Photoswitchable Fluorescent Proteins Yield Improved Biological Imaging Sensitivity. *Journal of the American Chemical Society* **2015,** *137* (40), 12764-12767.

14. Richards, C. I.; Hsiang, J.-C.; Dickson, R. M., Synchronously Amplified Fluorescence Image Recovery (SAFIRe). *J. Phys. Chem. B* **2009,** *114* (1), 660-665.

15. Elson, E. L., Fluorescence correlation spectroscopy: past, present, future. *Biophys J* **2011,** *101* (12), 2855-2870.

16. Tian, Y.; Martinez, M. M.; Pappas, D., Fluorescence correlation spectroscopy: a review of biochemical and microfluidic applications. *Appl Spectrosc* **2011,** *65* (4), 115A-124A.

17. De Los Santos, C.; Chang, C.-W.; Mycek, M.-A.; Cardullo, R. A., FRAP, FLIM, and FRET: Detection and analysis of cellular dynamics on a molecular scale using fluorescence microscopy. *Mol Reprod Dev* **2015,** *82* (7-8), 587-604.

18. Becker, W., Fluorescence lifetime imaging--techniques and applications. *Journal of microscopy* **2012,** *247* (2), 119-36.

19. Mujumdar, R. B.; Ernst, L. A.; Mujumdar, S. R.; Lewis, C. J.; Waggoner, A. S., Cyanine dye labeling reagents: Sulfoindocyanine succinimidyl esters. *Bioconjugate Chemistry* **1993,** *4* (2), 105-111.

20. Seybold, P. G.; Gouterman, M.; Callis, J., Calorimetric, photometric and lifetime determinations of fluorescence yields of fluorescein dyes. *Photochem Photobiol* **1969,** *9* (3), 229-42.

21. Resch-Genger, U.; Grabolle, M.; Cavaliere, S.; Nitschke, R.; Nann, T., Quantum Dots Versus Organic Dyes as Fluorescent Labels. *Nature methods* **2008,** *5*, 763-75.

22. Zimmer, M., Green Fluorescent Protein (GFP): Applications, Structure, and Related Photophysical Behavior. *Chem Rev* **2002,** *102* (3), 759-781.

23. Tsien, R. Y., THE GREEN FLUORESCENT PROTEIN. *Annual Review of Biochemistry* **1998,** *67* (1), 509-544.

24. Chudakov, D. M.; Matz, M. V.; Lukyanov, S.; Lukyanov, K. A., Fluorescent Proteins and Their Applications in Imaging Living Cells and Tissues. *Physiological Reviews* **2010,** *90* (3), 1103-1163.

25. Baldridge, A.; Feng, S.; Chang, Y.-T.; Tolbert, L. M., Recapture of GFP Chromophore Fluorescence in a Protein Host. *ACS Combinatorial Science* **2011,** *13* (3), 214-217.

26. Jablonski, A. E.; Vegh, R. B.; Hsiang, J.-C.; Bommarius, B.; Chen, Y.-C.; Solntsev, K. M.; Bommarius, A. S.; Tolbert, L. M.; Dickson, R. M., Optically Modulatable Blue Fluorescent Proteins. *J. Am. Chem. Soc.* **2013,** *135* (44), 16410-16417.

27. Dickson, R. M.; Cubitt, A. B.; Tsien, R. Y.; Moerner, W. E., On/off blinking and switching behaviour of single molecules of green fluorescent protein. *Nature* **1997,** *388* (6640), 355-358.

28. Jablonski, A. E.; Hsiang, J.-C.; Bagchi, P.; Hull, N.; Richards, C. I.; Fahrni, C. J.; Dickson, R. M., Signal Discrimination Between Fluorescent Proteins in Live Cells by Long-Wavelength Optical Modulation. *The Journal of Physical Chemistry Letters* **2012,** *3* (23), 3585-3591.

29. Tsien, R. Y., Imagining Imaging's Future. *Nature Reviews Molecular Cell Biology* **2003,** *5* (9), SS16-SS21.

30. Chen, K.-Y.; Cheng, Y.-M.; Lai, C.-H.; Hsu, C.-C.; Ho, M.-L.; Lee, G.-H.; Chou, P.-T., Ortho Green Fluorescence Protein Synthetic Chromophore; Excited-State Intramolecular Proton Transfer via a Seven-Membered-Ring Hydrogen-Bonding System. *Journal of the American Chemical Society* **2007,** *129* (15), 4534-4535.

31. Hsieh, C.-C.; Chou, P.-T.; Shih, C.-W.; Chuang, W.-T.; Chung, M.-W.; Lee, J.; Joo, T., Comprehensive Studies on an Overall Proton Transfer Cycle of the ortho-Green Fluorescent Protein Chromophore. *Journal of the American Chemical Society* **2011,** *133* (9), 2932-2943.

32. Richards, C. I.; Choi, S.; Hsiang, J. C.; Antoku, Y.; Vosch, T.; Bongiorno, A.; Tzeng, Y. L.; Dickson, R. M., Oligonucleotide-stabilized Ag nanocluster fluorophores. *J Am Chem Soc* **2008,** *130* (15), 5038-9.

33. Yu, J.; Patel, S. A.; Dickson, R. M., In vitro and intracellular production of peptide-encapsulated fluorescent silver nanoclusters. *Angewandte Chemie (International ed. in English)* **2007,** *46* (12), 2028-30.

34. Michalet, X.; Pinaud, F. F.; Bentolila, L. A.; Tsay, J. M.; Doose, S.; Li, J. J.; Sundaresan, G.; Wu, A. M.; Gambhir, S. S.; Weiss, S., Quantum dots for live cells, in vivo imaging, and diagnostics. *Science* **2005,** *307* (5709), 538-44.

35. Yu, W. W.; Qu, L.; Guo, W.; Peng, X., Experimental Determination of the Extinction Coefficient of CdTe, CdSe, and CdS Nanocrystals. *Chemistry of Materials* **2003,** *15* (14), 2854-2860.

36. Parak, W. J.; Pellegrino, T.; Plank, C., Labelling of cells with quantum dots. *Nanotechnology* **2005,** *16* (2), R9-r25.

37. Derfus, A. M.; Chan, W. C. W.; Bhatia, S. N., Probing the Cytotoxicity of Semiconductor Quantum Dots. *Nano Letters* **2004,** *4* (1), 11-18.

38. Lewinski, N.; Colvin, V.; Drezek, R., Cytotoxicity of nanoparticles. *Small (Weinheim an der Bergstrasse, Germany)* **2008,** *4* (1), 26-49.

39. Chan, W. C. W.; Nie, S., Quantum Dot Bioconjugates for Ultrasensitive Nonisotopic Detection. *Science* **1998,** *281* (5385), 2016.

40. Verwey, E. J. W., Theory of the Stability of Lyophobic Colloids. *The Journal of Physical and Colloid Chemistry* **1947,** *51* (3), 631-636.

41. Rust, M. J.; Bates, M.; Zhuang, X., Sub-diffraction-limit imaging by stochastic optical reconstruction microscopy (STORM). *Nature methods* **2006,** *3* (10), 793-5.

42. Shroff, H.; Galbraith, C. G.; Galbraith, J. A.; Betzig, E., Live-cell photoactivated localization microscopy of nanoscale adhesion dynamics. *Nature methods* **2008,** *5* (5), 417-23.

43. Betzig, E.; Patterson, G. H.; Sougrat, R.; Lindwasser, O. W.; Olenych, S.; Bonifacino, J. S.; Davidson, M. W.; Lippincott-Schwartz, J.; Hess, H. F., Imaging intracellular fluorescent proteins at nanometer resolution. *Science* **2006,** *313* (5793), 1642-5.

44. Marriott, G.; Mao, S.; Sakata, T.; Ran, J.; Jackson, D. K.; Petchprayoon, C.; Gomez, T. J.; Warp, E.; Tulyathan, O.; Aaron, H. L.; Isacoff, E. Y.; Yan, Y., Optical lock-in detection imaging microscopy for contrast-enhanced imaging in living cells. *Proc Natl Acad Sci U S A* **2008,** *105* (46), 17789-17794.

45. Mahoney, D. P.; Owens, E. A.; Fan, C.; Hsiang, J.-C.; Henary, M. M.; Dickson, R. M., Tailoring Cyanine Dark States for Improved Optically Modulated Fluorescence Recovery. *The Journal of Physical Chemistry B* **2015,** *119* (13), 4637-4643.

46. Wang, L. V., *Photoacoustic Imaging and Spectroscopy*. CRC Press: 2009.

47. Wang, L. V.; Wu, H.-I., Diffuse Optical Tomography. In *Biomedical Optics*, John Wiley & Sons, Inc.: 2009; pp 249-281.

48. Zhang, H. F.; Maslov, K.; Stoica, G.; Wang, L. V., Functional photoacoustic microscopy for high-resolution and noninvasive in vivo imaging. *Nat Biotech* **2006,** *24* (7), 848-851.

49. Xu, M.; Wang, L. V., Photoacoustic imaging in biomedicine. *Review of Scientific Instruments* **2006,** *77* (4), -.

50. Wang, L., *Photoacoustic imaging and spectroscopy*. CRC Press: 2009; Vol. 144.

51. Wang, L. V., and Wu, H., *Biomedical Optics Principles and Imaging*. Wiley and Sons, Inc: New Jersey, 2007.

52. Larkin, J. M.; Donaldson, W. R.; Knox, R. S.; Foster, T. H., Reverse intersystem crossing in rose bengal. II. Fluence dependence of fluorescence following 532 nm laser excitation. *Photochem Photobiol* **2002,** *75* (3), 221-8.

53. Gratz, H.; Penzkofer, A., Saturable absorption dynamics in the triplet system and triplet excitation induced singlet fluorescence of some organic molecules. *Chemical Physics* **2001,** *263* (2), 471-490.

54. Reindl, S.; Penzkofer, A., Higher excited-state triplet-singlet intersystem crossing of some organic dyes. *Chemical Physics* **1996,** *211* (1), 431-439.

55. Ringemann, C.; Schonle, A.; Giske, A.; von Middendorff, C.; Hell, S. W.; Eggeling, C., Enhancing fluorescence brightness: effect of reverse intersystem crossing studied by fluorescence fluctuation spectroscopy. *Chemphyschem* **2008,** *9* (4), 612-24.

56. Sandén, T.; Persson, G.; Thyberg, P.; Blom, H.; Widengren, J., Monitoring Kinetics of Highly Environment Sensitive States of Fluorescent Molecules by Modulated Excitation and Time-Averaged Fluorescence Intensity Recording. *Analytical Chemistry* **2007,** *79* (9), 3330-3341.

57. Kaido, M.; Matsumoto, Y.; Shigeno, Y.; Ishida, R.; Dogru, M.; Tsubota, K., Corneal Fluorescein Staining Correlates with Visual Function in Dry Eye Patients. *Investigative Ophthalmology & Visual Science* **2011,** *52* (13), 9516-9522.

58. McCraw, J. B.; Myers, B.; Shanklin, K. D., The value of fluorescein in predicting the viability of arterialized flaps. *Plastic and reconstructive surgery* **1977,** *60* (5), 710-9.

59. Urbanavičius, L.; Pattyn, P.; de Putte, D. V.; Venskutonis, D., How to assess intestinal viability during surgery: A review of techniques. *World journal of gastrointestinal surgery* **2011,** *3* (5), 59-69.

60. Sarkar, S.; Fan, C.; Hsiang, J.-C.; Dickson, R. M., Modulated Fluorophore Signal Recovery Buried within Tissue Mimicking Phantoms. *J. Phys. Chem. A* **2013,** *117* (39), 9501-9509.

61. Richards, C. I.; Hsiang, J.-C.; Senapati, D.; Patel, S.; Yu, J.; Vosch, T.; Dickson, R. M., Optically Modulated Fluorophores for Selective Fluorescence Signal Recovery. *Journal of the American Chemical Society* **2009,** *131* (13), 4619-4621.

62. Richards, C. I.; Hsiang, J.-C.; Khalil, A. M.; Hull, N. P.; Dickson, R. M., FRET-Enabled Optical Modulation for High Sensitivity Fluorescence Imaging. *Journal of the American Chemical Society* **2010,** *132* (18), 6318-6323.

63. Zheng, W.; Tu, D.; Huang, P.; Zhou, S.; Chen, Z.; Chen, X., Time-resolved luminescent biosensing based on inorganic lanthanide-doped nanoprobes. *Chemical Communications* **2015,** *51* (20), 4129-4143.

64. Zheng, W.; Huang, P.; Tu, D.; Ma, E.; Zhu, H.; Chen, X., Lanthanide-doped upconversion nano-bioprobes: electronic structures, optical properties, and biodetection. *Chemical Society Reviews* **2015,** *44* (6), 1379-1415.

65. Sun, J. W.; Baek, J. Y.; Kim, K.-H.; Moon, C.-K.; Lee, J.-H.; Kwon, S.-K.; Kim, Y.-H.; Kim, J.-J., Thermally Activated Delayed Fluorescence from Azasiline Based

Intramolecular Charge-Transfer Emitter (DTPDDA) and a Highly Efficient Blue Light Emitting Diode. *Chemistry of Materials* **2015,** *27* (19), 6675-6681.

66. Zhang, Q.; Li, B.; Huang, S.; Nomura, H.; Tanaka, H.; Adachi, C., Efficient blue organic light-emitting diodes employing thermally activated delayed fluorescence. *Nat Photon* **2014,** *8* (4), 326-332.

67. Zhang, Q.; Li, J.; Shizu, K.; Huang, S.; Hirata, S.; Miyazaki, H.; Adachi, C., Design of Efficient Thermally Activated Delayed Fluorescence Materials for Pure Blue Organic Light Emitting Diodes. *Journal of the American Chemical Society* **2012,** *134* (36), 14706-14709.

68. Dias, F. B.; Bourdakos, K. N.; Jankus, V.; Moss, K. C.; Kamtekar, K. T.; Bhalla, V.; Santos, J.; Bryce, M. R.; Monkman, A. P., Triplet Harvesting with 100% Efficiency by Way of Thermally Activated Delayed Fluorescence in Charge Transfer OLED Emitters. *Advanced Materials* **2013,** *25* (27), 3707-3714.

69. Lee, S. Y.; Yasuda, T.; Komiyama, H.; Lee, J.; Adachi, C., Thermally Activated Delayed Fluorescence Polymers for Efficient Solution-Processed Organic Light-Emitting Diodes. *Advanced Materials* **2016,** *28* (21), 4019-4024.

70. Krause, S.; Carro-Temboury, M. R.; Cerretani, C.; Vosch, T., Probing heterogeneity of NIR induced secondary fluorescence from DNA-stabilized silver nanoclusters at the single molecule level. *Physical Chemistry Chemical Physics* **2018,** *20* (24), 16316-16319.

71. Fleischer, B. C.; Petty, J. T.; Hsiang, J.-C.; Dickson, R. M., Optically Activated Delayed Fluorescence. *The Journal of Physical Chemistry Letters* **2017,** *8* (15), 3536-3543.

72. Awad, M.; McCarthy, P.; Blanchard, G., Photoisomerization of Cyanines. A comparative study of oxygen-and sulfur-containing species. *The Journal of Physical Chemistry* **1994,** *98* (5), 1454-1458.

73. Bahnick, D. A., Use of Huckel Molecular Orbital Theory in Interpreting the Visible Spectra of Polymethine Dyes: An Undergraduate Physical Chemistry Experiment. *Journal of Chemical Education* **1994,** *71* (2), 171.

74. Baraldi, I.; Carnevali, A.; Caselli, M.; Momicchioli, F.; Ponterini, G.; Berthier, G., Theoretical and photophysical study of photoisomerism of cyanine dyes: bisphenylaminopentamethine cyanine (BPPC). *J. Mol. Struct.: THEOCHEM* **1995,** *330* (1–3), 403-410.

75. Bures, F., Fundamental aspects of property tuning in push-pull molecules. *RSC Advances* **2014,** *4* (102), 58826-58851.

76. Mandal, D.; Pal, S. K.; Sukul, D.; Bhattacharyya, K., Photophysical processes of merocyanine 540 in solutions and in organized media. *The Journal of Physical Chemistry A* **1999,** *103* (41), 8156-8159.

77. Chibisov, A. K.; Zakharova, G. V.; Gorner, H., Effects of substituents in the polymethine chain on the photoprocesses in indodicarbocyanine dyes. *J. Chem. Soc., Faraday Trans.* **1996,** *92* (24), 4917-4925.

78. Su-Fan Wang, T. Z., Yu-Cheng Huang, Shi-Yong Ye, DFT Investigation on the Trans-cis Photoisomerization of Pentamethine Cyanine Dye Model Molecule. *Chinese J. Struct. Chem.* **2011,** *30* (3), 401-411.

79. Momicchioli, F.; Baraldi, I.; Berthier, G., Theoretical study of trans-cis photoisomerism in polymethine cyanines. *Chem. Phys.* **1988,** *123* (1), 103-112.

80. Huang, Z.; Ji, D.; Wang, S.; Xia, A.; Koberling, F.; Patting, M.; Erdmann, R., Spectral Identification of Specific Photophysics of Cy5 by Means of Ensemble and Single Molecule Measurements. *J. Phys. Chem. A* **2006,** *110* (1), 45-50.

81. Jia, K.; Wan, Y.; Xia, A.; Li, S.; Gong, F.; Yang, G., Characterization of photoinduced isomerization and intersystem crossing of the cyanine dye Cy3. *The Journal of Physical Chemistry A* **2007,** *111* (9), 1593-1597.

82. Meyer, Y. H.; Pittman, M.; Plaza, P., Transient absorption of symmetrical carbocyanines. *Journal of Photochemistry and Photobiology A: Chemistry* **1998,** *114* (1), 1-21.

83. Redmond, R. W.; Kochevar, I. E.; Krieg, M.; Smith, G.; McGimpsey, W. G., Excited State Relaxation in Cyanine Dyes: A Remarkably Efficient Reverse Intersystem Crossing from Upper Triplet Levels. *The Journal of Physical Chemistry A* **1997,** *101* (15), 2773-2777.

84. Widengren, J.; Seidel, C. A., Manipulation and characterization of photo-induced transient states of Merocyanine 540 by fluorescence correlation spectroscopy. *Physical Chemistry Chemical Physics* **2000,** *2* (15), 3435-3441.

85. Aramendia, P. F.; Krieg, M.; Nitsch, C.; Bittersmann, E.; Braslavsky, S. E., THE PHOTOPHYSICS OF MEROCYANINE 540. A COMPARATIVE STUDY IN ETHANOL AND IN LIPOSOMES. *Photochemistry and Photobiology* **1988,** *48* (2), 187-194.

86. Alarcon, E.; Aspee, A.; Gonzalez-Bejar, M.; Edwards, A. M.; Lissi, E.; Scaiano, J. C., Photobehavior of merocyanine 540 bound to human serum albumin. *Photochem. Photobiol. Sci.* **2010,** *9* (6), 861-869.

87. Mahoney, D. P.; Demissie, A. A.; Dickson, R. M., Optically Activated Delayed Fluorescence through Control of Cyanine Dye Photophysics. *The Journal of Physical Chemistry A* **2019,** *123* (16), 3599-3606.

88. Widengren, J.; Seidel, C. A. M., Manipulation and characterization of photo-induced transient states of Merocyanine 540 by fluorescence correlation spectroscopy. *Physical Chemistry Chemical Physics* **2000,** *2* (15), 3435-3441.

89. Lambert, C. R.; Kochevar, I. E.; Redmond, R. W., Differential Reactivity of Upper Triplet States Produces Wavelength-Dependent Two-Photon Photosensitization Using Rose Bengal. *The Journal of Physical Chemistry B* **1999,** *103* (18), 3737-3741.

90. Benniston, A. C.; Harriman, A., Photoisomerization of a sterically constrained merocyanine dye. *J Chem Soc Faraday T* **1998,** *94* (13), 1841-1847.

91. Redmond, R.; Kochevar, I.; Krieg, M.; Smith, G.; McGimpsey, W., Excited state relaxation in cyanine dyes: A remarkably efficient reverse intersystem crossing from upper triplet levels. *J Phys Chem A* **1997,** *101* (15), 2773-2777.

92. Benniston, A. C.; Harriman, A.; Gulliya, K. S., Photophysical properties of merocyanine 540 derivatives. *Journal of the Chemical Society, Faraday Transactions* **1994,** *90* (7), 953-9.

93. Chmyrov, V.; Spielmann, T.; Hevekerl, H.; Widengren, J., Trans–CisIsomerization of Lipophilic Dyes Probing Membrane Microviscosity in Biological Membranes and in Live Cells. *Analytical Chemistry* **2015,** *87* (11), 5690-5697.

94. Wu, L.; Dai, Y.; Jiang, X.; Petchprayoon, C.; Lee, J. E.; Jiang, T.; Yan, Y.; Marriott, G., High-Contrast Fluorescence Imaging in Fixed and Living Cells Using Optimized Optical Switches. *PLoS ONE* **2013,** *8* (6), e64738-8.

95. Elgass, K.; Caesar, K.; Wanke, D.; Harter, K.; Meixner, A.; Schleifenbaum, F., Application of FLIM-FIDSAM for the in vivo analysis of hormone competence of different cell types. *Analytical and Bioanalytical Chemistry* **2010,** *398* (5), 1919-1925.

96. Sun, Y.; Phipps, J.; Elson, D. S.; Stoy, H.; Tinling, S.; Meier, J.; Poirier, B.; Chuang, F. S.; Farwell, D. G.; Marcu, L., Fluorescence lifetime imaging microscopy: in vivo application to diagnosis of oral carcinoma. *Opt. Lett.* **2009,** *34* (13), 2081-2083.

97. Kim, C.; Erpelding, T. N.; Jankovic, L.; Pashley, M. D.; Wang, L. V., Deeply penetrating in vivo photoacoustic imaging using a clinical ultrasound array system. *Biomed. Opt. Express* **2010,** *1* (1), 278-284.

98. Luke, G.; Yeager, D.; Emelianov, S., Biomedical Applications of Photoacoustic Imaging with Exogenous Contrast Agents. *Ann Biomed Eng* **2012,** *40* (2), 422-437.

99. Maslov, K.; Zhang, H. F.; Hu, S.; Wang, L. V., Optical-resolution photoacoustic microscopy for in vivo imaging of single capillaries. *Opt. Lett.* **2008,** *33* (9), 929-931.

100. Wang, L. V.; Hu, S., Photoacoustic Tomography: In Vivo Imaging from Organelles to Organs. *Science* **2012,** *335* (6075), 1458-1462.

101. Wang, L. V., Prospects of photoacoustic tomography. *Medical Physics* **2008,** *35* (12), 5758-5767.

102. Song, K. H.; Stein, E. W.; Margenthaler, J. A.; Wang, L. V., Noninvasive photoacoustic identification of sentinel lymph nodes containing methylene blue in vivo in a rat model. *Journal of Biomedical Optics* **2008,** *13* (5), 054033-054033.

103. Erpelding, T. N.; Kim, C.; Pramanik, M.; Jankovic, L.; Maslov, K.; Guo, Z.; Margenthaler, J. A.; Pashley, M. D.; Wang, L. V., Sentinel lymph nodes in the rat: noninvasive photoacoustic and US imaging with a clinical US system. *Radiology* **2010,** *256* (1), 102-10.

104. Kim, C.; Song, K. H.; Gao, F.; Wang, L. V., Sentinel lymph nodes and lymphatic vessels: noninvasive dual-modality in vivo mapping by using indocyanine green in rats--volumetric spectroscopic photoacoustic imaging and planar fluorescence imaging. *Radiology* **2010,** *255* (2), 442-50.

105. de la Zerda, A.; Bodapati, S.; Teed, R.; May, S. Y.; Tabakman, S. M.; Liu, Z.; Khuri-Yakub, B. T.; Chen, X.; Dai, H.; Gambhir, S. S., Family of Enhanced Photoacoustic Imaging Agents for High-Sensitivity and Multiplexing Studies in Living Mice. *ACS Nano* **2012,** *6* (6), 4694-4701.

106. De La Zerda, A.; Zavaleta, C.; Keren, S.; Vaithilingam, S.; Bodapati, S.; Liu, Z.; Levi, J.; Smith, B. R.; Ma, T.-J.; Oralkan, O.; Cheng, Z.; Chen, X.; Dai, H.; Khuri-Yakub, B. T.; Gambhir, S. S., Carbon nanotubes as photoacoustic molecular imaging agents in living mice. *Nat Nano* **2008,** *3* (9), 557-562.

107. Homan, K. A.; Souza, M.; Truby, R.; Luke, G. P.; Green, C.; Vreeland, E.; Emelianov, S., Silver Nanoplate Contrast Agents for in Vivo Molecular Photoacoustic Imaging. *ACS Nano* **2011,** *6* (1), 641-650.

108. Kim, J.-W.; Galanzha, E. I.; Shashkov, E. V.; Moon, H.-M.; Zharov, V. P., Golden carbon nanotubes as multimodal photoacoustic and photothermal high-contrast molecular agents. *Nat Nano* **2009,** *4* (10), 688-694.

109. Mallidi, S.; Larson, T.; Tam, J.; Joshi, P. P.; Karpiouk, A.; Sokolov, K.; Emelianov, S., Multiwavelength Photoacoustic Imaging and Plasmon Resonance Coupling of Gold Nanoparticles for Selective Detection of Cancer. *Nano Letters* **2009,** *9* (8), 2825-2831.

110. Pai-Chi, L.; Wei, C. W.; Liao, C. K.; Chen, C. D.; Pao, K. C.; Wang, C. R. C.; Wu, Y. N.; Shieh, D. B., Photoacoustic Imaging of Multiple Targets Using Gold Nanorods. *Ultrasonics, Ferroelectrics and Frequency Control, IEEE Transactions on* **2007,** *54* (8), 1642-1647.

111. Zhang, Q.; Iwakuma, N.; Sharma, P.; Moudgil, B. M.; Grobmyer, S. R.; Jiang, H. In *In vivo Photoacoustic Imaging of Tumor Using Gold Nanoparticles as Contrast Agent*, Biomedical Optics and 3-D Imaging, Miami, Florida, 2010/04/11; Optical Society of America: Miami, Florida, 2010; p BTuD23.

112. Cheng, C.; Muller, K. H.; Koziol, K. K. K.; Skepper, J. N.; Midgley, P. A.; Welland, M. E.; Porter, A. E., Toxicity and imaging of multi-walled carbon nanotubes in human macrophage cells. *Biomaterials* **2009,** *30* (25), 4152-4160.

113. Cui, D. X.; Tian, F. R.; Ozkan, C. S.; Wang, M.; Gao, H. J., Effect of single wall carbon nanotubes on human HEK293 cells. *Toxicology Letters* **2005,** *155* (1), 73-85.

114. Liu, Z.; Davis, C.; Cai, W.; He, L.; Chen, X.; Dai, H., Circulation and long-term fate of functionalized, biocompatible single-walled carbon nanotubes in mice probed by Raman spectroscopy. *Proceedings of the National Academy of Sciences* **2008,** *105* (5), 1410-1415.

115. Yao, D.-K.; Zhang, C.; Maslov, K.; Wang, L. V., Photoacoustic measurement of the Grüneisen parameter of tissue. *Journal of biomedical optics* **2014,** *19* (1), 17007-17007.

116. Petrova, E.; Liopo, A.; Oraevsky, A. A.; Ermilov, S. A., Temperature-dependent optoacoustic response and transient through zero Grüneisen parameter in optically contrasted media. *Photoacoustics* **2017,** *7*, 36-46.

117. Shah, J.; Park, S.; Aglyamov, S.; Larson, T.; Ma, L.; Sokolov, K.; Johnston, K.; Milner, T.; Emelianov, S. Y., Photoacoustic imaging and temperature measurement for photothermal cancer therapy. *J Biomed Opt* **2008,** *13* (3), 034024.

118. Buettner, A. V., Flash Photolysis in Thin Films of Gelatin and Other Polymers1. *The Journal of Physical Chemistry* **1964,** *68* (11), 3253-3259.

119. Jeon, S. M.; Choi, S.; Lee, K.; Jung, H.-S.; Yu, J., Significantly improved stability of silver nanodots via nanoparticles encapsulation. *Journal of Photochemistry and Photobiology A: Chemistry* **2018,** *355*, 479-486.

120. Yang, S.-A.; Choi, S.; Jeon, S. M.; Yu, J., Silica nanoparticle stability in biological media revisited. *Scientific reports* **2017**, 1-9.